LARGE-SCALE ENGINEERED METALLIC NANSTRUCTURES FOR HIGH-THROUGHPUT SURFACE PLASMON RESONANCE BIOSENSING AND SURFACE-ENHANCED RAMAN SPECTROSCOPY

A DISSERTATION
SUBMITTED TO THE FACULTY OF THE GRADUATE SCHOOL
OF THE UNIVERSITY OF MINNESOTA
BY

SI HOON LEE

IN PARTIAL FULFILLMENT OF THE REQUIREMENTS
FOR THE DEGREE OF
DOCTOR OF PHILOSOPHY

PROF. SANG-HYUN OH, PH.D

JULY, 2012

Acknowledgements

I would like to thank my advisor, Professor Sang-Hyun Oh, for his guidance and encouragement in this research during my Ph.D. study. I am also grateful for having the opportunity to work with our collaborators, Professors Christy Haynes, David Norris, and Russel Holmes. I would also like to thank the members of my dissertation committee, Professors Jian-Ping Wang, and Ronald Siegel.

The results presented in this dissertation could not have happened without the help and support of my labmates. First, I would also like to thank former members of the Oh group, Antoine Lesuffleur, Nathan Lindquist, and Hyungsoon Im who were pioneers of the "NanoBio" lab. They built up the upright microscope which grew into the current luxurious setups as well as precious process recipes. I specially thank Hyungsoon who shared many sleepless nights in the nanofabrication Center (NFC). I really enjoyed a lot of his process recipes. Nor can any of my work be accomplished without the help of current members. Many of my FDTD results are done by Tim Johnson. Most of membrane protein chemistry recipes were prepared by Nate Wittenberg. I also would like to thank Luke Jordan, Shailabh Kumar, and Avijit Barik who are enrolled in same BME program. They helped with lipid preparation and SPR biosensing. I also would like to thank Sudhir Cherukulappurath for his help on SERS measurements of the DEP project, Jincy Jose for her helpful discussion on plasmonics, and Xiaoshu Chen for her help of NFC processes, particularly, metal deposition. Lastly, I would like to encourage Daehan Yoo who joined Oh group last year to also achieve great things and keep the Korean

pipeline of excellence open and well. Although I am leaving this world-class lab, I believe, all who are working in the Oh's lab will present sensational results soon.

I would like to also thank co-authors of my papers, Kyle Bantz and Wade Luhman. My research presented in this dissertation could not be achieved without the help and support of their collaborations. My gratitude also extends to the helpful staffs at Nanofabrication Center and Characterization Facility at the University of Minnesota for their support.

I thank many good friends I met here, the people of Paul's Mission in Korean Presbyterian Church of Minnesota (KPCM), the alumni and their family of Pusan National University, friends in ECE, BME, and the Chemistry department. I will remember them and their help and kindness forever.

I would like to thank Samsung for supporting my graduate study at the University of Minnesota, particularly, my team-leader Sayoon Kang, group-leader Kyoungsei Choi for their full support and sincere encouraging to participate in this fellowship program.

Outside of school, I am deeply grateful to my parents, parents-in-law, and brothers for their endless love, and hope they know that without their love, I would never have succeeded at this endeavor. Finally, I would like to give my special thanks to my wife Seon-Hee and lovely kids, Gayeon, Seoyoon, and Jaehyung who are the most special things in my life.

Dedication

I dedicate this dissertation and all the work presented here to my wife Seon-Hee for her love and commitment to me and our kids. Yet, most importantly to God I love.

ABSTRACT

Precise measurements of binding kinetics and affinity of receptor-ligand interactions play an important role in pharmaceutical development as well as basic biology. Since a new drug discovery requires tremendous amount of time and cost, the demand for a high-throughput screening as well as precise kinetics measurement has increased dramatically. Although the commercially available BIAcore^{TM} system has been the gold standard for label-free and real-time biosensing, it is not capable of high-throughput kinetic measurements that are required for large-scale proteomics studies. To address the critical challenges, high-throughput SPR imaging instruments based on plasmonic nanohole arrays is demonstrated in this dissertation. The key advantage of nanohole-based SPR setup is that plasmons can be excited at normal incidence, which enables simple optical alignment and high-resolution imaging. Using template stripping technology, massively parallel and highly homogenous nanohole arrays, which is the prerequisite to perform high-throughput SPR imaging, are obtained over a large area (~cm^2). Linewidths of *extraordinary transmission* (EOT) peaks are optimized by reducing the damping losses of *surface plasmon polaritons* (SPPs), leading to the improved detection limits of the sensor. By combining the highly parallel microfluidics with periodic nanohole arrays, our SPR imaging spectrometer system enables high-throughput, label-free, real-time SPR biosensing, and its full-spectral imaging capability increases the dynamic range of detection. Additionally, molecular identification via *surface-enhanced Raman spectroscopy* (SERS) is also presented in the second portion of the dissertation. Two approaches include planar-type nanohole structures aimed for highly reproducible SERS substrates with low-cost and dynamic nanogaps pearlchains via *dielectrophoresis* (DEP) for the rapid and ultrasensitive molecular detection and identification.

Contents

List of Tables

List of Figures

List of Publications

1. **S. H. Lee**, N. C. Lindquist, N. J. Wittenberg, L. R. Jordan, and S.-H. Oh, *Lab on a Chip* (2012) Accepted.
2. **S. H. Lee**, T. W. Johnson, N. C. Lindquist, H. Im, D. J. Norris and S.-H. Oh, *Advanced Functional Materials* (2012), Accepted
3. H. Im, **S. H. Lee**, N. J. Wittenberg, T. W. Johnson, N. C. Lindquist, P. Nagpal, D. J. Norris, S. H. Oh, *ACS Nano* **5** (8), 6244-6253, (2011)
4. K. C. Bantz, A. F. Meyer, N. J. Wittenberg, H. Im, O. Kurtulus, **S. H. Lee**, N. C. Lindquist, S. -H. Oh, *Physical Chemistry Chemical Physics,* 13, 11551-11567 (2011).
5. W. A. Luhman, **S. H. Lee**, T. J. Johnson, R. J. Holmes, S. -H. Oh, *Applied Physics Letters* ,99 , 103306 (2011)
6. **S. H. Lee**, K.C. Bantz, N.C. Lindquist, S.-H. Oh, C.L. Haynes, *Langmuir* **25** (23), 13685-13693 (2009)
7. **S. H. Lee**, S. Cherukulappurath, C. L. Haynes, S. -H. Oh, in preparation

CHAPTER 1

INTRODUCTION

Recent scientific and technological advancements have been truly astonishing. Nanotechnology has enabled us to approach to an atomic and molecular scale study. Human genome project successfully traced the secret of life. The spatial constraints have been obviated due to the advancement of aerospace technology. These technological advancements have brought the remarkable improvement in the quality of life as well as the continuous increase in life expectancy. But they often have accompanied unexpected effects such as nano-toxicity, environmental pollutions, and the faster spread of epidemic. To deal with these problems, there also have been great efforts in the pharmaceutical industry to find better cures. After the seminal work by Langley[1] and Ahlqust[2], the process of new drug discovery has moved from the era of chemistry to the era of biochemistry, in which the concepts of "receptor" and "chemotherapeutic agent" were formulated. Afterwards, owing to the development of genomics and proteomics, it has become possible to better understand target-receptor bindings and signaling pathways within the cell.

Typically, the entire drug discovery process takes an average of 12-15 years to be completed, and at the beginning of the process, thousands of substances are developed,

examined, and screened to verify the potency, selectivity, and unique chemistry to bind to a disease-related receptor. Due to cost-cutting and time-saving initiatives, high-throughput screening (HTS) has evolved into a central enabling tool and methodology in the discovery of clinical compounds. However, despite the recent scientific and technological progresses in the pharmaceutical industry, technological advances have not increased new drug approval by the FDA [3,4]. In 2010, The FDA approved 18 new molecular entities (NME) and 3 biologics, totaling 21 drugs in 2010, decreased from 26 in 2009, and 24 in 2008. All of which prove that the current methods of drug discovery are not optimal and it is imperative to approach a current drug discovery from novel concepts with new technological functionality.

1.1 High-throughput screening (HTS) for drug discovery

High-throughput screening (HTS), evaluating ~ 10^4 compounds per day or per week, has been widely used in pharmaceutical industry and allowed large-scale "-omics" studies. Once the targets such as GPCR, enzymes, hormones are selected, the clinical compounds in the library are screened with high speed and filtered to hundreds of drug candidates. Various detection methods are present such as 2-D fluorescence intensity distribution analysis (FIDA), confocal fluorescence lifetime analysis (cFLA), and fluorescence intensity and lifetime distribution analysis (FILDA). It is applicable not only for a whole cell assay but also for an individual proteins and organelles within the cell.[5] However, while this technique is greatly advantageous in time scale, it has a couple of drawbacks which must be complemented. The fluorescence molecules used for the observation only

give on/off information. Therefore, they do not provide the association/dissociation rate constants (k_{on},,k_{off}), which results in the same affinity ($1/K_D$) from different combinations of association/dissociation rate constants . In addition, the target-based screening may be incorrect since the target binding on ligands usually triggers multiple signal pathways within the cell. Therefore, a method which is able to monitor the output of experimentally controlled target binding by a label-free, real-time, high-throughput manner will greatly improve the rate of successful drug discovery.

1.2 Optical biosensor for drug discovery

1.2.1 Surface plasmon resonance (SPR) biosensor

Seeing is believing. Among the various types of sensors, which include electric, magnetic, electrochemical, and mechanical types, optical biosensors have been most successful to date due to several advantages. They are non-destructive and are not sensitive to solution conditions such as pH or salt concentration. In addition, optical system can be easily miniaturized and multiplexed. Typically, such optical biosensor utilizes an "evanescent" optical field to detect the molecular interactions. When target molecules bind on the receptor, they perturb the evanescent field near the surface which, in turn, changes the optical signals. Due to this evanescent field, the binding event can be detected without labeling of fluorescent or radioactive molecules on the target which can potentially alter or interfere with specific molecular binding sites. Among these optical biosensors, surface plasmon resonance (SPR) techniques have been successfully

demonstrated in this field with a couple of commercial instruments which can characterize binding interactions between small molecules, proteins, nucleic acids, and even viruses.[6-10] Surface plasmons (SPs) are electromagnetic waves propagating at the interface between a metallic film and a dielectric medium in a form of exponentially decaying evanescent field.[11,12] The strongly confined electric field makes SPs sensitive to the local refractive index changes near the surface. By monitoring the shifts of a resonance output such as a resonance angle or a wavelength, it is possible to track the events near the sensing surface in a real-time, label-free manner.[13,14]

Alternatively, SPs can also be excited by the grating coupling such as periodic nanohole arrays.[15] The key advantage of this setup is that plasmons can be excited at normal incidence, which makes optical alignment and high-resolution imaging much easier to perform. Contrarily, the previously mentioned commercial SPR biosensors need a prism to excite SPs which makes the instrument bulky, expensive, and low-throughput.

1.2.2 Raman spectroscopy

Although SPR biosensors detect the molecular binding events in a real-time, label-free manner, they do not provide any chemical, molecular structural information. Thus, this technique is useful when we know the binding partners but do not know the affinity and binding rate constants. Contrarily, Raman spectroscopy is another optical label-free detection technique which utilizes the molecules' unique vibration modes. When light collides with molecules, light mostly scatters elastically, in which the energy of scattered photons is unchanged. However, a very small portion of photons scatter in-elastically by

absorbing or losing some energy. This resulting specific "fingerprints" of molecules have made this technique as a promising tool for label-free identification method. With the development of *surface-enhanced Raman spectroscopy* (SERS) where Raman signal is enhanced 10^4~10^8 times,[16,17] the probing capability has been expanded to small molecules[18-22], DNA/apatmers[23-26], proteins, peptides.[27,28] However, due to the feeble scattering intensity, temporal resolution of SERS is considerably low compared with transmission or reflection based measurements. This prohibits the SERS technique from the wide use in real-time biosensing applications. Therefore the combination of SPR biosensing for detection and SERS for identification will greatly increase their measurement power.

1.2.3 Limit of current technology

Although the commercial SPR instruments have been widely adopted in pharmaceutical drug discovery, the binding events can only be monitored with limited throughput. To satisfy the general standard for large-scale genomics and proteomics studies, the throughput should be improved tens or hundreds folds more. To address this challenge, high density nanohole SPR biosensors have been demonstrated so far but limited to the proof-of-concept level due to the lack of massively parallel nanofabrication techniques. Therefore, it is critical to develop new SPR instruments equipped with high-quality, low-cost, and large-area nanohole arrays to cope with the scale of the pharmaceutical industry.

1.3 Scope of the dissertation

Research presented in this dissertation focuses chiefly on the development of high-throughput surface plasmon resonance (SPR) imaging instruments to satisfy the general standard for large-scale genomics and proteomics studies. To accomplish this goal, massively parallel and high-quality nanohole fabrication techniques are developed and presented in the first portion of the dissertation. Since SPPs are tightly bound to the metal interface, they are very sensitive to molecular bindings on the surface but also vulnerable to any random surface roughness. Thus, after developing high-throughput nanohole fabrication methods, research has been performed to minimize the spectral linewidth to obtain sharp and intense resonance peaks by reducing the materials as well as radiative damping loss. Unlike conventional intensity-based SPR imaging setup, full-spectral information has been acquired via previously developed high-quality and large-area nanohole arrays. This nanohole SPR spectral imaging setup provides not only high-throughput biosensing capability but also binding kinetics and affinities from each and every channel simultaneously. Besides high-throughput molecular detection by SPR biosensing, *surface-enhanced Raman spectroscopy* (SERS) is used to identify the molecules. Two approaches to fabricate SERS substrates such as nanoholes by *nanosphere lithography* (NSL) and nanogap pearlchains by *dielectrophoresis* (DEP) are presented in the second portion of the dissertation.

1.3.1 Outline of chapters

This dissertation is organized into following chapters and each chapter outlines original research performed during the course of graduate study.

Chapter 2 describes background theory about S*urface Plasmon Polaritions* (SPPs) and the *Extraordinary Optical Transmission* (EOT) phenomenon mediated by periodic nanohole arrays. In addition, methods to analyze molecular binding interactions to determine kinetic constants and binding affinities are presented.

Chapter 3 presents two novel methods to fabricate high-quality, low-cost, and large-area plasmonic nanohole arrays. These massively parallel and high-quality nanohole arrays fabrication methods enable high-throughput SPR imaging.

Chapter 4 presents a linewidth-optimized Fano-resonance, showing ultra-sharp resonance peaks. The roles of nanohole diameter and dielectric functions of metal to achieve ultra-sharp Fano-resonance peaks are presented. The bulk and surface sensitivity are compared with 3-D FDTD calculations.

Chapter 5 presents SPR spectral imaging for high-throughput affinity measurements. The uniformity of optical properties and refractive index sensitivity of the device are evaluated. 50-channel binding kinetics of cholera toxin b subunit (CTX-b) to gangliosidemonosialic (GM1) receptors is demonstrated to confirm the capability of this system.

Chapter 6 describes another label-free biosensing technique, *surface-enhanced Raman spectroscopy* (SERS), which can identify molecules from their characteristic molecular vibration modes. A highly reproducible and simple fabrication method using

nanosphere lithography (NSL) is presented first. Dynamic nanogap formation via dielectrophoresis (DEP) is also presented for a rapid and ultrasensitive SERS detection.

Chapter 7 presents additional work performed during the graduate study regarding self-assembled plasmonic electrodes for high-performance organic photovoltaic cells.

Chapter 8 summarizes the research works presented in the dissertation.

CHAPTER 2

BACKGROUND THEORY

IN this chapter, fundamental background theories for understanding the electrodynamics of metals and *Surface Plasmon Polaritons* (SPPs) will be presented. It also introduces the *Extraordinary Optical Transmission* (EOT) phenomenon which is mediated by periodic nanohole arrays. Finally, methods to analyze molecular binding interactions to determine kinetic constants, i.e. binding rates and binding affinity, are described.

2.1 Electromagnetics of Metals

2.1.1. Maxwell's equations

When light interacts with a material system, the response of the atoms or molecules in the material can be represented by using Maxwell's equations.

$$\nabla \cdot \boldsymbol{D} = 0 \qquad (2.1)$$

$$\nabla \cdot \boldsymbol{B} = 0 \tag{2.2}$$

$$\nabla \times \boldsymbol{E} = -\frac{\partial}{\partial \boldsymbol{t}} \boldsymbol{B} \tag{2.3}$$

$$\nabla \times \boldsymbol{H} = \frac{\partial}{\partial \boldsymbol{t}} \boldsymbol{D} \tag{2.4}$$

,where **D** and **B** are the electric and magnetic flux density, respectively. **E** and **H** are the electric and magnetic field intensity, respectively. The electric and magnetic flux density can be often expressed with the electric field and the magnetic field, respectively.

$$\begin{aligned} \boldsymbol{D} &= \varepsilon \boldsymbol{E} = \varepsilon_r \varepsilon_0 \boldsymbol{E} \\ \boldsymbol{B} &= \mu \boldsymbol{H} = \mu_r \mu_0 \boldsymbol{H} \end{aligned} \tag{2.5}$$

,where ε_0 is the electric permittivity of free space (8.854×10^{-12} F/m) and μ_0 is the magnetic permeability of free space ($4\pi \times 10^{-7}$ H/m). ε_r and μ_r are the relative electrical permittivity and magnetic permeability of the material. For a non-magnetic material, where μ_r =1, the magnetic flux density becomes $\boldsymbol{B} = \mu_0 \boldsymbol{H}$.

In an applied electric field (**E**), the total electric flux density (**D**) is composed of the flux from both the external E-field and material polarization (**P**). When **P** is linearly proportional to **E**, **D** becomes:

$$\boldsymbol{D} = \varepsilon_0 \boldsymbol{E} + \boldsymbol{P} = \varepsilon_0 \varepsilon_r \boldsymbol{E} \tag{2.6}$$

To help understand the dispersive behavior of metals, we need to consider the *wave equation* of electromagnetic fields, starting from Maxwell's equation:

$$\nabla \times \nabla \times \mathbf{E} = -\mu_0 \frac{\partial^2 \mathbf{D}}{\partial t^2} \tag{2.7}$$

Assuming an $\exp(-\boldsymbol{i}\omega\boldsymbol{t})$ time-harmonic behavior, a solution to this equation can be found when the electric field is expressed as:

$$\mathbf{E}(r) = E_0 e^{i(K \cdot r - \omega t)} \tag{2.8}$$

,where **K** is the wavevector of the plane wave and ω is the frequency of the wave. The divergence and curl of electric field can be re expressed as:

$$\begin{aligned} \nabla \cdot \mathbf{E} &= \boldsymbol{i}\boldsymbol{K} \cdot \mathbf{E} \\ \nabla \times \mathbf{E} &= \boldsymbol{i}\boldsymbol{K} \times \mathbf{E} \end{aligned} \tag{2.9}$$

By using curl of the curl relation we get:

$$\begin{aligned} \nabla(\nabla \cdot \boldsymbol{E}) - \nabla^2 \boldsymbol{E} &= -\boldsymbol{K}(\boldsymbol{K} \cdot \boldsymbol{E}) + \boldsymbol{K}^2 \boldsymbol{E} \\ &= \mu_0 \varepsilon(\boldsymbol{K}, \omega)\omega^2 \boldsymbol{E} = \varepsilon(\boldsymbol{K}, \omega)\frac{\omega^2}{\boldsymbol{c}^2}\boldsymbol{E} \end{aligned} \tag{2.10}$$

Now, a general dispersion relations can be expressed as:

$$\mathbf{K}(\mathbf{K} \cdot \mathbf{E}) - K^2 \mathbf{E} = -\varepsilon(\mathbf{K}, \omega)\frac{\omega^2}{c^2}\mathbf{E} \tag{2.11}$$

,where c is the speed of wave given by $c = 1/\sqrt{\mu_0 \varepsilon_0}$.

For transverse waves where wave motion and propagation direction are perpendicular (i.e. $\mathbf{K} \cdot \mathbf{E} = 0$), the dispersion relationship can be expressed as:

$$K^2 = \varepsilon(\mathbf{K}, \omega)\frac{\omega^2}{c^2} \tag{2.12}$$

For $\varepsilon(\mathbf{K},\omega) > 0$, the wavevector **K** has always a real value, allowing the light propagation in the metal. In this case, the metal will act as a dielectric material. For $\varepsilon(\mathbf{K},\omega) < 0$ when frequency of light (ω) is less than plasmon frequency (ω_p), the wavevector **K** becomes a complex value. This implies transverse electromagnetic waves can have a surface plasmon polaritons (SPPs) propagating along the metal surface but decaying exponentially into and out of the metal and the dielectric interface.

For longitudinal waves where wave motion and propagation direction are same (i.e. $\mathbf{K}(\mathbf{K}\cdot\mathbf{E}) - K^2\mathbf{E} = 0$), the relation yields:

$$\varepsilon(\mathbf{K},\omega) = 0 \tag{2.13}$$

This means longitudinal collective oscillations can only occur at $\varepsilon(\omega) = 0$. All electrons in volume will be oscillating in phase at the volume plasmon frequency (ω_p).

2.1.2. Dielectric function of a metal

In most case, when light interacts with matter, it is an electron that is the prime consideration. Many solid state phenomena can be explained using the movement of electrons in a lattice. Another approach for the light-matter interaction, particularly in metal, is the plasma concept of free electrons since they have almost an unlimited number of free electrons.[29,30] In this model, the motion for an electron in an external electric field **E**(t) can be described as:

$$m\ddot{\mathbf{x}} + m\gamma\dot{\mathbf{x}} = -e\mathbf{E} \tag{2.14}$$

,where *m* and *e* are the effective optical mass and charge of each electron, respectively and γ is a characteristic collision frequency defined as an inverse of the average time between electron collisions (γ = 1/τ). For a time-varying electric field $\mathbf{E}(t) = \boldsymbol{E}_0 e^{-i\omega t}$ where both the electron motion *x(t)* and the electric field **E**(t) have $\exp(-i\omega t)$ dependency, the solution of equation (2.14) becomes:

$$\mathbf{x}(t) = \frac{e\mathbf{E}(t)}{m(\omega^2 + i\gamma\omega)} \tag{2.15}$$

Then, the macroscopic polarization which depends on the number of charge (*n*), charge (*e*), and motion of electrons **x**(t), can be described as:

$$\mathbf{P} = -n_e e\mathbf{x} = -\frac{n_e e^2}{m(\omega^2 + i\gamma\omega)}\mathbf{E}(t) \tag{2.16}$$

Using equation (2.16), we can express the electron flux density **D** with dielectric constant $\varepsilon(\omega)$:

$$\mathbf{D} = \varepsilon_r \varepsilon_0 \mathbf{E} = \varepsilon_0 \mathbf{E} + \mathbf{P} = \varepsilon_0 (1 - \frac{\omega_p^2}{\omega^2 + i\gamma\omega})\mathbf{E} \tag{2.17}$$

,where the plasma frequency (ω_p) describing the transition frequency from dielectric behavior to metallic behavior is defined as:

$$\omega_p^2 = \frac{n_e e^2}{\varepsilon_0 m} \tag{2.18}$$

,where $\boldsymbol{n_e}$ is the electron density, *m* and *e* is a mass and charge of electron, respectively. From the Equation (2.17), the dielectric function of the free electron gas is derived as:

$$\varepsilon_r(\omega) = 1 - \frac{\omega_p^2}{\omega^2 + i\gamma\omega} = \varepsilon_1(\omega) + i\varepsilon_2(\omega), \tag{2.19}$$

,where the real and imaginary components of the dielectric function are given by:

$$\varepsilon_1(\omega) = 1 - \frac{\omega_p^2 \tau^2}{1 + \omega^2 \tau^2} \tag{2.20}$$

$$\varepsilon_2(\omega) = \frac{\omega_p^2 \tau}{\omega(1 + \omega^2 \tau^2)} \tag{2.21}$$

This dielectric function of metal, equation (2.19), is the so-called "*Drude"* model which only considers free electrons in the metal. In the visible and near-infrared range, where $\omega >> \gamma$, the imaginary part ($i\gamma\omega$) can be ignored since ω^2 dominates at high frequency. Thus, a simplified drude model describing a free electron gas $\varepsilon_r(\omega)$ is given by:

$$\varepsilon_r(\omega) = 1 - \frac{\omega_p^2}{\omega^2} \tag{2.22}$$

For $\omega > \omega_p$, this gives a positive dielectric function ($\varepsilon_r(\omega) > 0$) allowing propagation of light through the materials. For $\omega = \omega_p$, $\varepsilon_r(\omega) = 0$, meaning all electrons in the material are oscillating in phase at the plasma frequency (i.e. volume plasmon). For $\omega < \omega_p$, dielectric constant becomes negative, $\varepsilon_r(\omega) < 0$ and **K** becomes complex. Here, the real part of the dielectric function is responsible for the light propagation as a reflection form from metal surface and the imaginary part is responsible for the non-propagating evanescent field confined to metal and surrounding medium but decaying exponentially from the interface.

2.2 Surface Plasmon Polaritons (SPPs)

2.2.1 Theory

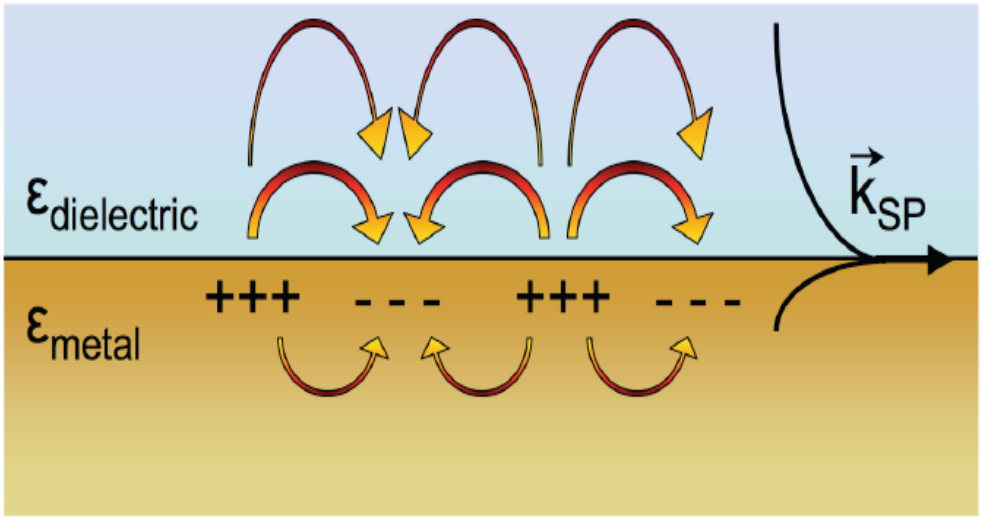

Figure 2.1 Surface plasmon polaritons (SPPs). Surface plasmon polaritons (SPPs) are collective oscillation of free electrons at the interface between a metal and a dielectric medium. They have a wavevector k_{spp} and the energy of the wave decays exponentially away from the surface. Generally, the field penetration depth δ_d into the dielectric is larger than the penetration depth δ_m into the metal.

Figure 2.1 shows a schematic of a surface plasmon polarition (SPP). A polariton is a coupled oscillation between an internal material motion (polarization) and EM wave. When incident light (EM waves) couples with the free electrons oscillating at the surface, it is called a surface plasmon polartions (SPP). With the continuous supply of incoming EM waves, the SPPs propagate only along the interface between the metal and dielectric medium and decay exponentially in the direction perpendicular to the interfacial area.[31,32] To derive the wave equation for SPPs, first, take the curl of the curl of Maxwell's equation:

$$\nabla^2 \boldsymbol{E} - \frac{\varepsilon}{\boldsymbol{c}^2}\frac{\partial^2 \boldsymbol{E}}{\partial \boldsymbol{t}^2} = 0 \tag{2.23}$$

By arranging this equation with the wavevector form, the wave equation becomes:

$$\nabla^2 \boldsymbol{E} + \boldsymbol{k}_0^2 \varepsilon \boldsymbol{E} = 0 \tag{2.24}$$

If we assume that the wave only propagates along the x-direction (Fig. 2.1), the equation can be expressed as:

$$\boldsymbol{E}(\boldsymbol{x}, \boldsymbol{y}, \boldsymbol{z}) = \boldsymbol{E}(\boldsymbol{z})\boldsymbol{e}^{\boldsymbol{i}\beta \boldsymbol{x}} \tag{2.25}$$

Therefore, if we consider the homogeneity along the y-direction, the wave equation for SPPs can be rearranged to give:

$$\frac{\partial^2 \boldsymbol{E}(\boldsymbol{z})}{\partial \boldsymbol{z}^2} + (\boldsymbol{k}_0^2 \varepsilon - \beta^2)\boldsymbol{E} = 0 \tag{2.26}$$

The formula for magnetic field will be a similar form. Because surface plasmons (SPs) cannot be excited by transverse-electric (TE) wave (i.e. longitudinal waves), we will only consider transverse-magnetic (TM) waves here. In TM mode, only $\boldsymbol{E}_x, \boldsymbol{E}_y, \boldsymbol{H}_y$ will be considered based on the assumption that the wave only propagates along the *x*-direction between a dielectric medium ($z > 0$) and a metal ($z < 0$) as shown in Figure 2.1. Therefore, we can assume that the wave equation for SPPs can be expressed as:

$$\begin{aligned} \boldsymbol{E} &= (\boldsymbol{E}_x, 0, \boldsymbol{E}_z)\exp[\boldsymbol{i}(\boldsymbol{k}_x \boldsymbol{x} + \boldsymbol{k}_z \boldsymbol{z} - \omega \boldsymbol{t})] \\ \boldsymbol{H} &= (0, \boldsymbol{H}_y, 0)\exp[\boldsymbol{i}(\boldsymbol{k}_x \boldsymbol{x} + \boldsymbol{k}_z \boldsymbol{z} - \omega \boldsymbol{t})] \end{aligned} \tag{2.27}$$

Combining equation (2.27) with maxwell's equations, we get For $\boldsymbol{z} > 0$ (i.e. dielectric side)

$$
\begin{aligned}
\boldsymbol{H}_y(\boldsymbol{z}) &= \boldsymbol{A}_d \boldsymbol{e}^{i\beta x} \boldsymbol{e}^{-k_d z} \\
\boldsymbol{E}_x(\boldsymbol{z}) &= \frac{\boldsymbol{i}\boldsymbol{k}_d}{\omega \varepsilon_0 \varepsilon_d} \boldsymbol{H}_y(\boldsymbol{z}) \\
\boldsymbol{E}_z(\boldsymbol{z}) &= \frac{-\beta}{\omega \varepsilon_0 \varepsilon_d} \boldsymbol{H}_y(\boldsymbol{z})
\end{aligned}
\tag{2.28}
$$

where k and β are the z- and x-components of wavevector **K**, ε is the dielectric constant, and subscripts m and d denote metal and dielectric.

For $\boldsymbol{z} < 0$ (i.e. metal side)

$$
\begin{aligned}
\boldsymbol{H}_y(\boldsymbol{z}) &= \boldsymbol{A}_m \boldsymbol{e}^{i\beta x} \boldsymbol{e}^{-k_m z} \\
\boldsymbol{E}_x(\boldsymbol{z}) &= \frac{-\boldsymbol{i}\boldsymbol{k}_m}{\omega \varepsilon_0 \varepsilon_d} \boldsymbol{H}_y(\boldsymbol{z}) \\
\boldsymbol{E}_z(\boldsymbol{z}) &= \frac{-\beta}{\omega \varepsilon_0 \varepsilon_d} \boldsymbol{H}_y(\boldsymbol{z})
\end{aligned}
\tag{2.29}
$$

To satisfy the boundary conditions for the continuity of $\boldsymbol{H}_y$ and $\boldsymbol{E}_x$ at the interface, we get $\boldsymbol{A}_d = \boldsymbol{A}_m$ and $\boldsymbol{k}_m / \boldsymbol{k}_d = -\varepsilon_m / \varepsilon_d$.

Also, from the equation (2.26), wavevector of each medium is arranged as:

$$
\begin{aligned}
\boldsymbol{k}_d^2 &= \beta^2 - \boldsymbol{k}_0^2 \varepsilon_d \\
\boldsymbol{k}_m^2 &= \beta^2 - \boldsymbol{k}_0^2 \varepsilon_m
\end{aligned}
\tag{2.30}
$$

By using equation (2.30) and $\boldsymbol{A}_d = \boldsymbol{A}_m$ and $\boldsymbol{k}_m / \boldsymbol{k}_d = -\varepsilon_m / \varepsilon_d$, the dispersion relations $\beta (= \boldsymbol{k}_x)$ is derived as below:

$$
\beta = \boldsymbol{k}_x = \boldsymbol{k}_{spp} = \frac{\omega}{\boldsymbol{c}} \sqrt{\frac{\varepsilon_d \cdot \varepsilon_m}{\varepsilon_d + \varepsilon_m}}
\tag{2.31}
$$

With the assumptions for the two materials that $\varepsilon_m = \varepsilon'_m + i\varepsilon''_m$, $|\varepsilon'_m| > \varepsilon''_m$, $\varepsilon'_m < 0$, and $|\varepsilon'_m| > \varepsilon_d$ at optical frequency, the dispersion relations can be expressed as $k_{spp} = k'_{spp} + ik''_{spp}$, where

$$\mathrm{Re}[\beta] = \boldsymbol{k}'_{spp} = \frac{\omega}{\boldsymbol{c}} \sqrt{\frac{\varepsilon_d \varepsilon'_m}{\varepsilon_d + \varepsilon'_m}} \tag{2.32}$$

$$\mathrm{Im}[\beta] = \boldsymbol{k}''_{spp} = \frac{\omega}{\boldsymbol{c}} \left(\sqrt{\frac{\varepsilon_d \varepsilon'_m}{\varepsilon_d + \varepsilon'_m}} \right)^3 \frac{\varepsilon''_m}{2\varepsilon'^2_m} \tag{2.33}$$

Detailed derivations of equation (2.32) and (2.33) formula are shown in the Appendix A.

In this equation, the imaginary component of $\boldsymbol{k}''_{spp}$ describes the internal damping such as an ohmic loss of the SPP, limiting the lifetime of SPPs at the metal-dielectric interface. As we mentioned earlier in equation (2.27), the E and H fields can be expressed as a $\exp(-\boldsymbol{i}\omega\boldsymbol{t})$ time-harmonic behavior such as:

$$\boldsymbol{E} \propto \boldsymbol{e}^{\boldsymbol{i}(\beta \boldsymbol{x} - \omega \boldsymbol{t})} \tag{2.34}$$

After arranging the equation with real and imaginary components, it becomes:

$$\boldsymbol{E} \propto \boldsymbol{e}^{\boldsymbol{i}(\mathrm{Re}[\beta])\boldsymbol{x}} \cdot \boldsymbol{e}^{\boldsymbol{i}(\boldsymbol{i}\,\mathrm{Im}[\beta])\boldsymbol{x}} \cdot \boldsymbol{e}^{-\boldsymbol{i}\omega\boldsymbol{t}} \tag{2.35}$$

Here, the decaying term which is imaginary component is expressed as:

$$|\boldsymbol{E}|^2 \propto \boldsymbol{e}^{-2\,\mathrm{Im}[\beta]\boldsymbol{x}} \tag{2.36}$$

Therefore, the propagation length of SPPs along the interface can be expressed with the formula $\boldsymbol{L} = (2\,\mathrm{Im}[\beta])^{-1} = \left(2\boldsymbol{k}''_{spp}\right)^{-1}$. In addition, the field amplitude of the SPP at the

interface will also decrease exponentially from the interface between the metal and dielectric. Now, the characteristic decay length defined by $\delta = 1/k_z$ can be expressed as:

$$\delta_d = \frac{\omega}{c}\sqrt{\frac{\varepsilon'_m + \varepsilon_d}{-\varepsilon_d^2}} \tag{2.37}$$

$$\delta_m = \frac{\omega}{c}\sqrt{\frac{\varepsilon'_m + \varepsilon_d}{-\varepsilon_m^2}} \tag{2.38}$$

Here, δ_d and δ_m denote the electromagnetic field decay length into dielectric and metal, respectively. The detailed derivations of equation (2.37) and (2.38) formula are shown in the Appendix A.

2.2.2 Dispersion relations of SPPs

Figure 2.2 presents the dispersion relation of light with different media. When light passes through air or silica, which is a dielectric material, the dispersion relation is a simple straight line which means it does not interact with the electrons in the medium. It is just squeezed based on the refractive index of the material and propagates through the medium. However, when light passes through the metal, it shows quite interesting behaviors. In chapter 2.2.1, we proved the frequency dependency of the incoming light for SPPs. Here, we can clearly observe the results of SPPs behavior in the metal. For small ω/ω_p , a k_{spp} curves show linear behavior, describing SPPs behaving like " light". In this regime, SPPs will propagate through the metal film. For $\omega/\omega_p \to 1/\sqrt{2}$, the SPPs approach the surface plasmon resonance (SPR) condition. In this "plasmon" regime, the

SPPs are squeezed in a very confined volume, thus, providing large momentum increase. As we can see in the Figure 2.2a, the momentum of light (1) is always smaller than the momentum of SPPs (2) in the same material since the SPPs curve always lies to the right of the light line. This implies that SPPs cannot be excited by free-space light in the same material due to the mismatch of momentums ($k_{spp} > k_x = k \sin\theta$) at any incidence angle.

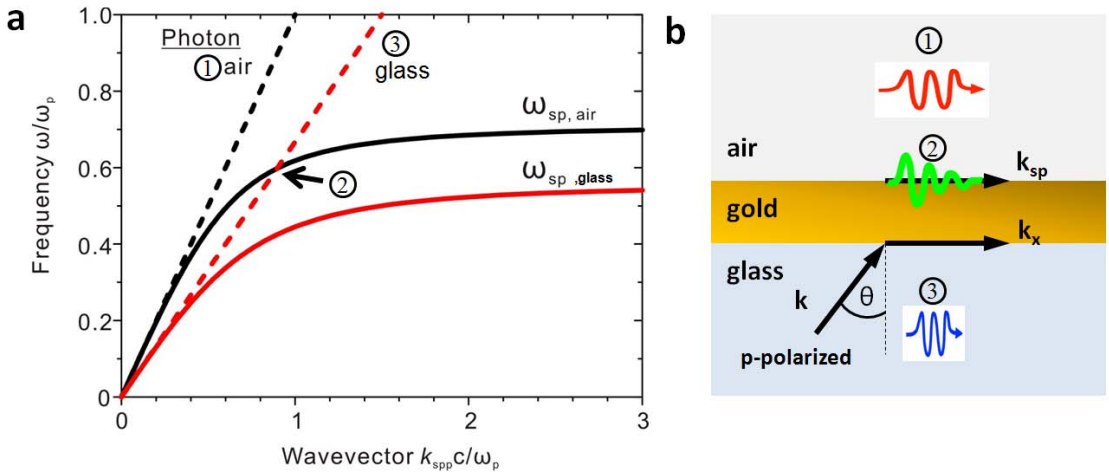

Figure 2.2 Dispersion relation of SPPs. The solid lines represents the dispersion curves of SPPs at the interfaces between Au and dielectric media (air and glass) and the dashed lines presents the dispersion curves of light in the dielectric media. kspp can be matched with kx at the gold and glass interface at the certain conditions. kspp will propagate along the air-gold interface but dampen out due to material and radiative damping of the plasmon.

However, the momentum of light in glass (3) can be matched with the momentum of SPPs in air at certain conditions. This implies the photon squeezed in glass can excite SPPs at the metal-air interface. Figure 2.2b shows the Kretchschmann configuration for

SPP excitation. In this setup, light is illuminated on the sensing spot in the gold film with an incident angle (θ) by using a prism. During the increase of the incident angle of light, the $\boldsymbol{k}_x$ at the metal-air interface is increased and matches $\boldsymbol{k}_{spp}$ at a certain angle. At this point, a sudden decrease of reflectivity is observed (Figure 2.3). This minimum in reflectivity means the incident light is coupled with the surface free electrons and converted to SPPs.[33]

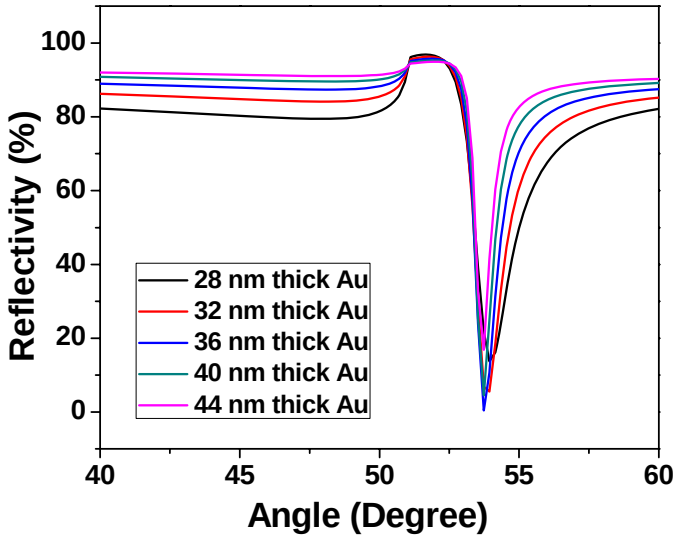

Figure 2.3 Reflectivity vs. the Au thickness in the Kretschmann configuration. When k_x matches with k_{spp}, incident light is coupled with the free surface electrons and converted to SPPs. This energy conversion will make a sharp dip in the reflectivity. The SPPs dip is related with many parameters such as refractive index, incident angle, and the thickness of Au.

2.3 Extraordinary optical transmission (EOT)

In the classical diffraction theory for light transmission through a single aperture, Bethe treated the metal as an infinitely thin, perfectly conducting film at the surface where light is impinging. For simplification, he assumed the hole, radius (a), is much smaller than the wavelength ($a << \lambda$) and is a magnetic dipole. Base on this approximation, he found that the transmission efficiency has the relationship:[34]

$$T = \frac{64}{27\pi^2}(kr)^4, \qquad (2.39)$$

,where $k = 2\pi/\lambda$ is the wavevector of incident light. This predicts that the transmission intensity drops with the *fourth* power of r/λ, indicating very weak transmission when the hole diameter is much smaller than the wavelength. As stated, one can imagine the transmission is dramatically reduced when a sub-wavelength size hole is punctured in the metal film. However, very a counterintuitive phenomenon which cannot be explained with just classical diffraction theory occurred when arrays of sub-wavelength holes are patterned in an optically thick metal film which has now been researched. This pioneering research on hole arrays in metal films has opened a new era of nanophotonics, contributing novel biosensors,[35] subwavlength optical circuitry,[36] high-density data storage,[37,38] and efficiency-enhanced photovoltaics.[39-41]

2.3.1 Origin of EOT from nanohole arrays

Although light transmission through hole arrays had been explored for decades, it was limited to theoretical study at micro-level (size, frequency) due to the technological limit

to produce a subwavelength dimension feature.[42-45] Therefore, due to the recent developments of nanofabrication technology, subwavelength size holes have attracted great attention in nano-photonics since it gives a response in the UV-visual regime which allows for many interesting applications. In 1998, Ebbesen and coworkers reported the observation of unusually high zero-order transmission after illuminating a Ag and Au film having subwavlength periodic nanohole arrays.[15] After normalizing the transmission intensity with the area occupied by holes, they concluded the intensity per hole at certain wavelengths is far more than the intensity from a single opening predicted by Bethe's diffraction theory. After this seminal discovery, a tremendous amount of work has been conducted to understand the mechanism of enhanced light transmission, and the influence of geometrical and optical properties for the EOT.[46-50] While there is a still debate about the exact mechanism of EOT, the majority agree on the role of SPPs at the metal-dielectric interfaces. Figure 2.4 shows a schematic of SPP generation, propagation, funneling through tiny holes, and radiation back to free space. Periodic nanohole arrays on the metallic surface increase the momentum of the incoming photons (equation 2.40), enabling the SPP excitation at the metal-dielectric interface.

$$k_{spp} = k_x + k_{gx} + k_{gy} = k_0 \sin\theta + n\frac{2\pi}{a_0} + m\frac{2\pi}{a_0} \qquad (2.40)$$

,where n and m are the resonance orders of the array and a_0 is the periodicity. These SPPs are confined in the normal direction of the interface but free to move along the interface. Even below the cutoff frequency at a small d and large λ, the SPPs can pass through the hole which acts as a waveguide, not being restricted by the diffraction theory (Figure 2.4). These transmitted SPPs can radiate back to free space by a reverse-grating coupling

mechanism. When they couple away from the metal-dielectric interface and leave as a far-field radiation, they can constructively or destructively interfere with the non-resonant transmitted light, resulting in the transmission maximum or minimum, respectively.

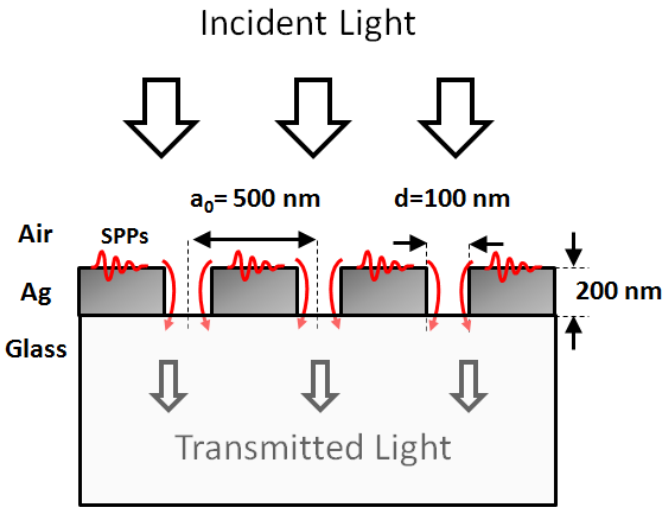

Figure 2.4 EOT of nanohole arrays. Schematic of SPPs generation, propagation, funneling through tiny holes, and radiation back to free space. Periodic nanohole arrays excite SPPs at the metal-dielectric interfaces.

2.3.2 Effects of geometries for optical properties

Previously, we discussed the role of SPPs for the extraordinary optical transmission (EOT) in periodic metallic nanohole arrays. In this part, various geometrical and optical properties affecting the EOT spectra will be discussed. The SPP excitation conditions and the transmission peak positions are determined by geometrical parameters (periodicity, hole size, and film thickness) as well as optical properties such as the dielectric functions

of the metal and surrounding media. Based on the SPP wavevector equation, the spectral positions of the transmission maxima can be approximated with the following equation:

$$\lambda_{\max} = a_0\left[(i^2 + j^2)\right]^{-1/2}\sqrt{\frac{\varepsilon_d \varepsilon_m}{\varepsilon_d + \varepsilon_m}}, \qquad (2.41)$$

,where a_0 is the periodicity of the array, the integers (i, j) represent the Bragg resonance orders, and ε_m and ε_d are the dielectric functions of the metal and dielectric, respectively. Table 2.1 shows the calculated transmission peak position based on the equation (2.41) using refractive index of water and dielectric functions of Ag. From these calculations, the (1,0) resonance peak occurs furthest to the red in the spectra, then, the higher order resonance peak come sequentially further in the blue direction. In addition, glass peaks of same resonance order are located at the longer wavelength position than that of the air or water peak.

Table 2.1 The position of EOT maxima having the different periodicity. The calculation is based on the equation (2.41) and includes λmax at the multiple resonance orders and two different interfaces.

Periodicity (nm)	**λ_{max}(nm)**					
	(2,1) water	**(2,1) glass**	**(1,1) water**	**(1,1) glass**	**(1,0) water**	**(1,0) glass**
400	388	414	455	503	578	649
500	410	445	526	588	699	787
600	442	487	607	682	825	930

However, the peak position ($\lambda_{\max}$) which is based on the k_{spp} equation shows big a discrepancy compared with the optical transmission spectra measured experimentally.

Figure 2.5 shows the transmission spectra of 200 nm thick Ag nanohole arrays with a 500 nm periodicity measured in an (a) air and (b) water environment. Although equation (2.41) expresses the maximum peak position, this theoretically calculated λ_{spp} is matched with λ_{min} in the real experiments.(Figure 2.5) This discrepancy of resonance position maxima, i.e. red shift from the minimum, can be explained by the existence of Fano-type interference between non-resonant transmission through the holes and the resonant portion due to SPPs. When the non-resonant term is larger than the resonant term in the transmission spectra, the maximum peak position is located more red, showing noticeable asymmetric Fano-type spectra.[48,51,52] In addition, transmission through periodic nanohole arrays is related with the reverse-grating coupling, and the loss of surface plasmon intensity (i.e. radiative, ohmic damping) also explains the position difference between the theoretical calculation and the experiment. When the surrounding medium is changed from air (n = 1.000) to water (n = 1.333), the SP resonance at the metal and surrounding medium interface is changed, thus, the (1,0) air peak shifts. However, the substrate resonance peak stays at the same position since the index of the substrate is not changed.

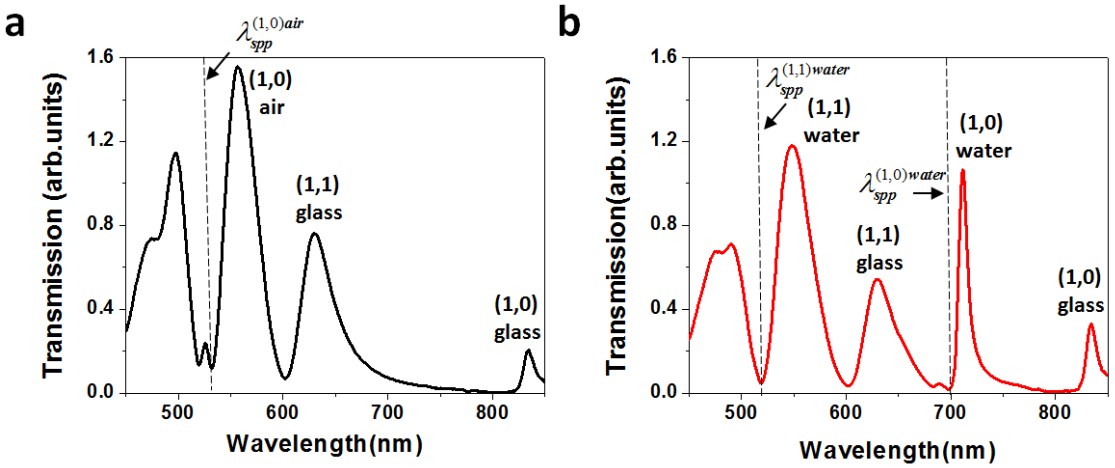

Figure 2.5 EOT spectra of nanohole arrays. Optical transmission spectra obtained from a 200 nm-thick Ag nanohole array having a 100 nm hole diameter and a 500 nm periodicity (a) in air, (b) in water. EOT spectra have multiple resonance peaks due to the two metal-dielectric interfaces and multiple resonance orders.

Besides the periodicity, the size (i.e. diameter) of the nanoholes is also critical parameter affecting EOT the spectra. Both the transmission intensity and the resonance peak position are affected by the size of holes. Many theoretical studies of hole arrays is using Babinet's principle, explaining that the transmittance (reflectance) of the particle array is identical to the reflectance (transmittance) of the complementary hole array, have be performed to explain the effect of hole size on the transmittance, linewidth, and position.[53,54] When the hole size becomes larger, larger polarizability is generated, which brings more red-shift to the λ_{max} and broader linewidth of the transmission spectrum. Inversely, as the hole size becomes smaller, the resonance peak becomes sharper and the λ_{max} position is blue-shifted. More detailed results on the diameter vs. linewidth will be presented in chapter 4.

2.4 Analysis of molecular binding kinetics

The response of the optical property change, i.e. effective refractive index increase, in a surrounding medium can be monitored from this EOT spectra shift. Therefore, SPR techniques are widely used in real-time, label-free biosensors applications. Unlike conventional affinity biosensors using fluorescence technology, the great advantage of a real-time biosensor is that it can measure the dissociation rate constant (k_d) which is not trivial with an equilibrium binding assay. In this chapter, the analysis method to calculate kinetic constants (association and dissociation rate constant, k_a, k_d , respectively) and affinity, K_A , K_D from the experimental response will be discussed.

Typically, a biosensor surface is functionalized with the receptors before injecting the analyte. Once the analyte is introduced on the sensor surface, the molecular interaction starts to happen, transducing the response of the sensor, i.e. spectra shifts or impedance change. Figure 2.6 shows the schematic of simple binary binding model.

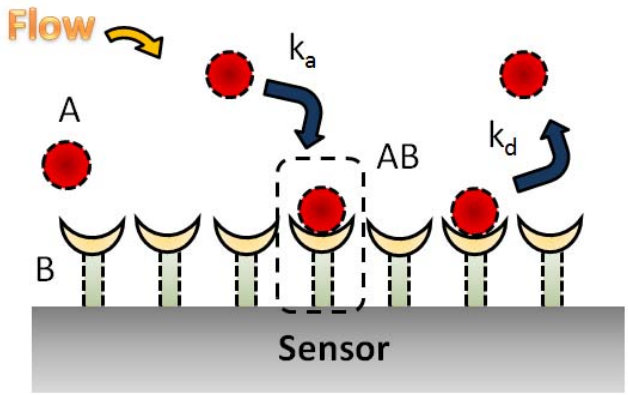

Figure 2.6 Schematic of 1:1 binding model. An analyte molecule (A) is introduced on the sensor surface where a receptor (B) is pre-functionalized. During the binding interaction, a complex (AB) is formed with an association rate constant (k_a). The complex reversibly dissociates with a dissociation constant (k_d).

Here, a receptor (B) is pre-functionalized on the sensor surface and an analyte (A) is introduced, generating a complex (AB) after the interaction. The kinetic model for a 1:1 interaction where one analyte molecule (A) binds with one receptor (B) at a single binding site can be expressed with the reaction scheme such as:

$$\mathrm{A} + \mathrm{B} \underset{k_d}{\overset{k_a}{\leftrightarrow}} \mathrm{AB} \tag{2.42}$$

,where k_a and k_d are association and dissociation rate constants of complex the AB, respectively. Then, the association rate of the complex, AB can be expressed using the concentration of each analyte ([A],[B]) with association and dissociation rate constants:

$$\frac{d[\mathrm{AB}]}{\mathrm{dt}} = k_a[\mathrm{A}][\mathrm{B}] - k_d[\mathrm{AB}] \tag{2.43}$$

After some binding reactions, the initial concentration of free binding site becomes, [B] = $[B]_0$-[AB], thus substitute this into equation (2.43) yields:

$$\frac{d[\mathrm{AB}]}{\mathrm{dt}} = k_a[\mathrm{A}]([\mathrm{B}]_0 - [\mathrm{AB}]) - k_d[\mathrm{AB}] \tag{2.44}$$

,where $[B]_0$ is the concentration of B at $t = 0$. In this 1:1 monophasic model, the response, R is proportional to the amount of AB complexes. Thus, equation (2.44) can be expressed as:

$$\frac{dR}{dt} = k_a C R_{\max} - (k_a C + k_d)R \tag{2.45}$$

, where *dR/dt* is the rate of complex formation, C is the concentration of analyte (A), R_{max} is the response when initial binding sites are all occupied.

2.4.1 Equilibrium binding assays

In equilibrium state, all binding sites are occupied by the anlayte (A), thus $dR/dt = 0$. Thus, the equation (2.45) becomes:

$$0 = k_a C R_{\max} - (k_a C + k_d) R_{eq}, \tag{2.46}$$

,where R_{eq} is the response signal at the equilibrium state. Rearranging the equation (2.46) yields:

$$\frac{1}{R_{eq}} = \frac{1}{R_{\max}} + \frac{1}{K_A R_{\max}} \cdot \frac{1}{C} \tag{2.47}$$

,where K_A is the association constant defined by k_a/k_d. After plotting $1/R_{eq}$ versus $1/C$ and linear fitting, $1/R_{max}$ can be obtained from the y-intercept of the linear curve. K_A can be calculated from the slope of the curve after substituting $1/R_{max}$ value acquired previously.

2.4.2 Real-time binding assays

From the equation of the rate of complex formation (2.45), by solving this first order differential equation, the time dependent response R_t can be expressed as:[55]

$$R_t = \frac{C k_a R_{\max} \left[1 - e^{-((C k_a + k_d) t)}\right]}{C k_a + k_d} + R_i \tag{2.48}$$

, where R_t is a response signal at time t and R_i is an initial signal at the point of analyte is introduced at time $t = 0$. Since the analyte concentration is 0 (i.e. C=0) during the dissociation process, the rate of dissociation can be rewritten as:

$$\frac{dR}{dt} = -k_d R, \tag{2.49}$$

and this can be also expressed in a form of integrated equation:

$$R_t = R_a e^{-k_d t} + R_{t\to\infty} \tag{2.50}$$

, where R_a and $R_{t\to\infty}$ is the response when dissociation process starts and completed, respectively. Generally, from equation (2.50), the dissociation rate constant (k_d) can be obtained from a linear slope in a plot of $\ln(R_a/R_t)$ versus time. After acquiring k_d, the k_a value can be calculated from the time constant, Ck_a+k_d, obtained from a linear slope in a plot of $\ln(dR/dt)$ versus time from equation (2.45).

CHAPTER 3

HIGH-QUALITY, LOW-COST, AND LARGE AREA NANOHOLE ARRAY FABRICATION

Theoretical backgrounds of periodic sub-wavelength hole arrays for SPPs excitation were introduced in the previous chapter. However, for the most part, nanohole arrays have been fabricated using expensive and time-intensive high-resolution serial techniques such as electron beam lithography (EBL) and focused ion beam (FIB) milling. Although nanoimprint technique is designed to make a sub-wavelength size structure over a large area with a high-throughput, it mainly requires the metal etching process which is not trivial for a high quality and large-area (~ cm^2) nanostructure patterning. In this chapter, two novel approaches to fabricate high-quality, large-area nanohole arrays without any expensive optical lithography and metal etching process will be presented. This low-cost, large-area nanohole fabrication method will provide a great benefit to high-throughput SPR imaging. The work presented in the chapter 3.1 is the result of a

collaborative effort with Professor Haynes group (with Dr. Kyle Bantz) and is mainly derived from the following publication:[65]

1. **S. H. Lee**, K. C. Bantz, N. C. Lindquist, S. -H. Oh, C. L. Haynes, *Langmuir* 25 (23), 13685-13693 (2009)

The chapter 3.2 is the result of a collaborative group effort, derived mainly from the following publication:[84]

2. H. Im, **S. H. Lee**, N. J. Wittenberg, T. W. Johnson, N. C. Lindquist, P. Nagpal, D. J. Norris, S. H. Oh, *ACS Nano* (2011) 5 (8), 6244-6253.

3.1 Self-assembled plasmonic nanohole arrays

Since Ebbesen and coworkers discovered extraordinary optical transmission (EOT) through subwavelength noble metal nanohole arrays in 1998,[15,56] there has been significant effort to fabricate nanohole arrays with well-controlled electromagnetic properties. Since the sub-micron patterning requires state-of-the-art photolithography technology for a patterning, which is usually not available in academy, nanohole arrays have been fabricated using expensive but slow high-resolution serial techniques such as electron beam lithography (EBL)[57] and focused ion beam (FIB) milling.[15,58] Even in industry, a deep ultraviolet (DUV) patterning resolution (~ 200 nm) requires incredibly expensive mask and photolithography equipment. To address this fabrication issues, highly intensive efforts have been employed on the novel way to fabricate high-throughput nanohole array fabrication technology having a consistent optical properties.

For this purpose, advanced soft lithography methods such as PEEL (a combination of phase-shift lithography, etching, electron-beam deposition, and lift-off) or soft nanoimprint techniques have been successfully employed to fabricate nanohole arrays.[59,60] In a recent example, Chen et al. fabricated ~ 1 cm^2 size square lattice gold nanohole arrays with sub 250-nm-diameter using UV nanoimprint lithography combined with reactive ion etching and a Cr/Au lift-off process.[61] With this method, various diameters and periodicities of the nanohole were fabricated and systemic shifts in the transmission spectra with structural variations were examined. While these methods have facilitated important fundamental studies, the field would greatly benefit from a simpler massively parallel fabrication method that can pattern nanohole arrays with a deep ultraviolet (DUV) patterning resolution without using an exposure tool, photomask, or imprint mold. As early as 1995, Masuda et al. used an anodic alumina template and multiple polymer/metal deposition steps to achieve a nanohole array structure; however, this work did not focus on topographic tunability, optical characterization, or use the substrate as a surface-enhanced spectroscopy platform.[62]

3.1.1 Nanosphere lithography (NSL)

Nanosphere lithography (NSL) conceived by Deckman et al.[63] and popularized by Van Duyne and coworkers[64] is a simple and very powerful technique to produce various sizes and shapes of nanostructures including nanoparticles, nanoholes, and nanowires.[64-66] Because of its versatile fabrication capability with low-cost, high-throughput, and tunability, it has been widely adopted to make plasmonic substrates for LSPR biosensing

andSERS detection. The first step to start this maskless, inexpensive lithography fabrication is the packing of nano-size colloids on the substrate. Because NSL is based on self-assembly of polymeric nanoparticles, either 2-dimensional (2-D) or 3-dimensional (3-D) structure can be made. The main focus of this thesis, however, lies in the nanohole fabrication, thus, only 2-D monolayer formation will be considered.

Previously, Jiang and McFarland employed a specialized spin-coating technique to create 2D non-close-packed nanospheres for use as a deposition mask[67]. The packing quality was further improved by controlling the force balance between the centrifugal and the surface tension by suppressing the evaporation speed, allowing longer time for the equilibrium state.[68] In this work, they showed a highly homogeneous, closely packed self-assembled monolayer over ~ cm size area. However, the packing quality, i.e. the size of a single crystal, is limited to ~ 10 μm level.

While the simple "drop and dry" method commonly used for nanosphere lithography can produce a relatively large area 2D packed structure (~1 mm^2), it is difficult to obtain a single crystalline domain over a large area. When a droplet of colloidal suspension is placed onto the substrate, it spreads out and forms concentric circles before drying. The convex, dome-shaped structure of the droplet hinders the collision and redistribution of the nanospheres at the drying edge, degrading the quality of 2D packing. In addition, since it is difficult to control the exact area over which the droplet spreads out, the local concentration of the nanospheres is not precisely controlled. Since Nagayama and coworkers observed capillary force-induced 2D self assembly using a Teflon ring,[69] many researchers have been working to improve the quality of the 2D self-assembled structures

by using a concave (instead of convex) meniscus relative to the surface of a substrate.[70-72] Using the concave meniscus facilitates the convective flow and enhances the rearrangement of nanospheres just before leading edge solvent evaporation. To maintain the balance between the nanosphere supply and solvent evaporation, a PDMS well is adopted to encourage formation of a concave meniscus on the substrate and control the local concentration of nanospheres. After the nanosphere packing, a reactive ion etching (RIE) step to shrink the nanospheres is performed before metal deposition, facilitating the formation of nanohole arrays on removal of the nanospheres. By controlling the original nanosphere size, etching time, metal deposition thickness, and metal deposition angle, it is possible to tune the nanohole spacing, size and aspect ratio, and accordingly, the plasmonic properties.

3.1.2 Fabrication method

To obtain the hydrophilic substrate necessary for nanosphere self-assembly, standard glass microscope slides were rinsed with acetone, methanol, isopropyl alcohol (IPA) and deionized water, and then sonicated in a cleaning solution of $NH_4OH/30\%H_2O_2/H_2O$ (volume ratio 1:1:10) for 1 hour. Finally, they were cleaned in a piranha solution ($70\%H_2SO_4/30\%H_2O_2$) for 30 min. After rinsing thoroughly, they were stored in deionized water and dried with high purity N_2 immediately before nanosphere deposition. To facilitate large areas of perfect nanosphere packing, the nanosphere solution spreading area was controlled by the presence of lithographically defined polydimethylsiloxane (PDMS, Sylgard) wells. Standard soft lithography methods were employed to create the

PDMS wells.[73] A negative photoresist, SU-8 50, was spin-coated onto a silicon wafer and patterned to create the master mold. A 10:1 ratio of PDMS and curing agent was degassed in vacuum, cast onto the master mold, and squeezed with a plastic film to remove excess uncured PDMS, creating a 50-200 μm thick layer, and creating holes several millimeters in diameter. After curing the PDMS at 70^{o}C overnight, the PDMS sheet was carefully peeled off and aligned onto the glass slide substrate, defining the PDMS wells for nanosphere assembly. The PDMS wells were reused many times.

Figure 3.1a shows a schematic of the colloidal self-assembly using PDMS-defined assembly areas. After dropping the nanosphere suspension onto the glass slides, a single layer of nanospheres is formed from the center and grows toward the outside as the solution evaporates. To pattern large areas, the nanospheres were diluted in 1:1 (v/v) milliQ water:ethanol to control the concentration and the surface tension at the liquid-vapor interface. A 0.5 μL droplet of the colloidal suspension was placed onto the glass slides within the 3-mm-diameter PDMS-defined holes and dried at room temperature. The closely packed polystyrene nanospheres were then etched with RIE (Reactive Ion Etch, STS320), causing them to shrink while retaining their original crystalline lattice location. A mixture of oxygen and argon gas was used in the etch process with the experimental parameters of O_2(35sccm)/Ar(10sccm), 60mTorr, 60W. After etching the PS nanospheres, an e-beam evaporator (Temescal) was used to deposit a 50 nm thick silver film onto the templated substrate. The substrate holder was rotating during normal incidence deposition, whereas it was not in the case of angled deposition. The evaporation chamber pressure and deposition rate were $5x10^{-6}$ Torr and 1Å/s,

respectively, and the deposition thickness was monitored by a quartz crystal microbalance. Finally, the PS nanospheres were removed with 3M Scotch tape, leaving behind the nanohole array. Residue and any remaining nanospheres were dissolved using dichloromethane and ultrasound sonication at 70W for 20 min. The processing steps for nanohole array fabrication using NSL are illustrated in Figure 3.1b.

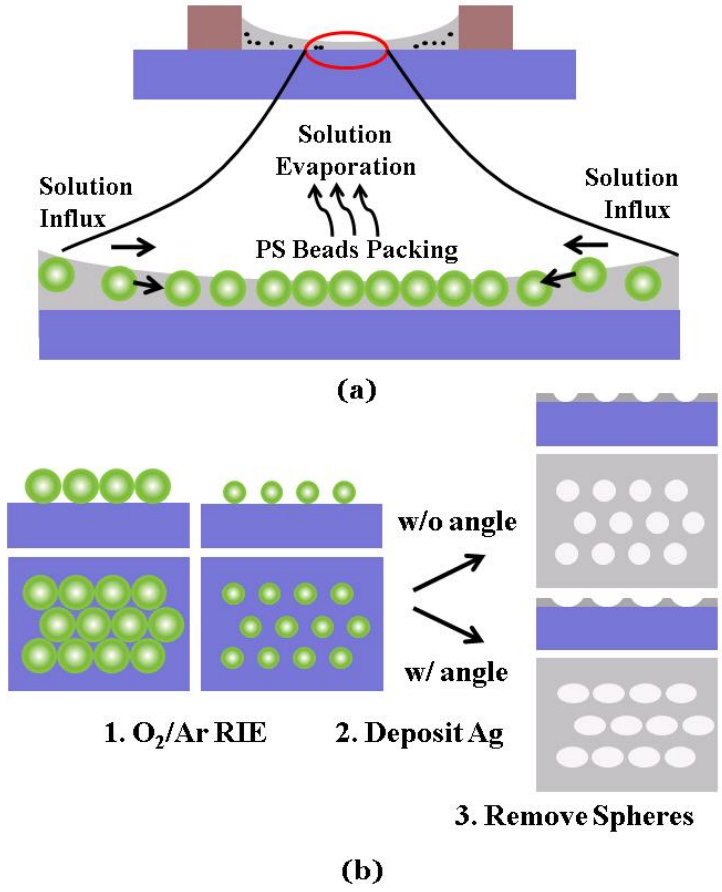

Figure 3.1 Schematic representation of the colloidal assembly. (a) using PDMS-defined areas and (b) process steps for fabricating nanohole arrays using NSL. Figure is adapted from Lee *et al.*,[65]

3.1.3 Large-area self-assembled nanohole arrays

Figure 3.2 shows the scanning electron micrograph (SEM) images of each process step to fabricate self-assembled nanohole arrays. Here, a PDMS well encourages formation of a concave meniscus on the substrate and controls the local concentration of nanospheres, facilitating the formation of a packed monolayer over ~1 mm-diameter region with a typical single crystalline, defect-free domain size of ~30 x 30 μm^2.(Fig. 3.2a) The self-assembly of nanospheres was followed by an RIE process in oxygen plasma to reduce the nanosphere size in a controlled manner. Importantly, the RIE process left the lattice position of each nanosphere intact (Figure 3.2b). Subsequently, a 50 nm-thick Ag film was evaporated onto the nanosphere template (Figure 3.2c), using each size-reduced PS nanosphere as a shadow mask. Then the nanospheres were removed with tape and solvent cleaning. Figure 3.2d shows the nearly defect-free, crystalline nanohole arrays produced by these steps. The average diameter of the hole after bead removal was 196±11 nm and 298±7 nm when using 400 nm-diameter and 600 nm-diameter nanospheres, respectively.

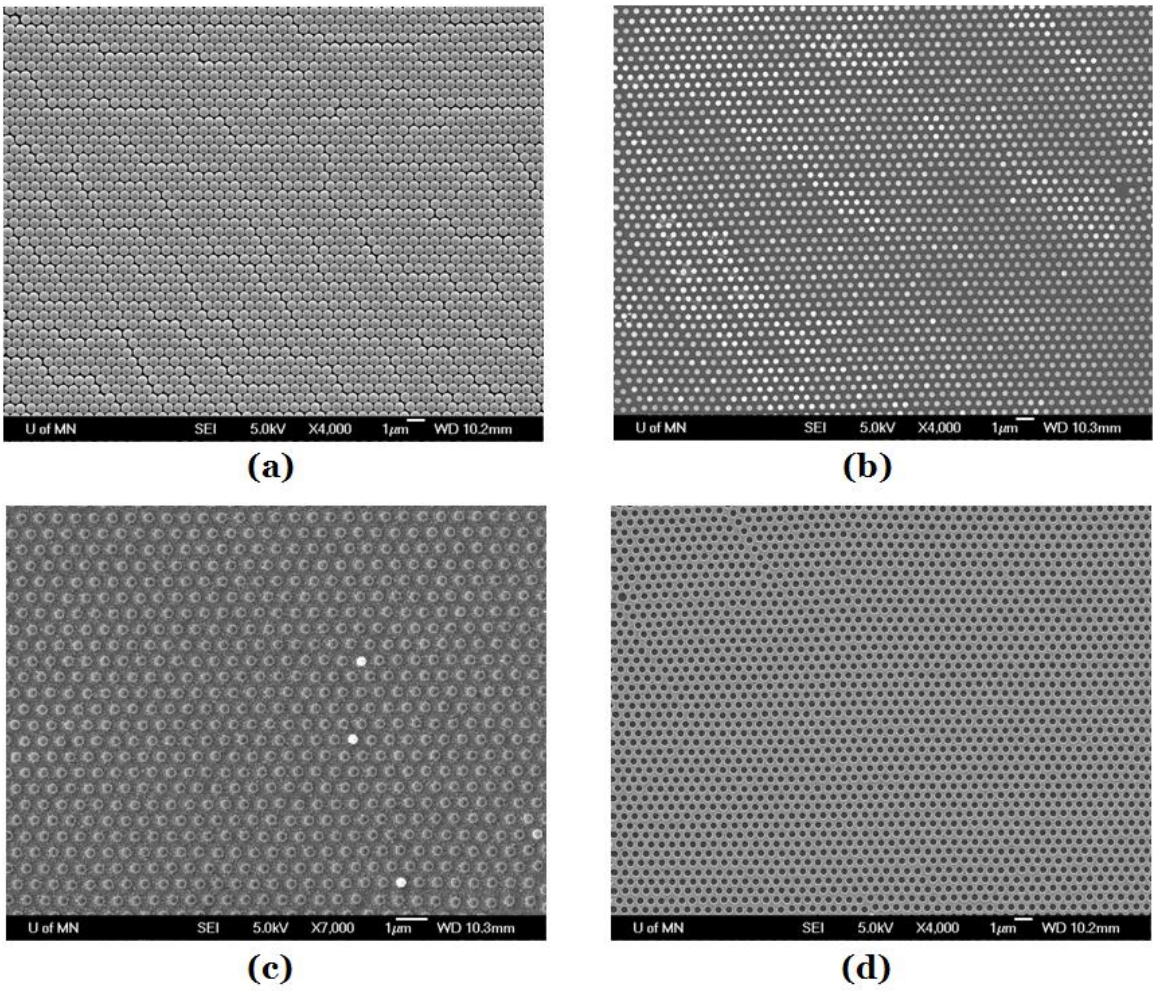

Figure 3.2 Scanning electron micrographs (SEM) of each NSL process step. (a) single layer formation with PS nanospheres (600 nm diameter), (b) nanosphere template after size reduction using reactive ion etching (c) nanosphere template after 50-nm-thick Ag deposition, and (d) the resulting large area (~30 x 30 μm^2) single crystalline hexagonal nanohole array. Figure is adapted from Lee *et al*.,[65]

3.1.4 Hole shape tuning by angle-resolved metal deposition

Using the NSL process, the size of each nanohole can be easily tuned by changing the RIE processing time. Furthermore, elliptical hole shapes can be created by simply tilting the substrate during the metal deposition, adding another degree of freedom to tailor plasmon resonance characteristics of the nanohole arrays,[74-76] shown in Figure 3.3a. This angle-resolved metal deposition technique has been adopted intensively for making various shapes of nanostrucutures.[77-80] The ellipticity of the holes depends on the size of nanospheres and the tilt angle of the substrate — smaller nanospheres with a steeper substrate tilt angle produce ellipses with a higher aspect ratios. Figures 3.3b and 3.3c show SEM images of 45^{o} and 60^{o}, respectively, tilted metal deposition onto etched nanosphere templates before removing the nanospheres. In Figure 3.3d, the aspect ratio measured after removing the nanospheres was 1.6 when the substrate was tilted to 60^{o}.

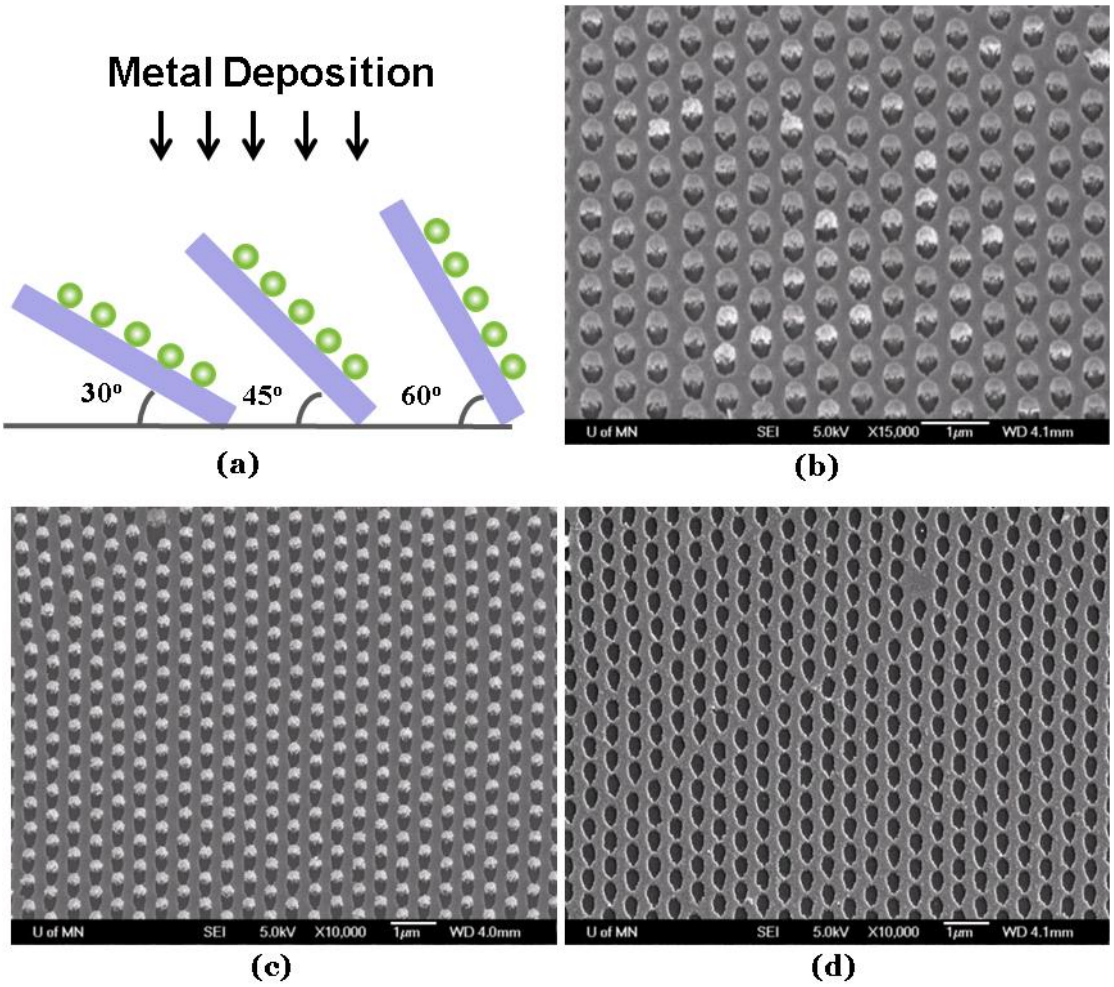

Figure 3.3 Hole size tuning by angle-resolved metal deposition. (a) Schematic illustration of the angle-resolved metal deposition process. Scanning electron micrographs of (b) an elliptical nanohole array (45º tilt angle) before nanosphere removal, (c) an elliptical nanohole array (60º tilt angle) before nanosphere removal and (d) after nanosphere removal. Figure is adapted from Lee *et al*.,[65]

3.1.5 Transmission spectra and FDTD simulation

To evaluate the optical properties of the self-assembled nanohole arrays, transmission measurements were completed on circular nanohole arrays. Figure 3.4a presents the experimental results obtained from substrates with circular holes made using 400-nm-diameter nanospheres. Finite-difference time-domain (FDTD) calculations (Fullwave, Rsoft Design Group) were performed on the analogous structure and are represented as a dashed line. The spectral position of the maximum transmission peaks (λ_{max}) at difference resonance orders and interfaces were predicted by the grating coupling equation.[81]

$$\lambda_{max} = a_0\left[\frac{4}{3}(i^2 + ij + j^2)\right]^{-1/2}\sqrt{\frac{\varepsilon_d\varepsilon_m}{\varepsilon_d + \varepsilon_m}} \qquad (3.1)$$

,where a_0 is the periodicity of the array, the integers (i, j) represent the Bragg resonance orders, and ε_m and ε_d are the dielectric functions of the metal and the dielectric, respectively. Overall, the λ_{max} position between the simulations and the experimental measurements are in good agreement. The (1,0) transmission peaks at the silver/glass interface calculated by FDTD and measured by the spectrometer appear at 672nm and 695nm, respectively. The (1,1) transmission peak at the silver/glass interface and the (1,0) transmission peak at the silver/air interface overlap at ~500nm, resulting in a broader resonance. Maintenance of two separate surface plasmon resonances on one sample will be convenient because it will facilitate a broader range of possible excitation wavelengths that yield good SERS enhancement factors. Although the probe area in the optical measurements was larger than the size of the perfectly crystalline areas, both the

transmitted intensity and the peak wavelengths measured at 9 different locations on the nanohole array sample, as shown in Figure 3.4b, are very similar, centered at λ=695 ± 5 nm.

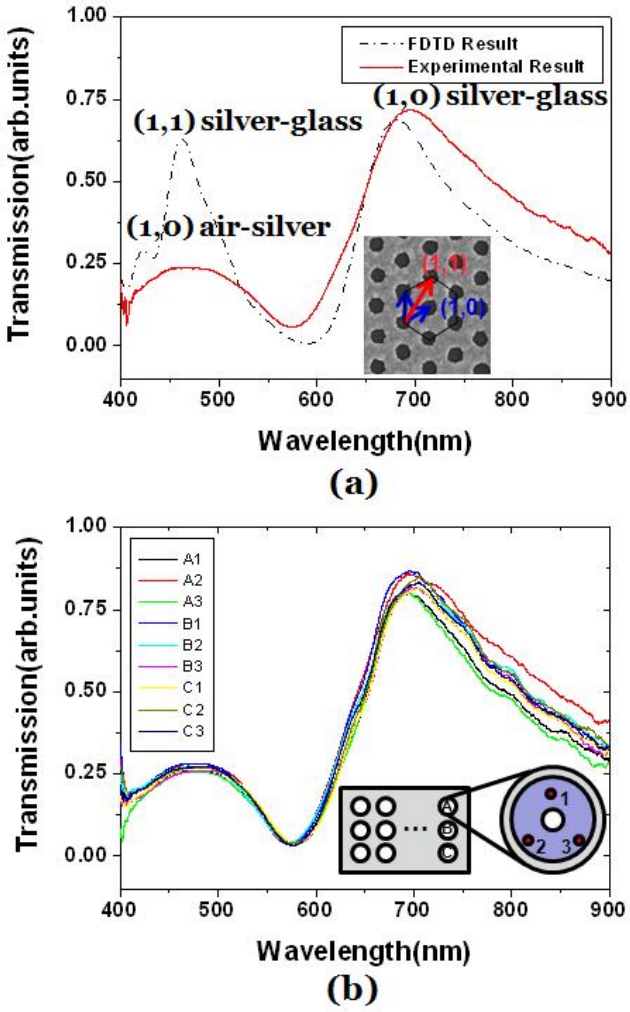

Figure 3.4 Transmission spectra and FDTD simulation of self-assembled hexagonal nanohole arrays. (a) Experimental and computational (FDTD) transmission spectra for a hexagonal nanohole array with a periodicity of 400 nm and a circular hole shape. (Inset) The direction of (1,0) and (1,1) resonances. (b) The experimental spectra measured at nine different locations on a nanohole array substrate. Figure is adapted from Lee *et al*.,[65]

In Figure 3.5a, a time-averaged intensity map of the z-component of the electric field is performed to visualize the electromagnetic field distribution in plasmonic structures. Periodic boundary conditions are used to simulate an infinite hexagonal array with a periodicity of 400 nm. Since the domain size of the fabricated nanohole arrays are larger than the propagation length of the surface plasmon at visible frequencies, ~10 μm on a smooth Ag film, using such periodic boundary conditions are justified. Furthermore, the propagation length of a surface plasmon within an array is reduced due to scattering introduced by the nanoholes. A non-uniform mesh was used for computational efficiency, with a nominal grid size of 5 nm and an edge/interface grid size of 2 nm. The dispersion of the silver film was modeled with a Drude/Lorentzian model fit to experimental dielectric functions. Both electric field maps were extracted from the FDTD calculation at the (1,0) resonance direction (x-axis) at different wavelengths. Light is incident from the top (+z) and excites surface plasmons on the nanohole array at each interface. The optical energy is confined strongly at the air/silver interface with λ_{max} = 422 nm, and to the glass/silver interface with λ_{max} = 672 nm. These results confirm the wavelength of the transmission peak at each interface in Figure 3.4a. Furthermore, the air/silver interface shows high electric field intensity at both wavelengths. Figure 3.5b shows a top-down view of the electric field intensity at the air/silver interface with λ_{max} = 422 nm. As has been seen in previous nanohole modeling, the electromagnetic fields are largely concentrated to the edges of the nanohole features.

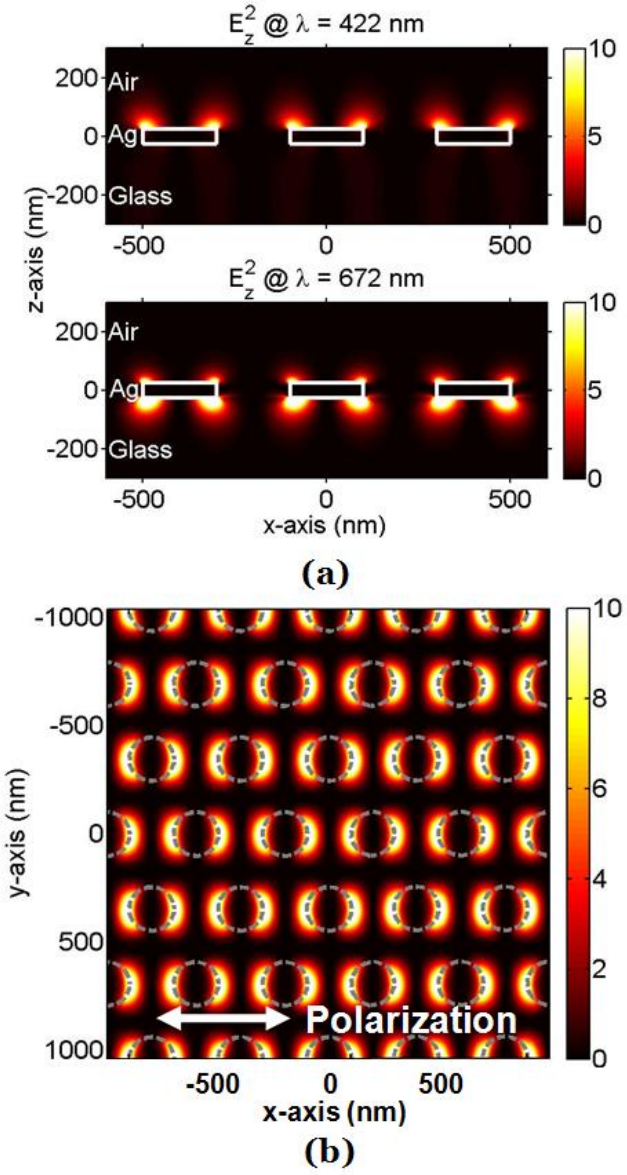

Figure 3.5 A time-averaged intensity map of the z-component of the electric field. (a) Time-averaged intensity map of the plasmonic field (z-component of the electric field) at λ=422nm and λ=672nm. The FDTD result confirms the wavelength of the transmission peak at each interface. (b) A top-down view of the electric field intensity at the air/silver interface at λ=422nm. Figure is adapted from Lee *et al.*,[65] The FDTD image is courtesy of Nathan Lindquist in our group.

3.1.6 Refractive index sensitivity

To evaluate the sensitivity of self-assembled nanohole arrays, the refractive index sensing using different values of index-calibrated ethanol-water solutions was performed. Nanosphere used in the refractive index sensing has a 500-nm-diameter. After shrinking the sphere diameter, a 50 nm-thick Ag film was evaporated onto the nanosphere template. Based on the λ_{max} equation, the resonance minimum observed at 565 nm is that of the water-silver interface (Fig. 3.6). When the refractive index increases from 1.333 to 1.363 in steps of 0.1 refractive index units (RIU), the spectrum shifts linearly due to the increase of refractive index near sensing surface. The bulk refractive index sensitivity, evaluated from the shift of peak wavelength over the change of refractive index unit (RIU), is 333 nm/RIU. (10 nm shift / 0.03 RIU change)

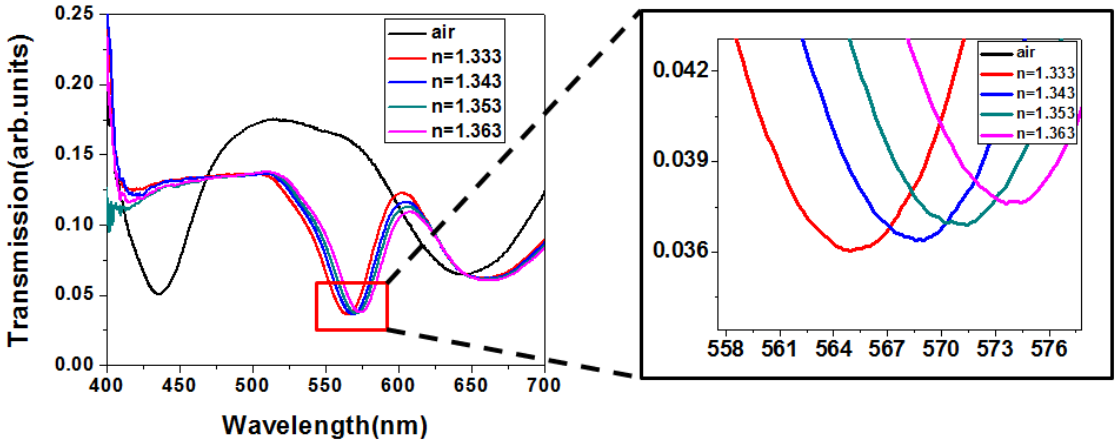

Figure 3.6 Refractive index sensitivity of self-assembled nanohole arrays. The transmission spectrum shifts after injecting the index-calibrated ethanol-water solutions. The refractive index sensitivity measured from spectral shift versus refractive index units (RIU) change is 333 nm / RIU.

3.2 Nanohole arrays fabrication via template stripping

Although NSL is a low-cost and versatile technique, allowing the high-throughput nanohole fabrication, it cannot produce perfect single crystalline periodic arrays over a large area due to its character of natural lithography. In addition, it is not trivial to make optically thick (> 100 nm) nanohole arrays which can block the direct transmission through the film. Furthermore, the standard deviation (SD) of spectral position from NSL is larger than the general level of spectral shift during SPR biosensing (~ 1 nm) due to the multiple-orientation of nanohole array crystals. Therefore, it is inevitable to develop advanced nanohole array fabrication method which satisfies both the high-throughput and high-integrity needs simultaneously.

In 2009, Nagpal et. al. reported simple but highly versatile nanostructure fabrication technique, called template stripping.[82] Template stripping exploits the poor adhesion between noble metals such as Au or Ag and a Si substrate. The beauty of this method becomes apparent when it combines with the fully matured Si nanofabrication technology. Once high-fidelity Si templates such as pyramids, bumps, lines are prepared, the metal pattern exactly follows the outline of the templates during a deposition. However, a different approach is required for the nanohole array fabrication via template stripping. Unlike other continuous metal structure such as pyramids and/or bumps, metals deposited on and in the hole of Si template should be discontinuous to make a hole. Therefore, poor step coverage during metal deposition is strongly required to make clean nanohole arrays. To accomplish this requirement, it is crucial to make the sidewall of the Si template

vertical. In the next chapter, the efforts to address this requirement will be discussed with a very detailed Si template fabrication process. After showing each step of fabrication process, real-time biosensing results using template-stripped nanohole array will be presented.

3.2.1 Fabrication method

Due to the enormous efforts and investments in the semiconductor industry, Si etching process has advanced with incredible speed. Generally, there are three well established principles for Si etching: chemical, physical, and ion-enhanced etching. Because chemical etching has a very selective but isotropic behavior, it is not an appropriate approach for template stripping Si template fabrication. Reactive ion etching (RIE) is a well established process for anisotropic Si etching. In principle, etching is done by reactive neutral species, such as "free radicals". Most common free radicals using for Si or SiO_2 etching is a fluorine-base gas such as CF_4 or SF_6 gas.[83]

$$\begin{aligned} e^- + CF_4 &\rightarrow CF_3 + F + e^- \\ e^- + SF_6 &\rightarrow SF_5 + F + e^- \end{aligned} \qquad (3.2)$$

To increase the etch rate, a small amount of O_2 gas can be added to reduce CF_3 + F recombination. During the Si etching process, by-products (SF_4) are removed continuously in the low-pressure vacuum chamber.

$$4F + Si \rightarrow SF_4 \qquad (3.3)$$

Based on this Si and SiO_2 etching theory, Si template fabrication process starts with the nanopatterning on the thermally grown SiO_2 oxide hard mask. The nanoimprint stamp contains a periodic array of Si posts (210 nm in diameter, 350 nm in height and 500 nm in periodicity) over an 8 mm × 8 mm area. A NXR-1025 nanoimprint resist was spin-coated on a Si chip at 3500 r.p.m. for 60 sec and cured at 150 °C for 1 min. (Heptadecafluoro-1,1,2,2-tetrahydrodecyl)trichlorosilane anti-sticking layer was formed on the nanoimprint Si stamp for 12 hours prior to the imprinting. Then, nanoimprint was performed with a pressure of 300 psi for 2 min at 130 °C (Fig. 3.7a). After transferring imprinted pattern on SiO_2 layer by reactive ion etching, anisotropic vertical Si etching was performed to make the periodic nanohole Si template (Fig. 3.7b). Two approaches are applied for anisotropic SiO_2 and Si etching. Although CF_4 gas shows a slow etch rate than SF_6 gas, etched profiles show more homogenous surface. Therefore, CF_4 based gas combination is used for SiO_2 oxide mask etch. For Si template etching, SF_6 based gas combination is used with oxide hard-mask since it provides a better sidewall profile. A detailed process condition is presented in Appendix B.

After Si etching process, a 100-nm thick Ag film was deposited on the mold cleaned in a 1:1 mixture of sulfuric acid and hydrogen peroxide (Fig. 3.7c). During the metal deposition, holes are perforated automatically due to the vertically etched holes in the Si template. Then, the Ag film was covered by a UV-curable optical epoxy with a glass slide and epoxy is cured under UV light. Finally, the metallic film was peeled off from the template to reveal the patterned nanohole arrays (Fig. 3.7d). By using this novel nanohole fabrication method, large-area, high-fidelity nanohole arrays can be fabricated

from one metal deposition without using any additional lithography, etching process. After cleaning the Si templates using a 1:1 mixture of sulfuric acid and hydrogen peroxide for 10 min, they can be reused more than 30 times.

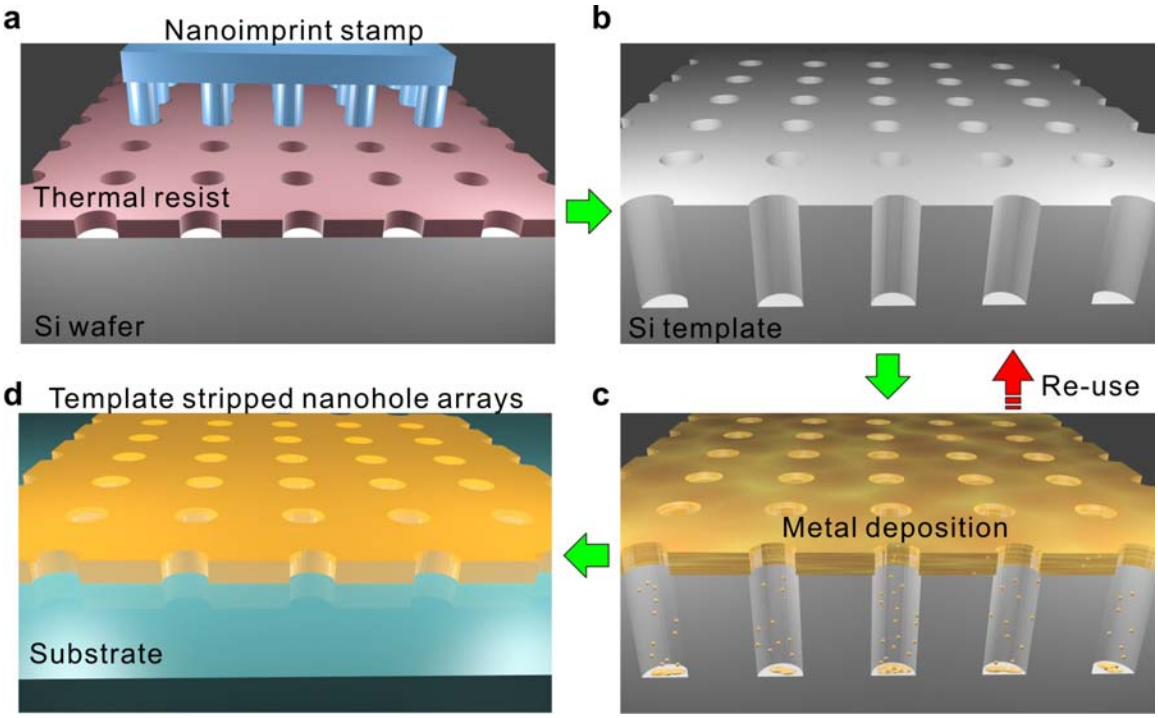

Figure 3.7 Schematic for fabricating the large-area nanohole arrays. (a) A thermal resist layer spun on a Si wafer is imprinted with a nanoimprint stamp with circular post patterns (b) The Si wafer is subsequently etched to be a nanohole template with deep circular trenches (c) A metal film is directionally deposited on the Si template (d) The metal surface is coated with a thin layer of epoxy and covered with a glass slide. The Ag film is then peeled off of the template to reveal the smooth nanohole array made in the metal film. The Si template can be reused to make multiple identical samples. Figure is adapted from Im and Lee *et al*.,[84]

3.2.2 Template-stripped nanohole arrays

Figure 3.8a shows a top-down scanning electron microscope (SEM) image of a patterned Si template. The diameter of Si template nanohole is ~ 210 nm which has a similar value to that of the Si nanoimprint mold. Figure 3.8b shows a cross-sectional SEM image of the template after deposition of a 100 nm-thick Ag film. Because the sidewall profile is vertical, the metal deposited above the hole falls inside the hole. Top and bottom/side metal remains disconnected. Thus, the nanohole patterns are created automatically during the metal evaporation process. Figure 3.8c shows a SEM image of a template-stripped Ag nanohole array. The hole diameter and periodicity of nanoholes are about 180 and 500 nm, respectively. Hole shape is not perfectly circular after the template stripping due to the lateral growth of metal during the deposition. However, transmission spectra does not show any singularities. A photograph of the fabricated nanohole array chip on a glass slide is shown in Figure 3.8d. The periodic nanohole arrays were made in an 8 mm × 8 mm area centered in a 100-nm-thick Ag film with an area of 26.5 mm × 26.5 mm.

One advantage of template-stripping method is that it results in ultra-smooth metal surface. Contrary to the top surface where the deposited metal film shows standard evaporated roughness (Fig.3.9a), the bottom side shows improved surface smoothness since the deposited metal follows the roughness of the Si template (Fig. 3.9b). Figure 3.9c shows root-mean-square (RMS) roughness and their standard deviation of Si template, as-deposited Ag film, and template-stripped Ag film, respectively. It clearly shows improved surface smoothness of template-stripped metal film (1.45 ± 0.2 nm) compared with as-deposited Ag film (4.8 ± 1.2 nm).

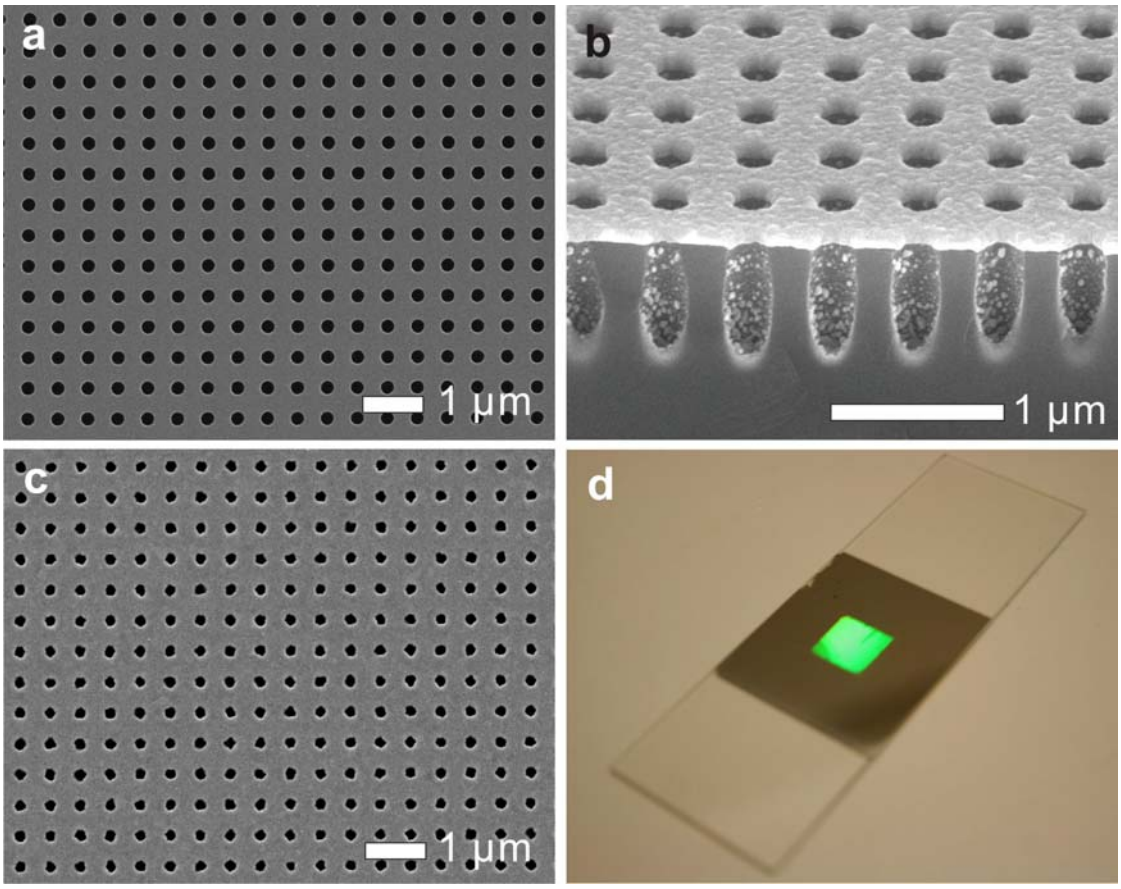

Figure 3.8 SEM images of template-stripped nanohole arrays. (a) A scanning electron microscope (SEM) image of the Si mold with circular deep trenches. (b) A cross-sectional SEM image of the Si mold after depositing a 100 nm-thick Ag film. (c) A SEM image of template-stripped Ag periodic nanohole arrays. The size and periodicity of nanohole arrays are 200 and 500 nm, respectively. (d) A photograph of the fabricated nanohole array chip. A 26.5 mm × 26.5 mm size of 100 nm-thick Ag film with nanohole patterns in a 8 mm × 8 mm area in the center is transferred on a standard microscope slide. Figure is adapted from Im and Lee *et al*.,[84]

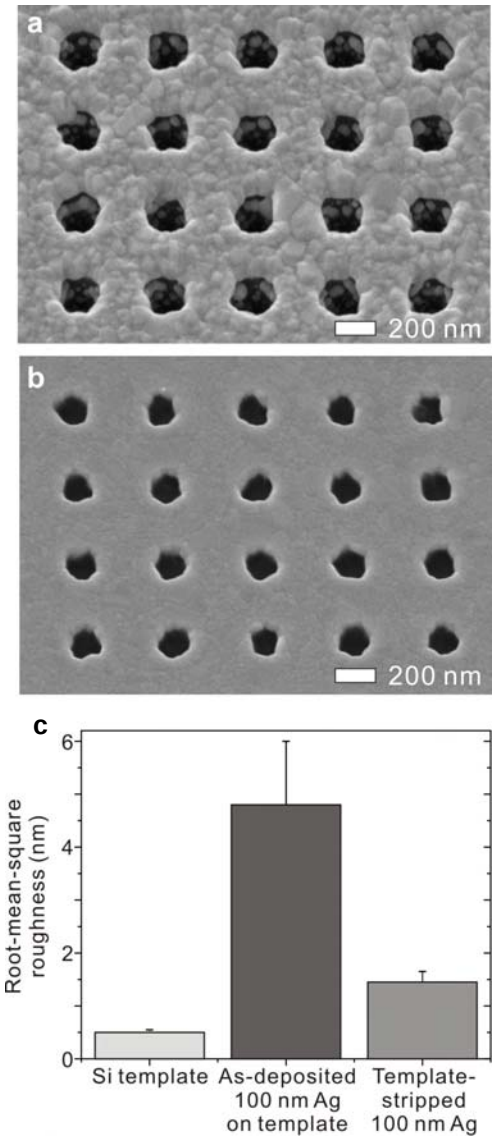

Figure 3.9 SEM images of top and bottom side of metal surface. (a) a 100 nm-thick evaporated silver film deposited on the Si mold and (b) template-stripped Ag nanoholes peeled off of the mold in (a). (c) The table shows root-mean-square (RMS) roughness and their standard deviation of Si mold, evaporated and template-stripped silver films. Template-stripped Ag film shows improved surface smoothness (1.45 ± 0.2 nm) compared with as-deposited Ag film (4.8 ± 1.2 nm). Figure is adapted from Im and Lee *et al.*,[84]

3.2.3 Transmission spectra and refractive index sensitivity

To characterize the optical property of template-nanohole arrays, transmission spectra was measured. A tungsten-halogen light source illuminated the top surface of the nanohole array through a microscope objective (5x, NA=0.15) and the directly transmitted light was collected by a fiber-optic spectrometer (Ocean Optics, USB-4000). Figure 3.10a shows optical transmission spectra of template-stripped nanohole arrays with varying values of refractive index solutions over the nanohole arrays using a microfluidic channel. The refractive index solution was prepared by mixing water and ethanol and injected sequentially. The transmission spectra were normalized by the spectrum of the incident light source. When the refractive index increases from 1.333 to 1.353 in steps of 0.1 refractive index units (RIU), the spectrum shifts linearly due to the increase of refractive index near sensing surface. Figure 3.10b shows the spectral shift of the transmission minimum around 700 nm as the refractive index of the water-ethanol mixture as shown in Figure 3.10a. The measured bulk sensitivity is 450 nm/RIU (RIU = refractive index unit).

Since most bimolecular binding events on receptors occur within tens of nanometers from the sensing surface, it is critical to characterize the surface sensitivity of the device. To quantify the local detection sensitivity, atomic layer deposition (ALD) of silica is used for layer-by-layer characterization of the spectral shifts. The controlled deposition of a conformal dielectric overlayer on the top and bottom surfaces as well as the sidewalls of the nanohole, analogous to the adsorption of biomolecules, provides a useful method to characterize the sensitivity and dynamic range of SPR biosensors.[85,86] The spectral shifts

were measured after depositing sequential 5-nm thick silica overlayers. For comparison, control samples of nanohole arrays made in evaporated and template-stripped Ag films using FIB were also characterized. Figure 3.10c shows the spectral shifts of the template-stripped nanohole arrays with the two control samples. The sensitivity of the template-stripped nanohole arrays is similar to the nanohole arrays made by direct FIB milling in a template-stripped Ag film. But, it decreased when the nanohole were made with FIB in as-deposited rough Ag films. The improved sensitivity can be explained with the increased SPP life time due to the smooth surface. Since SPPs are tightly bound to the metal surface, they are very sensitive to nanometric geometry. Previous work demonstrated that the SP propagation lengths on ultrasmooth template-stripped (sub-1-nm roughness) Ag films increased by a factor of 5 to 7 in the visible regime compared with standard evaporated Ag films.[82] In a periodic nanohole system, however, the smooth region between adjacent holes is only a few hundred nanometers in size, and SPs also scatter strongly from each nanohole. Thus, the optimization of the EOT spectra requires the suppression of the SPP re-radiation by controlling the roughness of the metal surface as well as tuning the nanohole diameter. The effect of hold diameter on the linewidth of the EOT spectra will be discussed in the chapter 4. Nevertheless, template-stripped Ag nanohole arrays include the benefits of high-throughput and low-cost fabrication in addition to the smooth metallic surfaces that improve the overall performance. Also, template-stripped smooth metallic films can produce high-quality self-assembled monolayers, which is useful for biological and chemical applications.[87] Figure 3.10d shows the simulated distribution of electric field intensity ($E_x^2 + E_y^2 + E_z^2$) around

nanoholes before and after depositing the 15-nm-thick silica overlayer. It can be seen that the sizes of hot spots, where strong resonant fields are concentrated around the edges of nanoholes, are bigger than the thickness of silica layer and the presence of the overlayer does not reduce the intensity of the field.

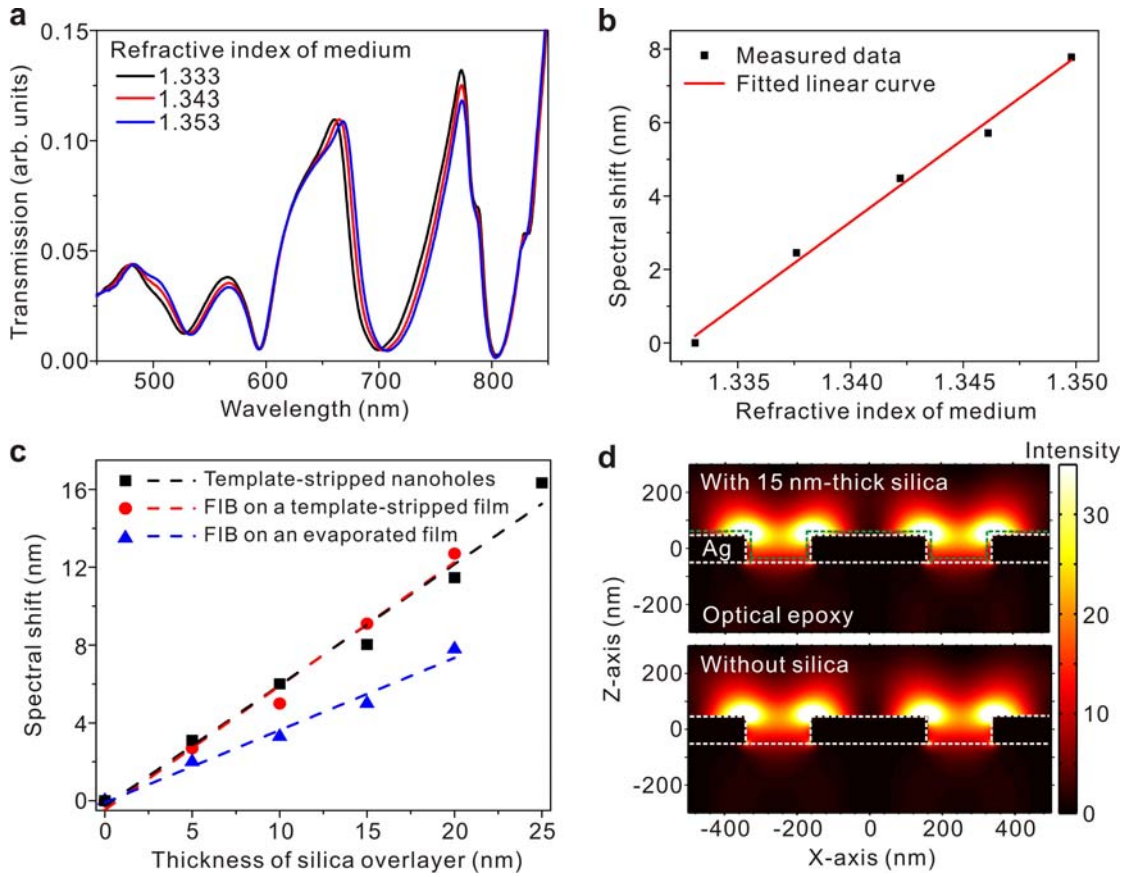

Figure 3.10 Transmission spectra and the device sensitivity of template-stripped nanohole arrays. (a) Experimentally measured optical transmission spectra of the fabricated nanohole arrays with 180 nm hole size and 500 nm periodicity made in a 100 nm-thick Ag film as the bulk refractive index of medium on the Ag film varies from 1.333 to 1.350. (b) Bulk refractive index sensitivity measurements of the fabricated nanohole arrays shown in panel (a). The spectral shifts are measured as the refractive index of a water-ethanol mixture changes from 1.333 to 1.350. The calculated bulk sensitivity is 450 nm/RIU (RIU = refractive index unit). (c) Local sensitivity measurements of template-stripped nanohole arrays with two control samples made by FIB milling on a template-stripped (smooth) and an evaporated (rough) Ag film. (d) 3-D FDTD simulation of the time-averaged surface plasmon (SP) field intensity for template-stripped nanohole arrays with and without a 15-nm-thick silica overlayer. Figure is adapted from Im and Lee *et al*.,[84]

3.2.4 ALD silica shells for supported lipid bilayers (SLBs) formation

For biosensing applications, the metallic surfaces need to be modified with molecular recognition elements. Au films are generally preferred for this purpose because they are chemically inert, non-cytotoxic, and amenable to well-established surface-modification protocols using self-assembled monolayers. Many groups have also investigated the use of Ag plasmonic structures since they are less expensive than Au while exhibiting lower SP propagation losses in the visible spectrum.[84,88,89] Working with Ag films, however, often presents challenges since they oxidize readily in air and water, and deposited Ag films are inherently rougher than Au films.[82] To avoid unwanted oxidation of Ag surfaces, a 15 nm-thick silica overlayer was coated by atomic layer deposition (ALD).[90] Capping the Ag nanohole array with a hydrophilic silica film not only protects its surface but also enables the use of standard surface modification techniques to covalently attach biomolecules or create a supported or suspended lipid bilayer.[84,91,92] As shown in Figure 3.10c, the spectral response of the Ag nanohole array remains linear with the deposition of silica overlayers up to the thickness of ~25 nm, indicating that a 15-nm-thick overlayer still provides sufficient sensitivity. In fact, the refractive index of protein layers and phospholipid bilayers are close to the refractive index of silica,[93,94] making silica overlayers a useful model for estimating the sensitivity and probing range of plasmonic nanosensors.

Supported lipid bilayers (SLBs) are commonly employed biomemetic structures that allow lipid bilayers to be interfaced with solid state sensors and microfluidics and facilitate incorporation of membrane receptors.[95] The simplest method to form a SLB is

the spontaneous rupture of vesicles on a hydrophilic surface.[96-99] To facilitate formation of a SLB on nanohole arrays, the template-stripped nanohole arrays were encapsulated by a 15 nm-thick silica layer deposited by ALD. After allowing Rhodamine-PE labeled vesicles to rupture on silica-coated template-stripped smooth surfaces and nanohole arrays, confocal microscopy and fluorescence recovery after photobleaching (FRAP) were used to characterize the resulting fluorescent SLBs. FRAP confirms that the SLBs formed on both nanohole array and flat areas are continuous and allow free planar diffusion of lipids. Figure 3.11a shows fluorescence images from different time points during a FRAP experiment for a SLB on a template stripped nanohole array. The nanoholes are not visible in fluorescence mode; however the presence of nanoholes was confirmed by viewing the sample in transmission mode. After photobleaching, fluorescent lipids diffuse into the bleached area and bleached lipids diffuse outward, resulting in the recovery curves shown in Figure 3.11b. Notably, the calculated diffusion coefficient (D) is lower for SLBs over nanohole arrays. The diffusion coefficient over the arrays (D_{array}) was calculated to be 1.90 ± 0.15 $\mu m^2/s$, while over flat surfaces the diffusion coefficient (D_{flat}) was calculated to be 2.25 ± 0.09 $\mu m^2/s$ (mean ± standard deviation). Using an unpaired t-test to compare the means returns a P-value of 0.001, indicating that there is a statistically significant difference between the diffusion coefficients. The lower diffusion coefficient over the nanoholes indicates that the membrane probably follows the contours of the nanoporous surface.[100] After thorough washing, the SLBs showed uniform fluorescence on both the flat template-stripped areas, as well as the nanohole arrays. Brighter fluorescence intensity from the nanohole array

side is because the membrane has more effective surface area because it conforms to the nanoholes. Also fluorescence intensity is probably enhanced by surface plasmons excited by the nanohole arrays in the Ag film.(Figure 3.11c)

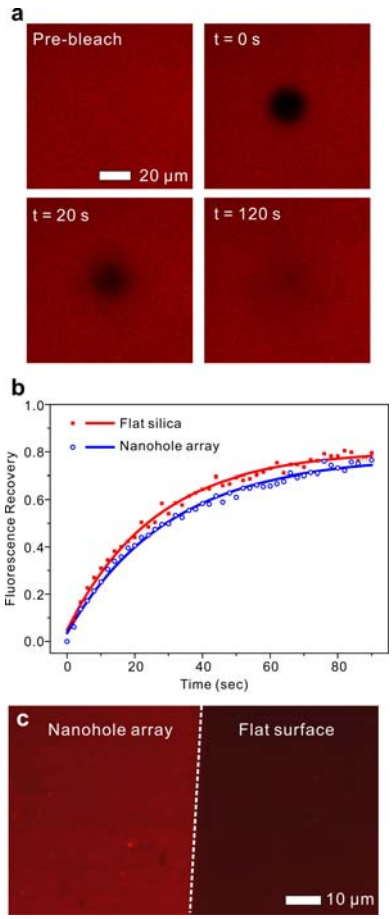

Figure 3.11 Fluorescence recovery after photobleaching (FRAP) for characterizing the SLBs formation. (a) Frames from a fluorescence recovery after photobleaching (FRAP) experiment on an egg PC lipid membrane on the silica-coated Ag nanohole array. The time of recording for each frame is indicated in the top left corner. (b) Representative FRAP recovery curves for an egg PC membrane on the silica-coated flat surface (red squares) and a nanohole array (blue circles). (c) Fluorescence image of egg PC lipid membrane with 1% Rhodamine-PE formed over the boundary of a nanohole array and flat surface areas. The white dashed line shows the boundary and the left and right sides correspond to nanohole array and flat surface areas, respectively. Figure is adapted from Im and Lee *et al*.,[84]

3.2.5 Real-time SPR biosensing

For SPR biosensing of molecular binding on SLBs, a template-stripped silica-coated Ag nanohole array was assembled with a PDMS microfluidic chip, which has 12 linear channels (250 μm channel width and 250 μm channel spacing). After connecting tubes to inlet and outlet ports, a PBS solution was injected into the channel with a constant flow rate of 30 μl/min for at least 10 min. Next, a 1 mg/ml of lipid vesicle solution in Tris buffer containing calcium was injected into the channel and incubated for 1 hour with a reduced flow rate of 2 μl/hr. This was followed by PBS washing for at least 30 min with 50 μl/min to remove excess vesicles. For binding assays, biotin and streptavidin were chosen because it is a well-characterized system with strong specific binding affinity. Also biotin is easily incorporated in the lipid membrane via biotinylated lipids and fluorescently conjugated streptavidin is commercially available. Fluorescently conjugated streptavidin is advantageous because it allows simple confirmation of SPR results by fluorescence microscopy. For binding assays, different amounts of biotinylated-phosphatidylethanolamine (biotin-PE) were incorporated into egg phosphatidylcholine (egg PC) vesicles and SLBs of the mixtures were formed in each channel by rupture of the vesicles.[101] A biotin-free egg PC membrane was used as a negative control. After 5 min of baseline with PBS, a 100 nM solution of streptavidin-R-Phycoerythrin (SAPE) was injected for 15 min. The flow rate was kept constant at 30 μl/min. Figure 3.12a shows binding kinetics between 100 nM SAPE and egg PC lipid membranes with 0, 1, 5, and 10% (w/w) biotin-PE as well as 1% (w/w) nitrobenzoxadiazole-conjugated phosphatidylethanolamine (NBD-PE). The spectral shift was recorded every 2 sec and

plotted without any further data processing. The spectral shift shown from the biotin-free egg PC membrane contains a bulk refractive index change and non-specific binding of SAPE. Therefore, the net shift only due to specific binding of SAPE to biotinylated-PE can be obtained by subtracting the kinetic response between SAPE and the biotin-free egg PC membrane from those between SAPE and biotinylated-PE membranes as shown in Figure 3.12b. The net shift after subtracting the signal from the negative control channel is linearly proportional to the percent biotinylated-PE in the SLB, which indicates specific binding between SAPE and biotinylated-PE can be quantitatively measured from the differential sensing. Figures 3.12c and 3.12d show fluorescence images and intensities of NBD and SAPE after the kinetic experiments shown in Figure 3.12a. The fluorescence intensities of NBD conjugated in the lipid membranes from the four channels are all similar regardless of the amount of biotinylated-PE, but the intensity of SAPE fluorescence increases linearly as a function of the amount of biotin-PE in the SLB. This confirms that the spectral shifts shown in Figure 3.12b result from specific binding between SAPE and biotinylated-PE membranes.

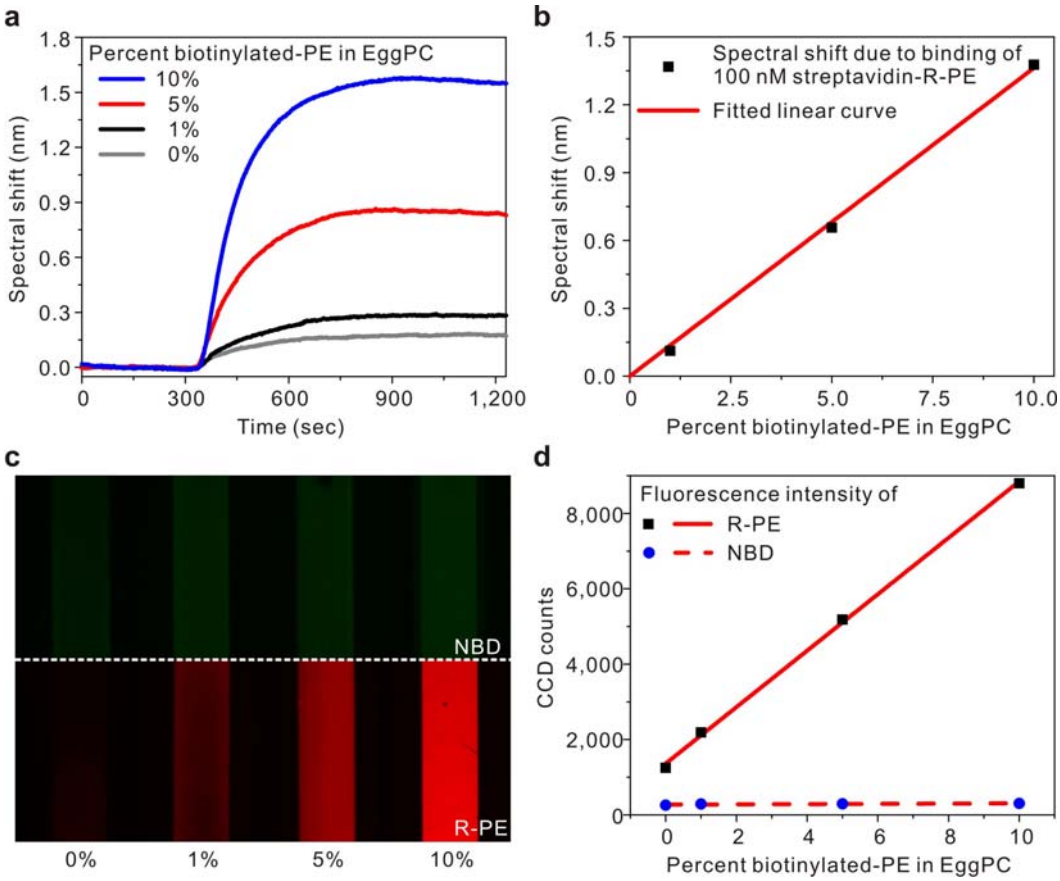

Figure 3.12 Real-time SPR biosensing with biotinlayted lipid membrane and streptavidin. (a) Real-time kinetic measurements of 100 nM of streptavidin-R-Phycoerythrin (SAPE) and 1, 5, and 10% biotinylated and non-biotinylated lipid membranes. After a 5 min baseine with a PBS solution, 100 nM of SAPE solution is injected and incubated for 15 min. The flow rate is kept constant at 30 µl/min and data point were recorded every 2 sec. (b) The net spectral shift obtained by subtracting the spectral shift from the binding of SAPE to the non-biotinylated lipid membrane. In this way, shifts due to bulk refractive index change and non-specific binding of streptavidin-R-PE are eliminated. (c) Fluorescence images of four channels of nanohole arrays. From the leftmost channel, the percent biotinylated-PE in egg PC membrane increases from 0 to 10 %. The lipid membranes are tagged by 1% nitrobenzoxadiazole (NBD). Then 100 nM of SAPE are injected through the channels for 15 min. (d) The fluorescence intensity of NBD in the lipid membranes and R-PE after binding with 100 nM streptavidin-R-PE as shown in (c). Figure is adapted from Im and Lee *et al*.,[84]

3.3 Conclusion

In conclusion, this chapter demonstrated two novel approaches to achieve a high-quality, low-cost, and large-area plasmonic nanohole arrays. First, nanosphere lithography (NSL) was applied for producing self-assembled nanohole arrays without any expensive photo-lithographic tools. After optimizing all process conditions such as nanosphere packing, bead size reduction, and metal deposition, a large defect-free areas (>30 x 30 μm^2) of noble metal nanohole arrays across a mm-sized patterning area was produced with a massively parallel process. By controlling the original nanosphere size, etching time, metal deposition thickness, and metal deposition angle, it is possible to tune the nanohole spacing, size and aspect ratio, and accordingly, the plasmonic properties. In addition, the nanohole profiles can be varied simply by controlling the deposition angle onto the etched nanosphere template. The optical transmission properties of the nanohole arrays are extremely homogeneous across a sample, revealing homogenous nanohole array quality across positions and samples.

To address the limit of self-assembly process such as the polycrystalline nanohole arrays, template stripping method was applied for the high-throughput, high-quality nanohole fabrication over a large area (~cm^2). Si templates were fabricated by nanoimprint, followed by the RIE for anisotropic Si etching. A batch metal evaporation process completes the patterning of nanohole arrays in every mold simultaneously. After curing with an optical epoxy, the patterned metallic films can be peeled off just prior to use to avoid unwanted contamination or oxidation. Because of the uniform Si trenches, template-stripped nanohole arrays show extremely homogeneous sensitivity and optical

properties across positions and samples. To confirm the utility as a biosensor, SLBs formation and real-time binding kinetics were evaluated. Since the master templates can be reused multiple times after a template-cleaning, this fabrication technique will benefit a lot for whom very extensive proteomics research is needed or high-resolution lithography equipment is hard to access.

CHAPTER 4

LINEWIDTH-OPTIMIZED EXTRAORDINARY OPTICAL TRANSMISSION (EOT)

Engineered metallic nanostructures can exhibit unusual optical properties not found in natural materials. With proper design, tuning, and high-throughput fabrication discussed in the previous chapters, such metallic nanostructures can be tailored for practical applications such as biosensing, spectroscopy, imaging, and photovoltaics. For biosensing, it is highly desirable to obtain sharp resonance peaks because the spectral shift can be distinguished clearly even at the small amount of binding, increasing the dynamic range of sensor. This essential requirement can be accomplished by reducing the radiative damping of SPPs through the nanoholes or the material damping in the metals. In this chapter, the roles of nanohole diameter and dielectric functions of metal for the linewidth of EOT peaks will be investigated. Template stripping will be employed again to obtain an ultra-smooth, small hole-diameter. The work presented here is mainly derived mainly from the following publication:[225]

1. S.H. Lee, *T. W. Johnson*, *N. C. Lindquist*, *H. Im*, *D. J. Norris and S.-H. Oh*, Advanced Functional Materials (2012), Accepted

4.1 Roles of SPPs for ultra-sharp resonance

Following the discovery of extraordinary optical transmission (EOT) through periodic subwavelength hole arrays in metal films,[15] extensive research has been conducted to both understand the physical transmission mechanism[46,47,102,103] and practically produce these nanostructured films with high throughput for emerging applications in plasmonics and nanophotonics.[60,61,84,104-107] In EOT, the excitation of surface plasmon polaritons (SPP) in metallic films leads to a series of optical transmission peaks. The SPP excitation conditions and the peak transmission wavelengths are determined by geometrical parameters (hole size, shape, periodicity, and film thickness) as well as dielectric functions of the metal film and surrounding medium.[103] In addition, the far-field EOT peaks exhibit an asymmetric profile described by the Fano-type interference between direct transmission through the holes and the resonant surface modes.[48,51,52,104,108,109]

The spectral linewidth is mainly determined by damping of SPP waves due to ohmic losses from metal as well as radiative damping through the holes. It is advantageous to use a sharp resonance peak for biosensing and spectroscopy, because it is then easier to detect very small changes in the transmission spectra with a high signal-to-noise (S/N) ratio. To accomplish this, one needs to simultaneously reduce radiative damping by tuning the hole size, minimizing the optical losses at visible frequencies by producing extremely high-quality metal films. Since SPPs are tightly bound to the metal interface, they are very sensitive to nanometric geometries – an attribute good for sensing but that

also makes SPPs vulnerable to any random surface roughness and grain boundaries in the metal film. Because as-deposited metal films exhibit rough top surfaces, there is often a mismatch between theoretical calculations and measured device performance. Previously introduced template stripping technique can resolve this problem and produce atomically smooth metallic surfaces with improved optical performance. [82,84] Another advantage of template-stripping process is the simple tunability of the diameter of a metallic nanohole. As the deposition thickness increases, the metal slowly grows laterally, resulting in a smaller hole diameter than the original mold. Therefore, the investigation to acquire sharp resonance peaks will be started by re-visiting template stripping process.

4.2 Hole diameter control via template stripping process

Previously, template stripping has been employed to make nanohole arrays in metal films with a hole size down to 200 nm.[82,84] To reduce the radiative damping by nanoholes, additional approach was attempted to improve the process, reducing a nanohole size further down to ~100 nm, sharpening the EOT peaks while achieving extremely uniform optical properties across cm-sized metal films using well-developed template stripping process. During the metal evaporation on the Si template, apertures are naturally formed in the deposited metal film and the aperture size is gradually reduced by the lateral growth of metal. Figure 4.1a shows a schematic of the diameter control with template stripping. The lateral growth of metal can be reduced via increasing the directionality of metal evaporation (e.g. lower chamber pressure, longer source-to-sample distance, and

smaller size of the metal source). To reveal the optimum process conditions, significant efforts were spent to evaluate the parameters affecting the hole size such as the sample location in the chamber, chamber pressure, the rotation of wafer holder, the deposition rate, the electron beam power, and the beam raster size. Based on these experiments, it is possible to tune these parameters in the metal evaporation chamber to shrink the nanohole size in a controlled manner and obtain a hole size down to 100 nm. Figure 4.1b shows the scanning electron micrograph (SEM) of a Si template and template-stripped Ag nanoholes. The measured nanohole diameter in the Si template is 142 ± 7 nm. After a 100 nm thick metal deposition, the diameter of the template-stripped nanohole is reduced to 128 ± 11 nm. The diameter is further reduced to 98 ± 8 nm when the film thickness becomes 200 nm. Figure 4.1c and 4.1d show photographs of the Si nanohole template after metal deposition and template-stripped nanohole arrays, respectively.

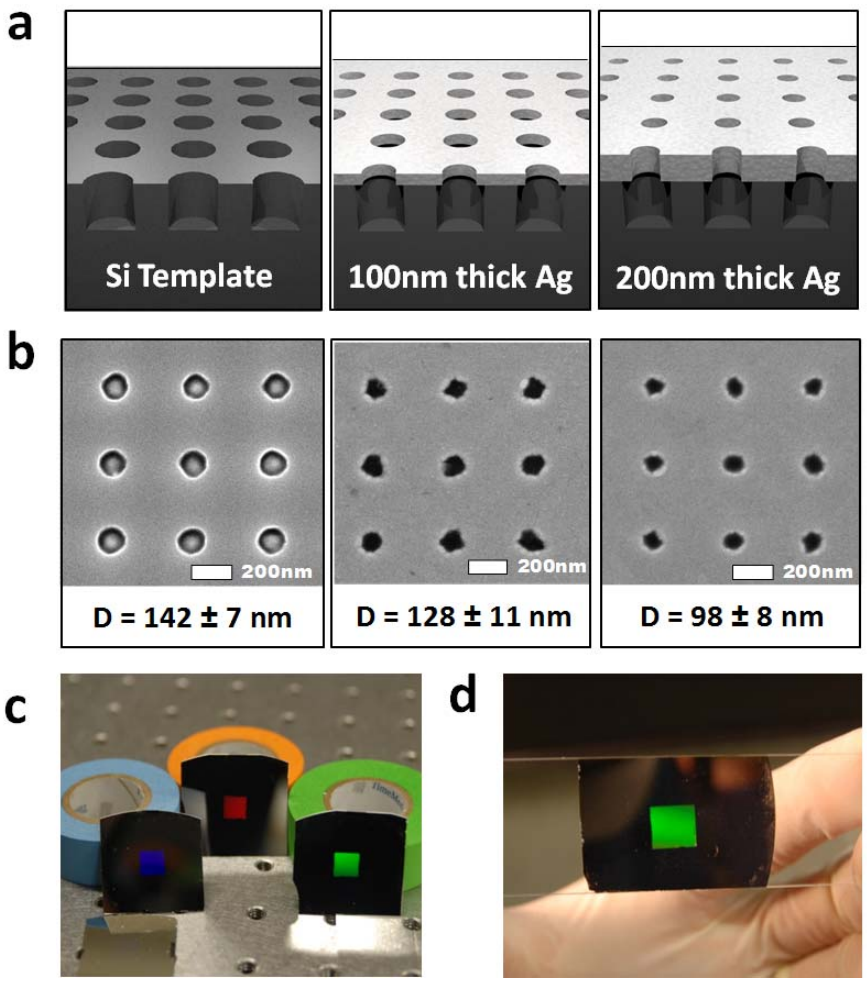

Figure 4.1 The hole diameter control via template stripping. (a) Schematic for fabricating size-tunable nanohole arrays in ultra-smooth metallic films via template stripping. As the metal deposition thickness increases, the metal slowly grows laterally, shrinking the hole size. (b) A top-down scanning electron micrograph (SEM) of the Si template and different thicknesses of template-stripped nanoholes. The measured hole diameter of the mold is 142 ± 7 nm. The hole diameter is reduced to 128 ± 11 nm at a 100 nm thick Ag. The hole diameter is further reduced to 98 ± 8 nm at a 200 nm thick Ag. (c) A photograph of the Si nanohole templates after metal deposition. Si templates have same periodicity. They show very homogenous colors at any angle of incident light. (d) A photograph of an 8 × 8 mm area of periodic Ag nanohole arrays fabricated by template stripping shows extremely uniform optical properties over the entire patterned area. Figure is adapted from Lee *et al*.,[225]

4.3 Effects of hole diameter and surface roughness on the linewidth

4.3.1. Transmission spectra and resonance peak width

To elucidate the major factors affecting SPP damping in a nanohole array structure, computer simulation for the EOT spectra was conducted by changing both the hole diameter from 80 to 200 nm as well as the dielectric functions through 3-D FDTD simulations. FDTD simulations were done using a commercial software package, FullWave (Rsoft Inc.). The simulation area contained a single hole with periodic boundaries within the plane of the metal to simulate an infinite array and perfectly matched layer absorbing boundaries in the planes parallel to the metal film. A nominal grid size of 10 nm was used which was graded down to 3 nm within plane of the metal and down to 5 nm in the z-dimension. The dielectric constants for the metals were numerically fit to a Drude-Lorentz model to be used in the computation. The optical constants for the template-stripped Ag films were measured with a VASE (J.A. Wollam Co.) spectroscopic ellipsometer from 250 nm to 1100 nm from a freshly template-stripped sample and numerically fit to a Lorentz-Drude model that was then integrated into the FDTD simulations. As a comparison, we modeled the same structure using optical constants obtained from Palik,[110] which are commonly used values for Ag. Figure 4.2 shows the imaginary part of dielectric constant of both materials. Notably, the optical loss is reduced significantly in the template-stripped Ag film, as previously shown.[82,111]

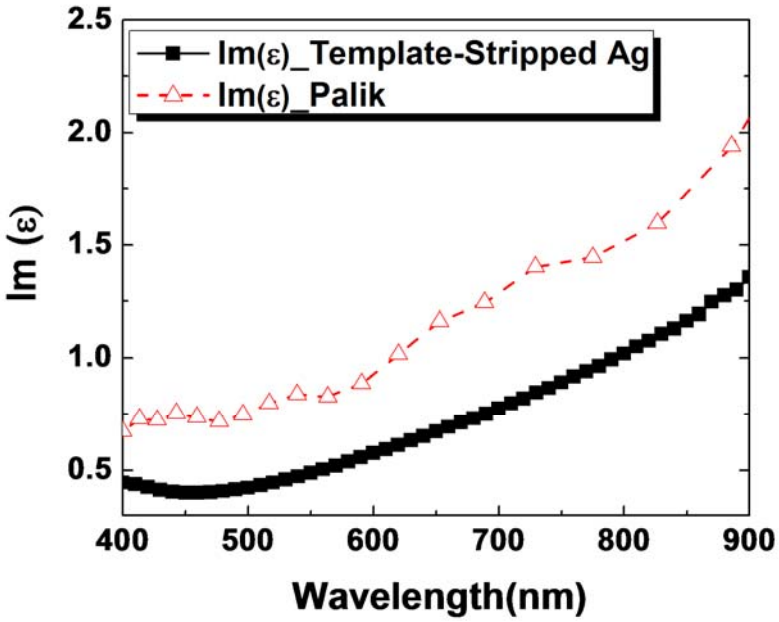

Figure 4.2 The imaginary part of the dielectric function used in the 3-D FDTD simulation before being fit to a Lorentz-Drude model. The dielectric function of the template-stripped Ag film was measured via ellipsometer. Figure is adapted from Lee *et al.*,[225]

When the hole diameter is large, the transmission spectra show similar behavior with the two different dielectric functions (d = 200 nm in Figure 4.3). This implies that at this diameter range, the transmission peaks are broadened primarily through radiative damping as opposed to material damping. The roughness of the surface becomes important when the diameter approaches ~150 nm. Asymmetric Fano-type peaks become noticeable in the EOT spectra modeled using template-stripped Ag optical constants whereas the spectra modeled using Palik's optical constants show a Lorentzian profile (d = 150 nm in Figure 4.3). The spectral positions of the transmission peak maxima at the different grating orders can be approximated with the equation (2.41). Compared to the (1,0) resonances, the (1,1) resonances, which have a higher diffraction order and occur at

shorter wavelengths, show broader spectral widths. As the hole size is decreased further (d = 100 nm in Figure 4.3), an ultra-sharp (1,0) resonance peak is observed, which is associated with SPPs at the Ag-water interface. Overall, reducing the hole size shifts the peak transmission wavelengths toward shorter wavelengths (blue shift) as previously shown,[103,108,112] and changes the line shape to an asymmetric Fano profile. The position of the transmission minima remain unchanged because they are mainly associated with SPP grating coupling with the periodic array.[113]

The relationship between the spectral linewidth and the nanohole diameter is shown in Figure 4.4. The linewidth is determined by measuring the full width at half maximum (FWHM) of the (1,0) peak at the Ag-water interface. With a nanohole diameter of 200 nm, the linewidths from the two different dielectric constants are similar. When the diameter decreases, internal damping—in this case due to excess roughness of the metal surface—starts to emerge as a primary loss mechanism. Upon further reduction of the diameter below ~120 nm, both linewidths start converging to minimum values but show a considerable difference (FWHM = 3.8 and 9.0 nm from using our experimentally measured template-stripped Ag optical constants and those obtained from Palik,[110] respectively).

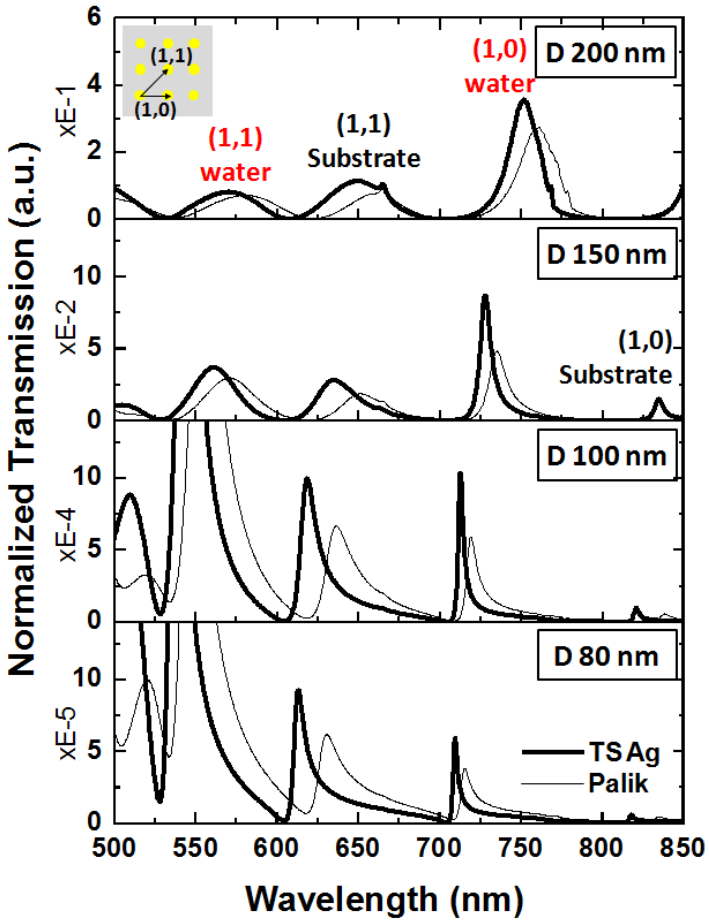

Figure 4.3 3-D FDTD transmission spectra of a nanohole array with varying hole diameter and optical constants. Hole diameters (D) are changed from 80 to 200 nm while the periodicity and Ag thickness are maintained at 500 and 200 nm, respectively. The transmission spectra based on the measured optical constants of template-stripped Ag are denoted by the thick solid lines and the transmission spectra based on optical constants from Palik are denoted by the thin solid lines. All simulations are performed in a water environment (refractive index value 1.33) with the Ag film attached to an optical epoxy substrate (refractive index value 1.56). Figure is adapted from Lee *et al*.,[225]

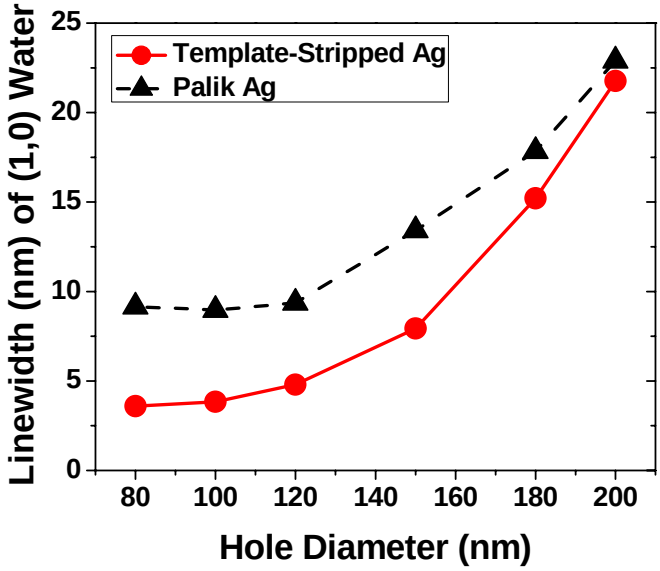

Figure 4.4 Spectral linewidth at the (1,0) resonance versus the hole diameter. The linewidth is FWHM determined from the FDTD spectra. Figure is adapted from Lee *et al.*,[225]

4.3.2. Field enhancement due to the smoothness of metal surfaces

To further investigate the difference the dielectric functions make, FDTD simulations were done showing the full-field intensity distributions at the various resonances. Figure 4.5a and 4.5b show the calculated field intensity for the nanohole arrays using optical constants measured from template-stripped Ag films vs. Palik's constants at the (1,0) resonance (713.3 and 719 nm), respectively. The period of 500 nm, Ag thickness of 200 nm, and hole diameter of 100 nm are maintained the same. The field intensity is much stronger for the case of the measured, template-stripped optical constants (Figure 4.5a) and the enhancement of the smooth, template-stripped Ag nanohole arrays is clearly seen

in Figure 4.5c. The field intensity is enhanced about 2× on the transmission side of the nanohole array which corresponds to the ~2× increase in transmission of that peak shown (d = 100 nm in Figure 4.3). On the incident light side of the nanohole array there is up to a 4× enhancement in the field intensity, which indicates a longer plasmon lifetime in the template-stripped Ag film.

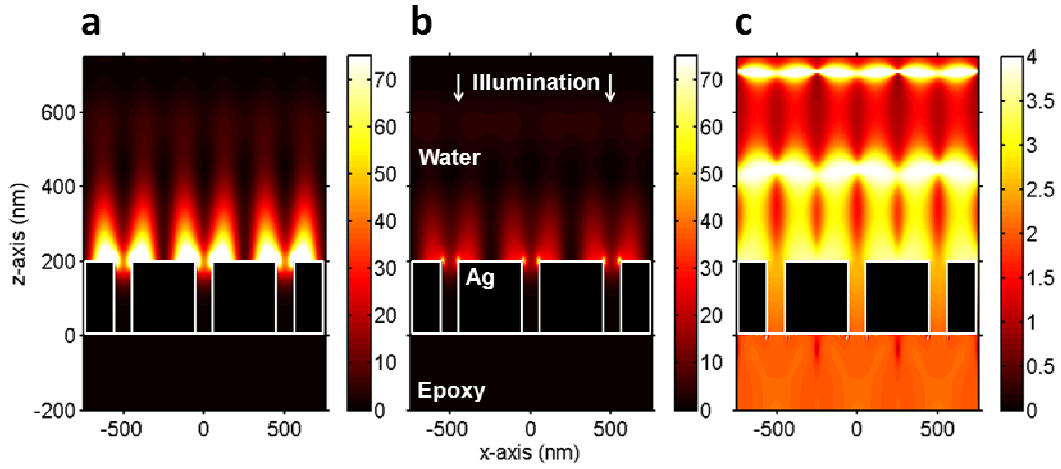

Figure 4.5 FDTD simulations of the full-field intensity distributions. The peak of the (1,0) water resonance for nanohole arrays with period, Ag thickness, and hole diameter of 500 nm, 200 nm, and 100 nm is monitored, using dielectric functions from (a) the template-stripped Ag and (b) Palik. The significant increase in field intensity is further emphasized in (c) which shows the field enhancement between (a) and (b) (panel (a) divided by panel (b)) and indicates both increased transmission and a longer plasmon lifetime. The FDTD image is courtesy of Tim Johnson in our group. Figure is adapted from Lee *et al.*,[225]

4.3.3. Linewidth-optimized EOT via template-stripped nanohole arrays

After tuning the optical film thickness, substrate index, and array periodicity such that the peaks associated with the rough and smooth sides are clearly separated in water, optical transmission spectra were measured from a 200 nm-thick template-stripped Ag nanohole array having a 100 nm hole diameter and a 500 nm periodicity. The measurement was performed after applying a drop of water on the nanohole array and covering it with a glass cover slip. A tungsten-halogen light source illuminated the top surface of the nanohole array through a microscope objective (4×, NA=0.13) and the directly transmitted light was collected by a fiber-optic spectrometer (Ocean Optics, USB-4000). A 3-D FDTD simulation with the same geometric parameters is compared to the measured data in Figure 4.6a. The λ_{max} of the (1,0) and (1,1) SP resonances on the water-side of the film, where the surface is the smooth, template-stripped Ag (Figure 4.6b) show close agreement between experiment and the simulation. However, the peak positions of the substrate (epoxy) side resonances deviate more from the simulations and show broader linewidths, i.e. increased SPP losses, which is likely due to the nominal roughness of the "topside" of the Ag film (Figure 4.6c). When the hole diameter and metal surface are optimized, very sharp SPP resonance peaks in template-stripped periodic Ag nanohole arrays are observed experimentally. The FWHM of the (1,0) SP resonance in water is measured to be 9.9 nm, and the simulated value is 3.8 nm. The discrepancy is likely due to the finite NA (0.13) of the objective used for illumination and the residual roughness on the nanohole sidewalls. The improvement in plasmon lifetime in nanohole arrays can also be characterized using the measured linewidth relative to the

resonance wavelength (the Q factor). According to this definition, the Q factor measured from the (1,0) peak in water is 71, which is among the best values reported in water for visible wavelengths, and indicates a longer SPP lifetime or propagation length on template-stripped Ag surfaces. While it was previously shown that angled illumination of nanohole arrays can sharpen the transmission or reflection peaks,[114-116] the fact that we observe a high Q factor at simple normal incidence further reflects a long SPP propagation length from the small hole size and improved dielectric functions of the metal film.

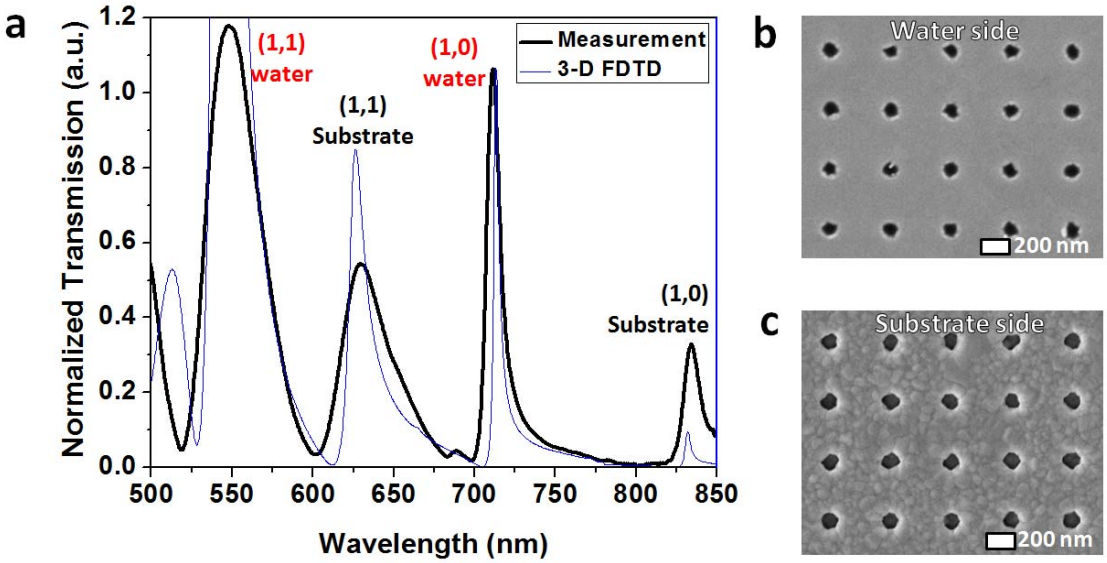

Figure 4.6 Linewidth-optimized EOT via template stripping. (a) Optical transmission spectra of template-stripped nanohole arrays with a 100 nm hole diameter and 500 nm periodicity in a 200 nm-thick Ag film obtained experimentally (thick solid line) and from 3-D FDTD simulation (thin solid line). The spectral linewidths of the (1,0) plasmon peak in water are 9.9 nm and 3.8 nm and Q-factors of this major peak are 71 and 189 in the measured data and the FDTD simulation, respectively. (b) A SEM of a water-side nanohole array which is the smooth, template-stripped Ag film. (c) A SEM of a substrate-side nanohole array which is the rough, topside of template-stripped Ag film. Figure is adapted from Lee *et al.*,[225]

4.4 Sensitivity of linewidth-optimized nanohole arrays

4.4.1. Refractive index sensitivity

To characterize the device sensitivity for biosensing applications, the bulk refractive index sensitivity was evaluated using index-calibrated solution. The bulk refractive index sensitivity of the device is measured by injecting solutions with varying values of refractive index over the nanohole arrays using a microfluidic channel. The index-calibrated solution is prepared by varying the amount of glycerol mixed with water and confirmed by a refractometer (Refracto 30PX, Mettler Toledo). Figure 4.7 shows the transmission spectra change as the refractive index solution changes in the 3-D FDTD (Fig. 4.7a) and the experiment (Fig. 4.7b). When the refractive index increases from 1.333 to 1.356, the (1,0) water resonance peak shifts linearly due to the increase of refractive index near sensing surface. However, the position of transmission minima on the Ag-epoxy interface (λ~ 600 nm) remains unchanged throughout the experiments.

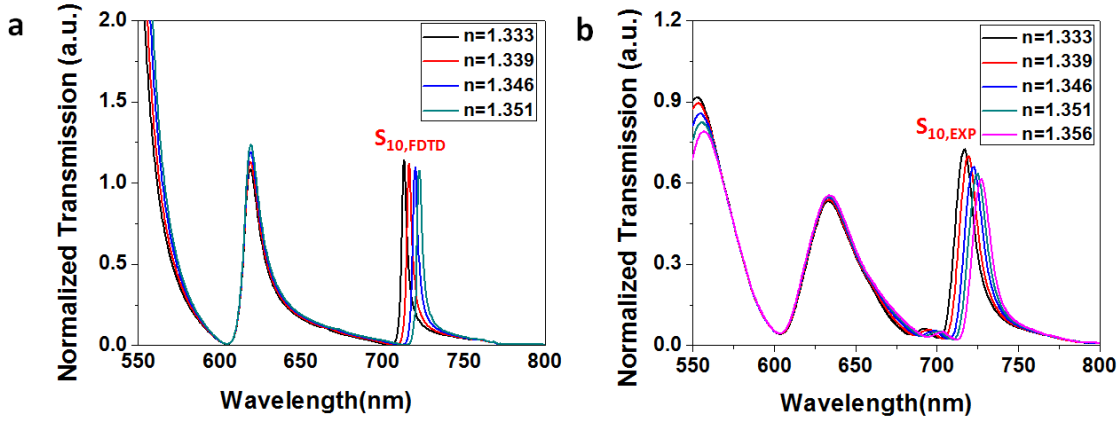

Figure 4.7 Refractive index sensing. The transmission spectra of linewidth-optimized, template-stripped Ag nanohole arrays shifts linearly due to the increase refractive index solution on the sensing surface. (a) 3-D FDTD simulation results are compared with (b) measured optical transmission spectra. Figure is adapted from Lee *et al*.,[225]

The bulk refractive index sensitivity, evaluated from the shift of peak wavelength over the change of refractive index unit (RIU), is presented in Figure 4.8. The measured (1,0) bulk sensitivity is 494 nm/RIU, which is slightly lower than the theoretical values based on FDTD simulations (524 nm/RIU). Experimentally, figure of merits (FOM), representing the performance of the device is as high as 50 (495 nm/RIU divided by 9.9 nm), which is among the best values reported in the visible regime and in water.

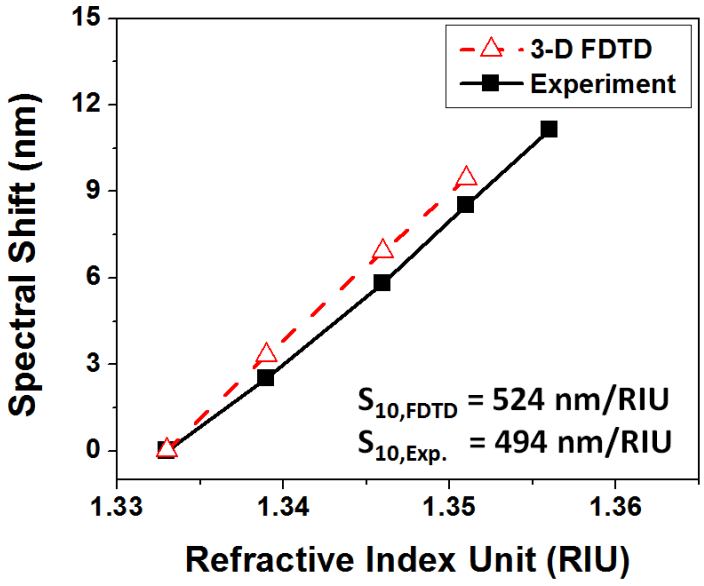

Figure 4.8 Refractive index sensitivity of linewidth-optimized nanohole arrays. The spectral shifts are measured by changing the refractive index of water-glycerol mixture from 1.333 to 1.356. The sensitivities of the (1,0) water SP resonance (S_{10}) are measured from the spectral shifts of the maximum peak position. Figure is adapted from Lee *et al.*,[225]

4.4.2. Surface sensitivity measurement via ALD process

While the bulk index sensitivity is straightforward to measure and provides a means to compare the performance of various optical biosensors, the ultimate performance of these sensors is determined by the signal changes resulting from thin-film adsorption, i.e. localized surface sensitivity, since molecular binding events occur within tens of nanometers from the sensing surface. To quantify this local detection sensitivity, ALD of Al_2O_3 has been used for layer-by-layer characterization of the spectral shifts. Previously, such layer-by-layer ALD characterization has been performed in air,[85,86] but the plasmon decay length and local sensitivity will change when the sensor is immersed in water. Figure 4.9a shows a schematic of the local sensitivity measurement of template-stripped Ag nanohole arrays by an ALD process. The spectral shifts of the (1,0) peak are monitored with increasing ALD thickness from 0 to 35 nm in 5 nm intervals. To prevent surface oxidation of Ag, an initial 2 nm of Al_2O_3 layer is formed prior to the first measurement in water. The aqueous condition is maintained during the measurement by using a cover slide after applying a drop of water on the nanohole array. Afterwards, the sample is completely dried with a high purity N_2 before immediately proceeding to the next ALD step. The ALD process is monitored after each interval by ellipsometric measurements on the thickness of the Al_2O_3 deposited on a Si chip processed in the same chamber. While this characterization method is very time-consuming and requires careful sample handling to avoid contamination and artifacts, the results obtained are more representative of what one would expect from biosensing in an aqueous environment. FDTD simulations were also carried out adding conformal layers with an index of 1.65 to

the surface and in the holes. The local sensitivity of the (1,0) SP resonance peak of Ag nanohole arrays is 1.13 nm shift per 1 nm Al_2O_3, which shows good agreement with the FDTD result (1.32 nm shift per 1 nm Al_2O_3 in Figure 4.9b). In addition, the spectral shift increases linearly within the ALD thickness range used. Since the ALD process is highly reproducible, this surface sensitivity data obtained in water can help evaluate the local sensitivity of various SPR and LSPR biosensors in practical biosensing environments.

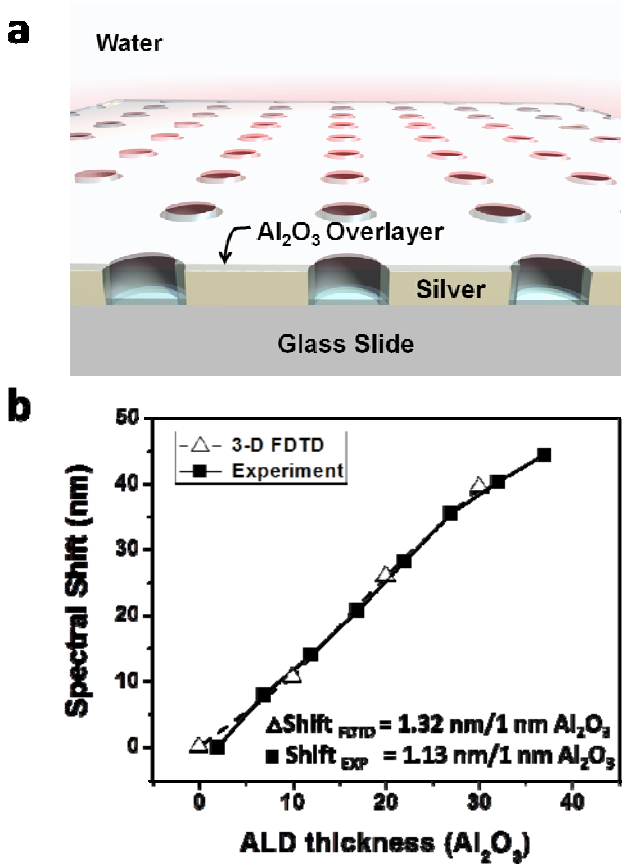

Figure 4.9 Surface sensitivity characterization using ALD. (a) A schematic for a local sensitivity measurement of template-stripped nanohole arrays by an Al_2O_3 atomic layer deposition (ALD) process. (b) The spectra shifts of (1,0) water SP resonance peaks are measured by increasing ALD thickness. The result of FDTD (triangle, dashed line) matches very well with that of experiment (square, solid line). Figure is adapted from Lee *et al.*,[225]

4.5. Conclusion

In this chapter, the effects of hole diameter and surface smoothness on the linewidth of EOT peaks were investigated with an emphasis on minimizing radiation and material damping of plasmons. Besides being a massively parallel method to create high-quality metallic nanostructures, the template-stripping process also provides tunability for the nanohole diameter. When the nanohole size is above ~200 nm, the linewidth at visible frequencies is predominantly determined by the radiative scattering of SPPs by the large nanoholes. Below ~150 nm nanohole size, materials loss dominates the linewidth, and smooth Ag films will further sharpen the EOT peaks in that regime. The measured linewidth from nanoholes immersed in water is less than 10 nm. Furthermore, the measured Q-factor of the EOT peak in template-stripped nanohole arrays is as high as 71 at visible frequencies in aqueous conditions. Bulk and local sensitivity of this template-stripped device are in good agreement with the theoretical results (FDTD). Since this sharp peak (9.9 nm linewidth) can be obtained from the cm-sized nanohole array with simple normal incidence illumination via an incoherent light source, it will benefit broad applications based on EOT such as surface plasmon resonance imaging[106,117-121] and spectroscopy.[35,122-125]

CHAPTER 5

SPR SPECTRAL IMAGING FOR HIGH-THROUGHPUT AFFINITY MEASUREMENTS

Precise measurements of binding kinetics and affinity of receptor-ligand interactions play an important role in pharmaceutical development as well as basic biology. Although the commercially available BIAcore™ system has been the gold standard for label-free and real-time biosensing, it is not capable of high-throughput kinetic measurements that are required for large-scale proteomics studies. Surface plasmon resonance (SPR) imaging technology does have the potential for such high-throughput measurements. However, intensity-based 2-D SPR imaging is not widely used in pharmaceutical field due to the difficulty of protein spotting with small volume and the artifacts such as cross-contamination, position dependent depletion of analyte, as well as position dependent binding rates due to mass transport effects. To address these drawbacks, SPR spectral imaging combined with multichannel microfluidics is investigated in this chapter. The work presented here is mainly derived mainly from the following publication:[226]

1. **S.H. Lee**, *N. C. Lindquist*, *N. J. Wittenberg*, *L. R. Jordan, and S.-H. Oh*, *Submitted.*

5.1 Motivations of SPR spectral imaging

The ability to quantify kinetics and affinities of receptor-ligand binding interactions is essential for basic biology, biomarker discovery, proteomics, and pharmaceutical development, among others.[126] Owing to the success of the DNA microarray, the protein microarray has attracted increasing attentions as a solution to these needs.[127-134] Conventional protein microarray technologies use fluorescent or radioactive labels to target molecules to verify the binding. This labeling process, however, can potentially alter or interfere with specific molecular binding sites. In addition, this dye molecule only gives on/off information, requiring multiple concentration assays to extract the kinetic constants of a given binding partner. Furthermore, for a high-affinity interaction, it is impractical to use this equilibrium assay because of the tremendous time to reach to an equilibrium state. Therefore, this difficulty has brought a great demand for a real-time, label-free biosensor that can directly measure binding kinetics with unaltered molecules.

Among this class of biosensors, optical biosensors that utilize surface plasmon waves[135] (SPs) – surface electromagnetic waves propagating at the interface between a metallic film and a dielectric medium – have been widely used for this purpose.[136-139] Commonly known as surface plasmon resonance (SPR) instruments, they measure refractive index changes near the metal surface caused by surface binding of biomolecules without fluorescent labels, enabling rapid label-free quantification of association/dissociation rates and equilibrium constants for analytes binding to targets such as proteins, antibodies, nucleic acids, aptamers, or lipids. Owing to rapid developments in proteomics, lipidomics, and systems biology, there is a growing demand

to enhance the throughput and sensitivity of conventional SPR instruments. [126] Many technological challenges exist, however, since even routine quantification of protein binding kinetics generally requires a series of SPR measurements performed at multiple analyte concentrations, which can take hours depending on surface modification steps and dissociation rates. SPR imaging provides an attractive path to expand the throughput of conventional SPR sensors.[140-146] Typically an analyte or buffer solution flows over a microarray of receptors on the gold sensing surface, which is illuminated with a light source. The spatial variation in light intensity generated by surface binding is imaged in real time, allowing the extraction of binding kinetics from every spot simultaneously. Target receptors are typically arrayed on the gold sensing surface using robotic spotting tools, microfluidics, or microcontact priting. Among various multiplexing options, intensity-based SPR imaging of two-dimensional (2-D) microarray has been widely studied,[143] because many sample spots can be densely packed in this format. High-throughput SPR imaging with a 2-D microarray of proteins, however, is a challenging task, because standard robotic spotting protocols, which work well for nucleic acids, do not translate well to spotting protein microarrays.[126] It is difficult to print small protein spots with a uniform thickness and morphology, and the protein spots must be prevented from drying, which can denature some proteins.[147] Also, in a typical SPR imaging experiment with a 2-D microarray, wherein multiple receptor spots are exposed to an analyte solution in a single flow cell, artifacts or errors may be introduced due to cross-contamination, position-dependent depletion of analyte, as well as position-dependent binding rates due to mass transport effects.[148]

Alternatively, SPR imaging can be performed with parallel microfluidic channels that partition the sensing area on the gold surface. While the multiplexing capacity in space is reduced in this one-dimensional (1-D) array, multiple receptors can be patterned on the gold surface via well-established flow-based immobilization protocol, obviating the needs for expensive robotic spotting tools. In fact, many commercial SPR instruments use individual flow cells such that all experimental steps such as receptor immobilization, washing, blocking non-specific binding, protein binding, and surface regeneration are performed in the same channel using flow-based techniques, rather than spotting.[149] Furthermore, because the flow cell is partitioned into multiple isolated channels, cross-contamination can be eliminated and receptors that are not amenable to standard robotic spotting (e.g. lipid membranes) can be readily reconstituted and confined inside each microfluidic channel. In short, 1-D configuration can eliminate the cross-talk between each spot and eliminate unnecessary steps and expensive spotting tools, leading to process automation. By using photolithography, the width of each microfluidic channel can be reduced smaller than the capability of molecular spotting equipment, giving a highly parallel arrangement. Unlike single-channel SPR sensing, wherein a full angular or spectral response of a sensor chip can be recorded in real time, intensity-based 2-D SPR imaging can only records the intensity of light at a fixed wavelength, rather than full spectral information.

The drawbacks mentioned above motivates the development of a high-throughput SPR imaging instrument capable of measuring full spectra in real time from a large array of parallel microfluidic channels. After coating the template-stripped large-area Ag

nanohole arrays films with a thin silica shell for biological interfacing, a PDMS microfluidic chip is bonded to form to partition the sensing region into 50 parallel microfluidic channels. After demonstrating real-time SPR spectral imaging with custom LabVIEW^{TM} software and MATLAB-based image processing, device sensitivity and refractive index resolution are evaluated. The use of partitioned microfluidic channels allows us to readily incorporate membrane-bound receptors in fluidic supported lipid membranes[101] without cross-contamination or mixing. To demonstrate the utility of our instrument for high-throughput analysis of protein-lipid interactions, SPR spectral imaging is performed using cholera toxin b and ganglioside (GM1), and the dissociation rate constant (k_d), association rate constant (k_a), and equilibrium dissociation constant (K_D) are extracted simultaneously from 50 channels.

5.2 Imaging spectroscopy setup

Figure 5.1a describes the concept of SPR spectral imaging using metallic nanohole arrays. Broadband light illuminates nanohole arrays at normal incidence. Surface plasmon polaritons (SPPs) are excited, and resonantly transfer energy through the nanohole substrate, then light is re-radiated back to free space. This transmitted light exits the microscope (Nikon Eclipse Inverted) via the side camera port and enters the imaging spectrometer through a narrow slit. The multiple channels are imaged and aligned along the vertical entrance slit and are each dispersed as a single spectrum by a grating. These spectra are then recorded on a 1340 × 400 pixel CCD in real time. In this way, the recorded image contains spectrally dispersed information (i.e. optical transmission

spectrum through nanoholes) along the spectral axis, and spatially resolved 1-D image of multiple channels along the orthogonal (image axis) direction. The range and resolution of the spectra dispersed horizontally also can be controlled by using diffraction gratings with different line-spacing. Figure 5.1b shows a sample spectral image taken from the imaging spectrometer (Newport MS257) with a low-noise, deep-cooled CCD camera (Princeton PIXIS) controlled by custom LabVIEW^{TM} software. Because EOT can be excited by the periodic nanohole arrays at certain resonance wavelengths, the image recorded on CCD shows different transmission intensity peaks along the spectral (horizontal) axis. Channels and boundaries can be clearly distinguished along orthogonal (image axis) due to the difference of refractive index between polydimethylsiloxane (PDMS) and liquid solutions. After taking a spectral image, the data is analyzed using MATLAB image-processing scripts to extract the spectra and quantify kinetics data from each microfluidic channel in parallel (Fig. 5.1c). Unlike conventional SPR imaging which measures intensity changes, full spectral information from each and every channel can be acquired without any data loss, leading to the increase of dynamic range of detection. For example, SPR imaging using a laser (i.e. single-wavelength) illumination requires the excitation wavelength precisely positioned at the position of maximum sensitivity along the SPR curve (i.e. region of maximum slope).[150] However, this sets a limitation since further molecular immobilization can shift the SPR response curve. With full spectral imaging, such restrictions do not exist, since the entire spectrum can be recorded. Furthermore, by combining a surface-enhanced Raman spectroscopy (SERS) capability

of nanohole arrays[35] with the imaging spectroscopy, it is possible to use our instrument to perform a molecular detection and identification successively in a parallel setup.

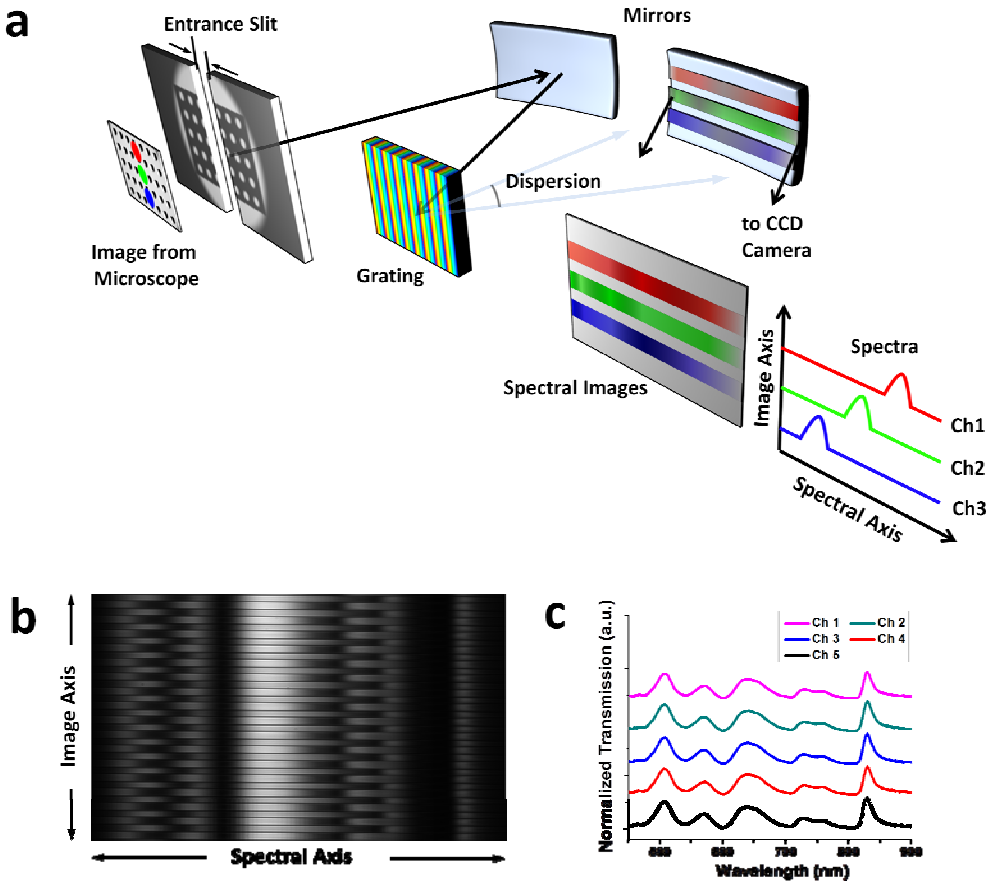

Figure 5.1 Schematic of the imaging spectrometer setup. (a) An image from the microscope enters a spectrometer through an entrance slit and is spectrally dispersed by a grating and mirrors. Then, the spectral image is recorded on a CCD in real-time. From the spectral image, the spectra from different positions along image axis can be extracted by image-processing MATLAB scripts. (b) The one-dimensional (1-D) spectral image obtained from the multichannel microfludics assembled on periodic nanohole arrays. Different intensities along spectral axis represent the enhanced transmission due to surface plasmon polaritions (SPPs) excited by light illuminating the periodic nanohole arrays. The channels can be clearly distinguished from the boundaries due to the difference of refractive index of PDMS and water. (c) The intensities in the same channel are averaged and transformed to spectra using image-processing MATLAB scripts. Figure is adapted from Lee *et al.*,[226]

5.3 Nanofabrication and microfluidic integration

The fabrication of large-area nanohole arrays having homogenous optical properties is the prerequisite to perform the high-throughput SPR imaging spectroscopy. Figure 5.2a shows photographs of Si templates and template-stripped nanoholes. The Ag film is stripped off from this Si template after curing UV optical epoxy, producing a large area (8 × 8 mm) periodic nanohole array. By preparing multiple Si templates, It is possible to obtain multiple high-quality nanohole arrays from one metal deposition without any additional etching processes. The master templates can be reused after removing residual metals.

The nanohole array substrate is attached to a PDMS microfluidic chip, which partitions the nanohole array into 50 individual channels. Figure 5.2b shows a photograph of 50-channel microfluidics assembled on the nanohole array. The channel period is 70 μm and the width of each channel is 30 μm. Five channels merge to one inlet and outlet, producing an equivalent width of 150 μm. All 50 channels can be monitored simultaneously in our instrument. While the number of channels could be increased beyond 100, attachment of inlet and outlet tubes and syringe pumps limits the practical throughput in the proof-of-concept experiment. Before assembling multichannel microfluidics on the Ag nanohole arrays, silica is coated on the surface by atomic layer deposition (ALD). This dense and conformal silica layer will protect Ag from oxidation as well as promote supported lipid bilayer formation.[84] In addition, the PDMS chip containing microfluidic channels can be permanently bonded to silica-coated nanohole arrays, which eliminates fluid leakage. (Fig. 5.2b) Inset in Figure 5.2b shows the SEM of

template-stripped Ag periodic nanohole arrays having 500 nm periodicity. Figure 5.2c shows a spectral image of 50-channels after injecting water into all channels. All the channels and boundaries are clearly distinguished in the image.

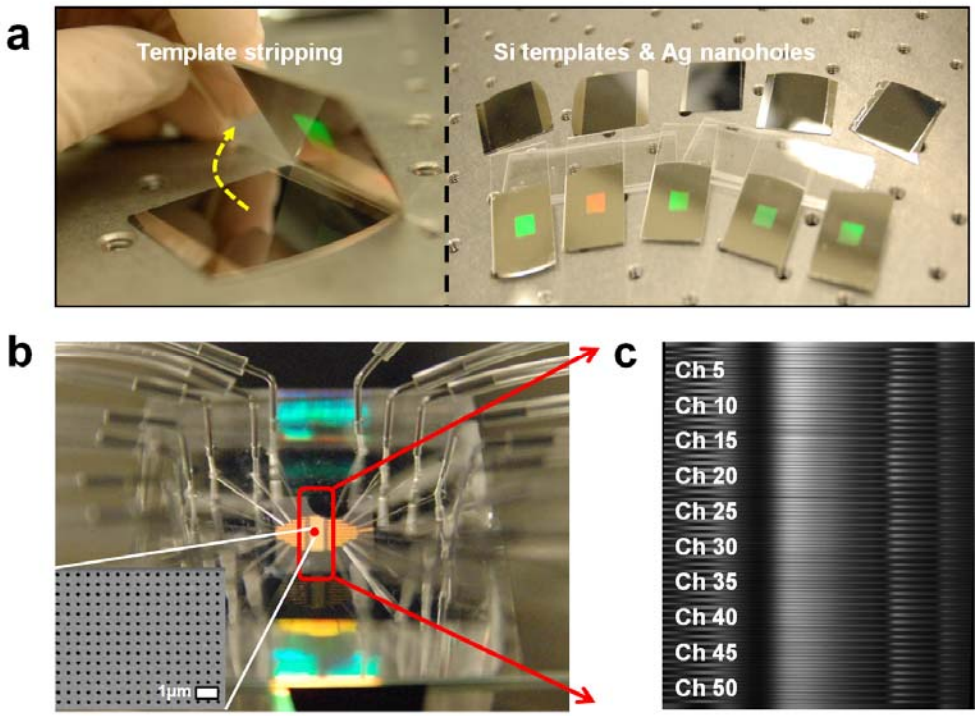

Figure 5.2 Template-stripped nanohole arrays for the 50-channel microfluidics and the spectral image. (a) Photographs of template-stripped nanohole arrays and Si templates. The 8 × 8 mm area of a periodic Ag nanohole array is transferred onto a glass slide from a Si template after curing UV optical epoxy and peeling it off by a razor blade (left). Multiple template-stripped nanohole arrays are obtained from one metal deposition without any additional etching process (right). (b) A photograph of a 50-channel PDMS microfluidic chip, which is permanently bonded onto a silica-coated Ag nanohole array substrate to eliminate the fluid leakage during experiments. (inset) Scanning electron micrograph (SEM) of template-stripped Ag periodic nanohole arrays. (c) A spectral image of 50-channels after injecting water into all channels. Figure is adapted from Lee *et al*.,[226]

5.4 1-Dimensional full-spectral SPR imaging

5.4.1 Uniformity of optical properties

Prior to multichannel biosensing, the uniformity of the optical spectra from each channel was evaluated. After the spectral dispersion, 50 channels over a 3.5 × 2 mm area were successfully recorded on the CCD (Fig. 5.2c). Multiple points of enhanced transmission (i.e. bright spots) in each channel in the image represent the EOT resonances from the various grating orders and different interfaces between sensing surface and surrounding medium (i.e. water or substrate). This transmission peak maxima of EOT can be predicted by the following grating coupling equation.

Figure 5.3a shows the spectra extracted simultaneously from all 50-channels. Positions 1, 2, and 3 represent transmission maxima at (1,1) water, (1,1) substrate, (1,0) water, respectively. While the transmission varies somewhat from channel to channel, highly consistent spectral peak positions over the 50 channels are acquired due to the high-quality template-stripped nanohole arrays. The resolution of one pixel in the spectral image can be tuned by changing the grating used in the experiment from 0.623 nm/pixel with a 121 lines/mm grating to 0.0623 nm/pixel with a 1200 lines/mm grating. Based on the gratings used, the spectral range can cover a 250 nm window, which can accommodate major EOT resonances, or a 25 nm window for monitoring the peaks in a narrow spectral region. Figure 5.3b shows the average and standard deviation (SD) of the peak position at each resonance. The SD of the (1,1) substrate resonance peak is less than 1 nm and the (1,1) and (1,0) water resonance peaks have SDs of 1.1 nm and 1.6 nm, respectively, proving highly homogeneous

optical properties across devices and positions (~ 1 cm), which provide a great benefit to SPR spectral imaging experiments.

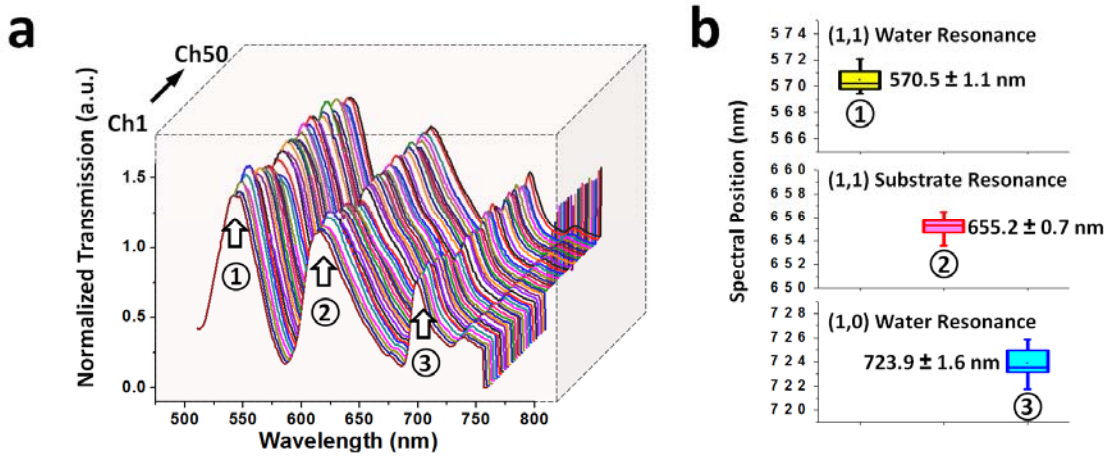

Figure 5.3 50-channel spectra extracted from the spectral image. (a) The spectra extracted from 50-channels by averaging the intensities between two positions inside each microfludic channels along the spectral axis. Positions 1, 2 and 3 represent transmission maxima at (1,1) water, (1,1) substrate, (1,0) water, respectively. The positions of these resonance maxima are highly consistent over all channels. (b) The average and standard deviation (SD) of spectral maxima at each resonance position. Standard deviation (SD) of resonance maxima positions show very homogeneous values over all channels, 1.1 nm, 0.7 nm, 1.6 nm at (1,1) water, (1,1) substrate, and (1,0) water resonance, respectively. Figure is adapted from Lee *et al.*,[226]

5.4.2 Device sensitivity over 50 channels

To evaluate the sensitivity of nanohole device, refractive index sensing is performed. Glycerol-water solutions with different refractive indices are serially injected into all channels. When the refractive index increases from 1.333 to 1.353 in steps of 0.05

refractive index units (RIU), the spectrum shifts linearly due to the increase of refractive index near sensing surface (Fig. 5.4a). The spectral shift is consistent over all 50 channels, and the measured (1,0) bulk sensitivity of the device is 470 ± 11.7 nm / RIU.(Fig. 5.4b)

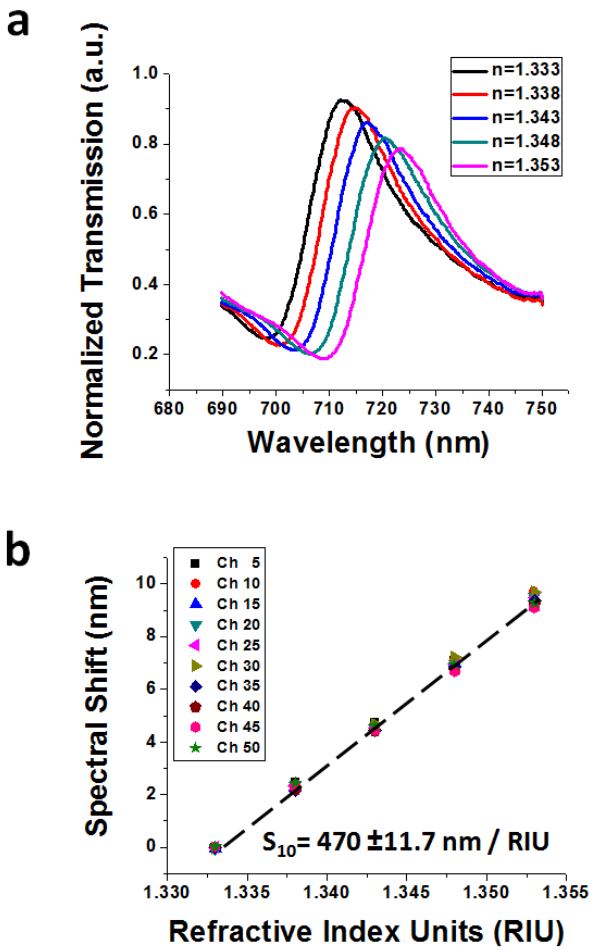

Figure 5.4 Refractive index sensitivity of a 50-channel SPR nanohole arrays. (a) The transmission spectrum shifts after injecting the index-calibrated water-glycerol solutions. Each spectrum is obtained from one of the 50 channels using a 600 lines/mm grating. (b) The refractive index sensitivity measured from spectral shift versus refractive index units (RIU) change. It shows linear increase and is consistent over all 50 channels. The measured sensitivity is 470 ± 11.7 nm / RIU. Figure is adapted from Lee *et al.*,[226]

5.4.3 Refractive index resolution of the multichannel device

Spectral and temporal resolutions are also important factors for defining the performance of the system. Spectral resolution (i.e. refractive index resolution) is obtained by dividing the noise level (σ) by the refractive index sensitivity. Therefore, noise suppression is important to increase refractive index resolution after optimizing the sensitivity of the device. Among various source of noise, shot noise—statistical variation of photon flux on CCD—is the major background noise in real-time SPR measurements. It is reported that this random variation can be reduced by doing multiple temporal averaging of the spectra (i.e. multiple frame averaging).[151,152] For a continuous exposure mode CCD, however, it is required to have enough frame exposure time to remove all previous data during the readout (R/O) time. Otherwise, charge will continue to accumulate, blurring the image along one direction (i.e. a smearing effect). This can be circumvented by blocking the photon flux on the CCD during R/O time using a shutter. However, the R/O time of full-frame imaging is considerably longer (~ 250 msec) than that of line spectra, it is not effective to reduce the exposure time dramatically which enables the multiple frame-averaging. To allow enough refreshing time for a full-frame imaging and avoid the optical cross-talk, 1.0 sec exposure time is used in the experiment. Even at no averaging (1.2 sec of temporal resolution), the measured spectral noise (σ) is 5.2×10^{-3} nm due to the deep-cooled, low-noise CCD as well as large-area (~cm^2) nanohole arrays allowing high intensity of transmission light (Figure 5.5a). Figure 5.5b shows the spectral resolution

based on the refractive index sensitivity and the noise (σ) at the 2.5 sec (1 sec exposure with 2 averaging) temporal resolution. The noise is decreased to 3.6×10^{-3} nm by doing 2 times temporal averaging. Based on the sensitivity and the noise level, 7.7×10^{-6} RIU level of spectral resolution is obtained at multichannel nanohole-based SPR spectral imaging without any on-chip cooling. Spectral resolution can be further reduced by using a faster CCD or CMOS camera because it is a shot noise that contributes to the background noise more than the uniformity or dark current in the high photon influx and fast time-frame imaging.[153] However, the majority of antibody and antigen binding kinetics can be studied with this refractive index resolution.

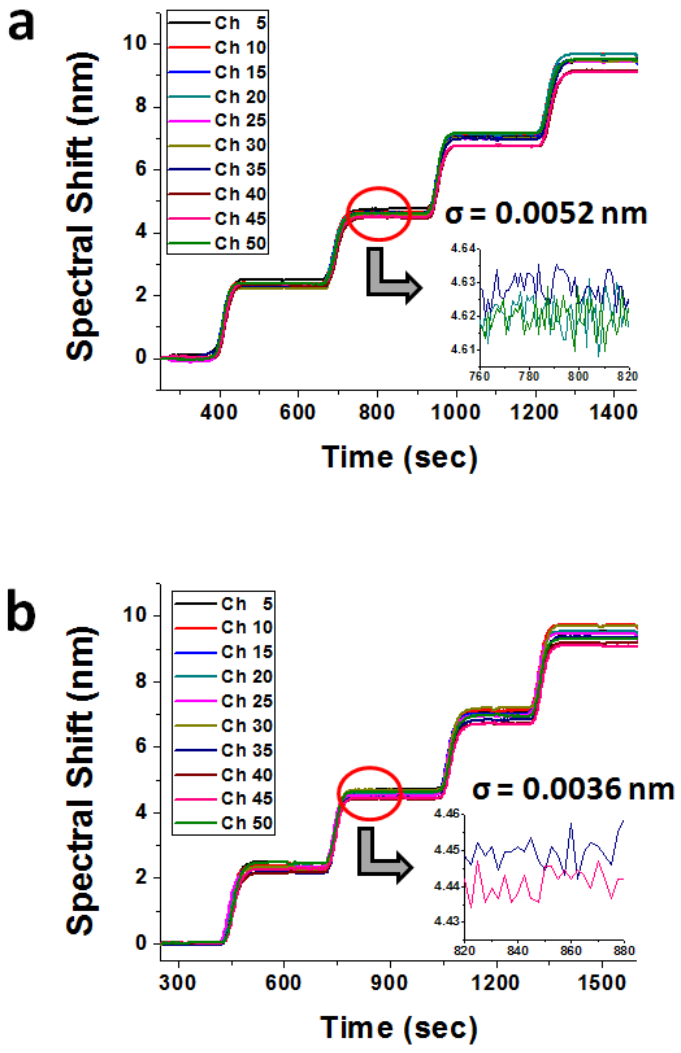

Figure 5.5 Spectral resolution of a 50-channel SPR nanohole arrays. Spectral resolution is based on the refractive index sensitivity and the standard deviation of noise. (a) the measured spectral noise (σ) is 5.2×10^{-3} nm due to the deep-cooled, low-noise CCD as well as large-area (~cm^2) nanohole arrays allowing high intensity of transmission light (b) With 2.5 sec temporal resolution, the spectral noise is σ = 3.6×10^{-3} nm, giving ~ 7.7 $\times10^{-6}$ RIU spectral resolution without any on-chip cooling. Figure is adapted from Lee *et al*.,[226]

5.5 SPR spectral imaging results

5.5.1 Vesicle formation

Vesicles used in the experiments were composed of Egg PC (L-alpha-phosphatidylcholine) (Avanti Polar Lipids, chicken eggs) and varying amounts of Ganglioside GM_1 (ovine brain-ammonium salt) (0 - 4 mol %). For fluorescence imaging 1 mol % Rhodamine-DPPE (1,2-dipalmitoyl-sn-glycero-3-phosphoethanolamine-*N*-(lissamine Rhodamine B sulfonyl), ammonium salt) was incorporated. Lipids in chloroform/methanol were mixed to desired amounts and then dried under vacuum in glass vials for at least 6 hours to remove all solvent. The dried lipid film was then hydrated with NaTrisEDTA buffer (100 mM NaCl, 10 mM Tris, 1 mM EDTA, pH = 8) and refrigerated overnight. Next the lipids were vortex-mixed for 10 seconds to disperse the vesicles into solution, followed by bath sonication for 10 min, and lastly by 15 passes through an extruder with a polycarbonate membrane filter having 200 nm diameter holes (Avanti Mini-Extruder), all performed at room temperature. Prior to injecting the vesicles on the chip, an equal amount of NaTrisCa buffer (100mM NaCl, 10mM Tris, 10mM CaCl2, pH = 8) was mixed with the vesicle solution to promote rupture on the chip surface. Cholera toxin b subunits (CTX-b) from recombinant origin, conjugated with Alexa Fluor-488 dye (5 mol dye/mol pentamer), was purchased from Invitrogen and mixed in PBS.

5.5.2 Surface chemistry with lipid membranes

To demonstrate the multi-channel microfluidic SPR spectral imaging capability, cholera toxin b (CTX-b) and ganglioside GM1 are used. CTX-b binding to GM1 is a well-characterized system of a protein binding to a lipid receptor. [154-159] Figure 5.5a shows schematic of a supported lipid bilayer (SLB) on a nanohole sensor and CTX-b binding to GM1 in the SLB. Phospholipid vesicles containing GM1 are injected into microfluidic channels then rupture on the silica-coated nanohole array to form SLBs.[101,160] After SLB formation CTX-b is introduced and binds with oligosaccharide portion of the GM1 receptor.

Prior to SPR imaging, fluorescence imaging is employed to evaluate SLB formation on the silica surface and CTX-b binding to GM1 in multiple channels. Vesicles containing 1 mol % rhodamine-labeled phosphatidylethanolamine (Rho-PE) but with different concentrations of GM1 were injected into each individual flow cell. After the formation of SLBs, 50nM CTX-b was introduced simultaneously into all channels. Figure 5.5b shows fluorescence images of SLBs with 1 mol % Rho-PE (top) and Alexa 488-conjugated CTX-b (bottom). The Rho-PE intensity is consistent across all channels, indicating little channel-to-channel variability in SLBs formation. However, the Alexa 488 intensities increase when the GM1 densities increase, implying more CTX-b binds when the receptor density increases, as expected. Figure 5.5c shows a line profile of fluorescence intensity across the of microfluidic channels.

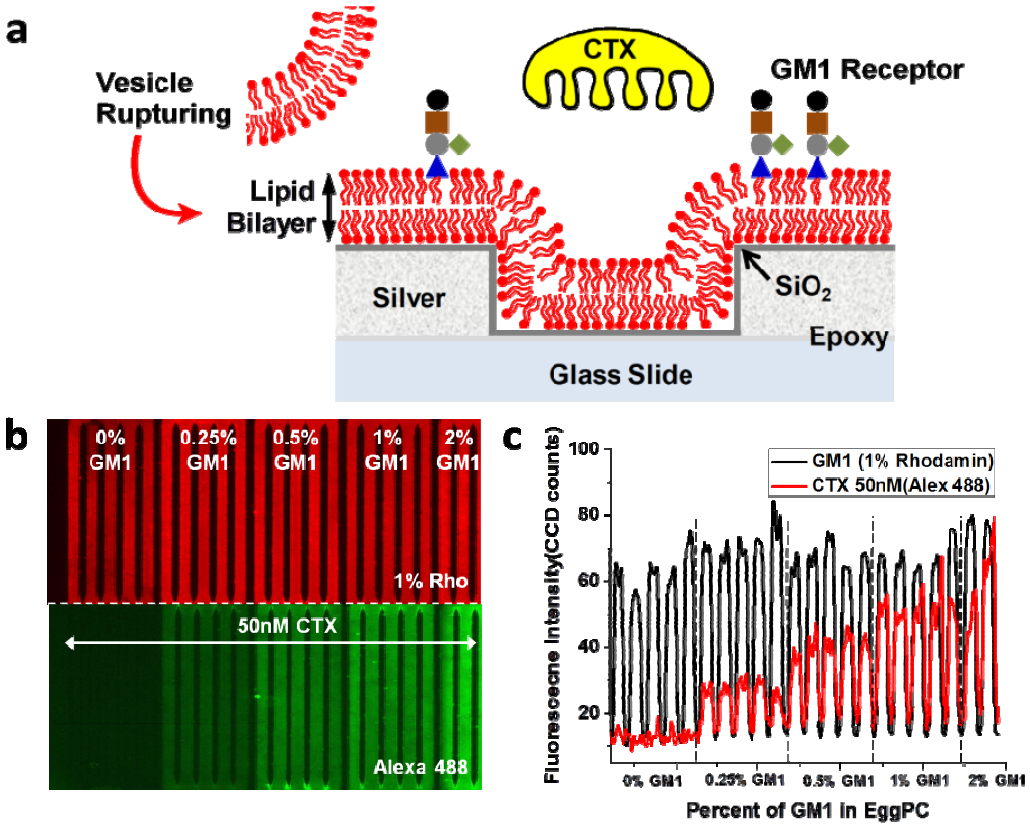

Figure 5.6 Supported lipid bilayer (SLB) formation on a silica-coated nanohole sensor having different concentrations of GM1. CTX-b bindings are confirmed by the fluorescence image. (a) Schematic of cholera toxin b subunits (CTX-b) binding to gangliosidemonosialic (GM1) receptor incorporated in lipid membranes. First, a silica shell is coated on a silver surface to promote vesicle rupture. Then, GM1 containing vesicles are injected into microfluidic channels and rupture to form supported lipid bilayers (SLBs). The CTX-b is introduced and binds with GM1. (b) Fluorescence images showing homogeneous SLBs formation and different amount of CTX-b binding to various concentration of GM1 in supported lipid bilayers. (c) A line profile of fluorescence intensity across the microfluidic channels. The fluorescence intensity of the SLBs indicates a homogeneous lipid membrane across the channels, while the intensity of CTX-b bound to GM1 increases due to the increase in receptor density. Figure is adapted from Lee *et al.*,[226]

5.5.3 Sensorgram and receptor concentration assays

The experimental cycle including SLB formation, blocking and CTX-b binding is shown in Figure 5.7a. First, all channels were wet with a PBS solution for at least 10 min. Lipid membranes were formed by injecting egg PC vesicles containing GM1 molecules into the channels with a constant flow rate of 20 µl/min for 2min and 5 µl/hr for the rest of time. Only egg PC vesicles without GM1 molecules were injected in the channel for a negative control. After incubation of vesicles for 1 hour to allow vesicle rupture on the silica surface, excessive vesicles and lipid overlayers were washed by PBS for another 30 min with a flow rate of 20 µl/min. After injecting PBS to remove excess vesicles, the resonance peak position stabilized at a 2 nm shift from initial (1,0) maximum position, indicating stable formation of an SLB on the nanohole array. To reduce non-specific binding of CTX-b on the lipid membrane, the surface is blocked by injecting a 1 mg/ml BSA solution at 20 µl/min for 5 min and 1 µl/min for 25 min, followed by PBS washing for another 30 min. After 5 min baseline with the PBS solution, different concentrations of CTX-b solution were injected simultaneously for 5 min, followed by PBS washing for another 60 min. All solutions were introduced into channels continuously by using a four-way valve (Cole-Parmer, USA) and two syringe pumps (Harvard Apparatus). The real-time kinetics of CTX-b binding to GM1 receptor were obtained by monitoring the spectral shifts of the maximum transmission peak around 700 nm.

Though CTX-b is pentavalent, a 1:1 kinetic interaction model can be used for low receptor densities, while more complex models are required for higher receptor densities where polyval

ent interactions occur.[161] Therefore, the first set of experiments was to determine the range of GM1 concentrations for which a 1:1 binding model is appropriate. Figure 5.7b shows kinetic curves for 50 nM CTX-b binding on SLBs with GM1 concentrations ranging from 0 – 4 mol %. During a 5 min CTX-b injection, rapid association between CTX-b and GM1 were observed. Up to 2 mol % GM1, the maximum spectral shift is linearly proportional to the amount of GM1 in the SLB. In all kinetic analyses, bulk refractive index change was subtracted. During the 1 hour dissociation phase, all channels showed slow negative peak shifts, confirming the high affinity between CTX-b and GM1.

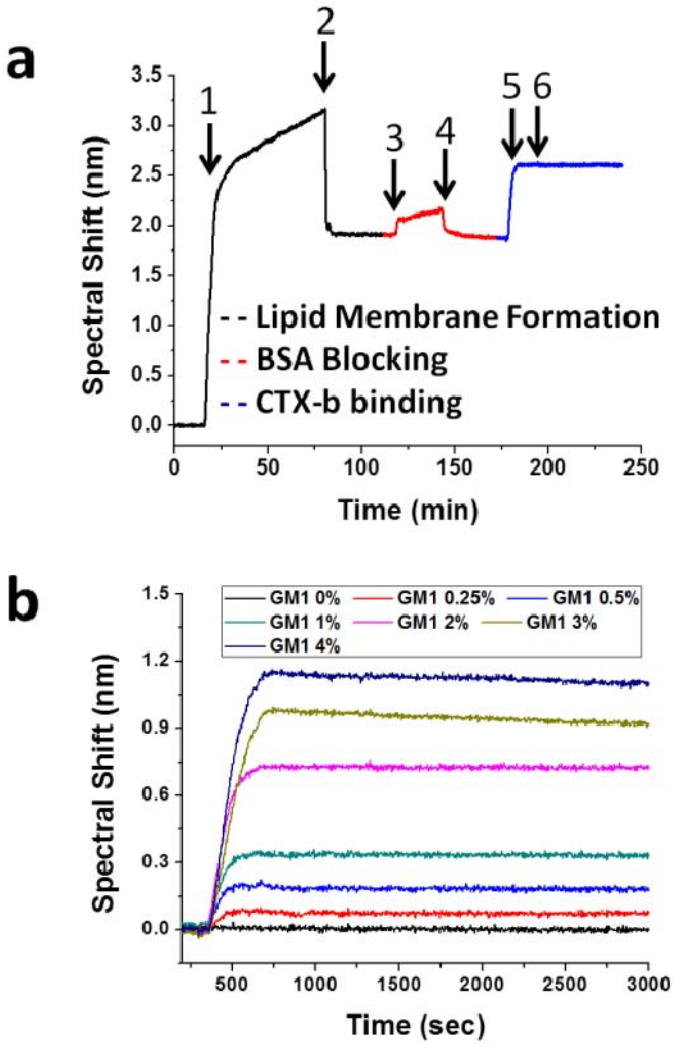

Figure 5.7 Sensorgram and GM1 receptor concentration assay. (a) Sensorgram showing SLB formation, BSA blocking and CTX-b binding to GM1. 1) vesicle injection; 2) washing excess vesicles from surface; 3) BSA blocking; 4) wash excess BSA; 5) inject CTX-b; 6) end CTX-b injection and begin dissociation step by washing the channel with PBS. (b) Binding kinetics curves of 50 nM CTX-b with SLBs containing various concentration of GM1. The kinetic curves clearly show fast association of CTX-b to GM1 and slow dissociation of CTX-b from GM1. The maximum spectral shifts increase linearly with the amount of GM1 receptor up to 2 mol % concentration. Figure is adapted from Lee *et al*.,[226]

5.5.4 Multichannel binding kinetics and affinities for CTX-b - GM1

Figure 5.8 shows a concentration assay of CTX-b binding to GM1 using multichannel SPR imaging spectroscopy. CTX-b concentration ranged from 400 to 3.13 nM and the GM1 receptor concentration is fixed to 2 mol %. 40 channels were used for simultaneous binding kinetic experiments (5 channels × 8 different concentrations). The other 10 channels are used for the negative control SLBs with no GM1 and for channels that compensate for bulk refractive index shift. 50nM CTX-b was also injected into the negative control channels. Due to the multichannel microfluidics and SPR spectral imaging setup, 40 different binding interactions can be measured in parallel. The binding kinetic curves are highly stable over all channels and clear kinetics were observed with CTX-b concentrations as low as 6.25 nM. Based on the 40 binding kinetics, the dissociation rate constant (k_d), association rate constant (k_a), and equilibrium dissociation constant (K_D) between cholera toxin b (CTX-b) and ganglioside (GM1) are extracted simultaneously. For analysis of molecular binding kinetics, the model for a 1:1 interaction where one analyte molecule binds with one receptor at a single binding site is used. From equation (2.49) in the chapter 2, the dissociation rate constant (k_d) can be obtained from a linear slope in a plot of $\ln(R_a/R_t)$ versus time. Since the dissociation between GM1 and CTX-b occurs linearly, k_d of GM1 and CTX-b can be determined from a slope of dissociation response of the kinetic curve. After acquiring k_d, the k_a value can be calculated from the time constant, Ck_a+k_d, obtained from a linear slope in a plot of $\ln(dR/dt)$ versus time. The kinetic constants calculated using a 1:1 binding analysis method are shown in Table 5.1 Although the dissociation constant (K_D) obtained from

each concentration varies from sub-nM to ~ 2 nM, they are comparable to previously reported values.[9,156,162,163]

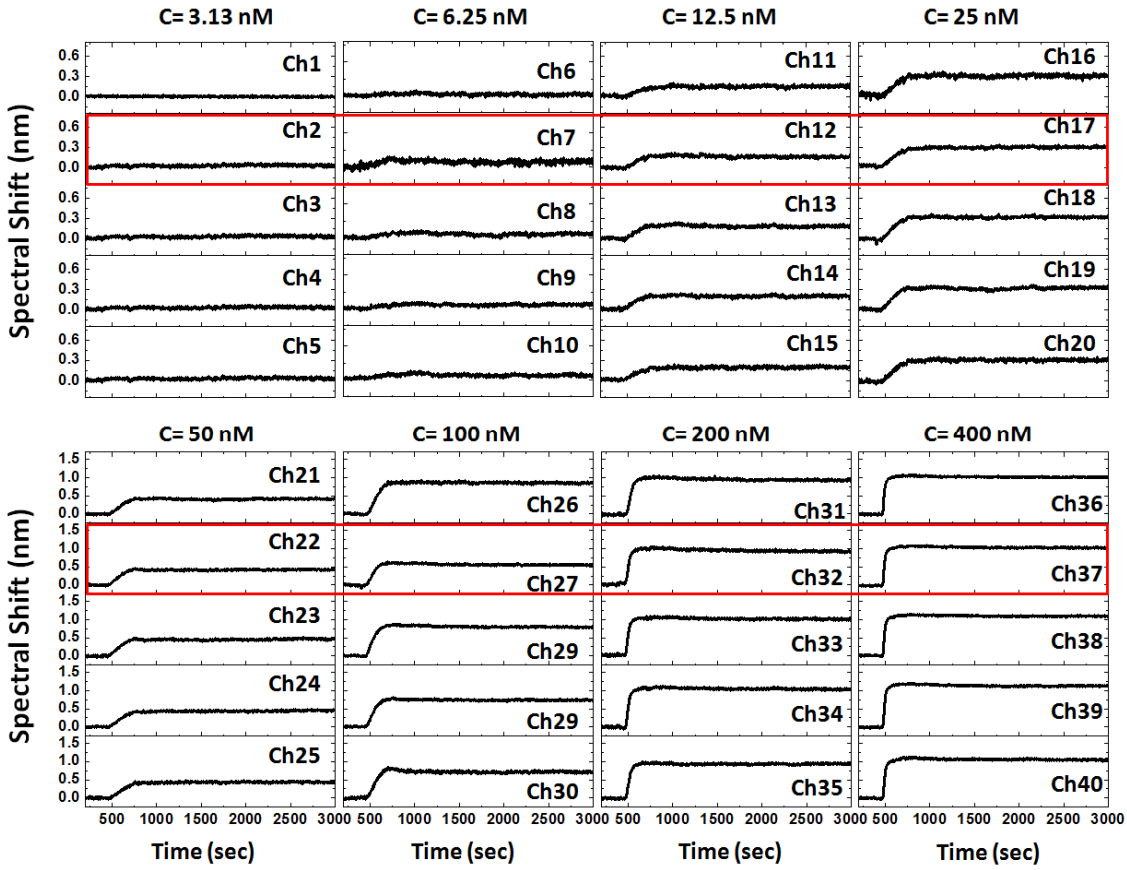

Figure 5.8 A CTX-b concentration assay to 2 mol % GM1 using multichannel SPR imaging spectroscopy. 40 different binding interactions are measured in one experiment. The binding kinetic curves are highly stable over all channels and clear kinetics are observed with CTX-b concentrations as low as 6.25 nM. Figure is adapted from Lee *et al.*,[226]

Table 5.1 Binding and dissociation rate constants for CTX-b to GM1. Binding rate constants and dissociation constants for CTX-b binding to lipid membranes containing GM1 measured by multichannel SPR imaging spectroscopy using metallic nanohole arrays. Table is adapted from Lee *et al*.,[226]

CTX-b Concentration (nM)	k_d (1/s)	k_a (1/M·s)	K_D (nM)
6.25	$6.46 \pm 2.7 \times 10^{-5}$	$1.64 \pm 0.6 \times 10^{5}$	0.39 ± 0.08
12.5	$4.27 \pm 1.0 \times 10^{-5}$	$3.26 \pm 1.9 \times 10^{5}$	0.19 ± 0.15
25	$4.10 \pm 2.7 \times 10^{-5}$	$1.44 \pm 1.2 \times 10^{5}$	0.32 ± 0.06
50	$3.55 \pm 3.5 \times 10^{-5}$	$3.29 \pm 3.2 \times 10^{4}$	1.07 ± 0.03
100	$5.13 \pm 2.1 \times 10^{-5}$	$3.29 \pm 0.9 \times 10^{4}$	1.53 ± 0.29
200	$1.25 \pm 0.4 \times 10^{-4}$	$6.01 \pm 2.0 \times 10^{4}$	2.34 ± 1.35
400	$9.40 \pm 0.7 \times 10^{-5}$	$8.20 \pm 1.1 \times 10^{4}$	1.17 ± 0.24

Figure 5.9a shows representative binding kinetics with CTX-b concentrations ranging from 3.13 to 400 nM. With the increase of analyte concentration, the spectral response increases but approaches a maximum. The limit of detection (LOD), commonly defined as 3 × the signal-to-noise ratio (S/N), is generally the smallest detectable concentration for a given instrument. However, when seeking to extract quantitative binding relationships, it is more advantageous to determine the practical limit of quantification (LOQ), which we estimate as 10 × S/N. To calculate LOQ of CTX-b binding to GM1 in the SPR spectral imaging setup, the maximum spectral shifts to the SD of the baseline noise versus the analyte concentration are plotted in Fig. 5.9b. Based on the S/N versus analyte concentration plot, LOQ corresponding 10 × S/N is computed to 8.4 nM, which is

similar value from the minimum concentration showing the apparent spectral shift in real-time binding kinetics. Thus, binding kinetics at 3.13 nM is not extracted.

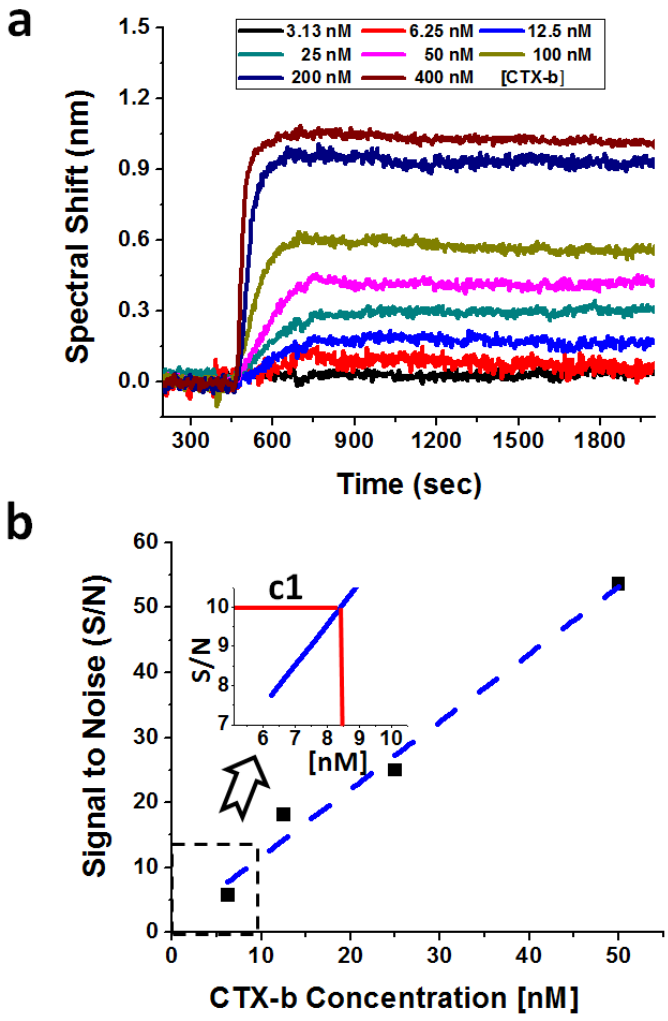

Figure 5.9 The representative binding kinetics of CTX-b to GM1 and the limit of quantification (LOQ) plot. (a) The representative binding kinetics at different concentration of CTX-b. The spectral response increases with the analyte concentration but approaches to a maximum. (b) The plot of signal-to-noise ratio (S/N) versus concentration of CTX-b for the limit of quantification (LOQ). LOQ corresponding 10 × S/N is calculated to 8.4 nM. Figure is adapted from Lee *et al.*,[226]

5.6 Conclusion

In this chapter, the drawbacks of commercial SPR biosensor and 2-D SPR imaging instruments are listed. This low-throughput, protein spotting with small volume, cross-contamination between spots, and position dependent inconsistent analyte concentration and binding rates are addressed by combining nanohole-based SPR image spectroscopy with a 50-channel microfluidics. The instrument combines an imaging spectrometer, a cooled CCD camera and a PDMS microfluidic chip to produce high throughput full-spectral imaging and accurate quantification of receptor-ligand binding kinetics. Multi-channel microfluidics is assembled on the silica-coated nanohole arrays. Highly uniform optical properties, which are the prerequisite for SPR spectral imaging can be acquired through homogeneous, large-area nanohole arrays fabricated by the template-stripping method. Device sensitivity extracted from the multichannel SPR spectral image is highly consistent over all channels. The measured refractive index resolution is around 7.7×10^{-6} RIU level, which can be further improved by using a faster CCD or CMOS camera. The parallel microfluidic channels partition the sensing area on the nanohole array into 50 isolated compartments, which is particularly valuable in using lipid or protein receptors incorporated in supported lipid membranes. To confirm the utility of our system, various conditions for binding kinetics of cholera toxin b subunit (CTX-b) to gangliosidemonosialic (GM1) receptors are measured in a single experiment. The dissociation constant (~sub-nM) acquired from nanohole-based multichannel SPR imaging spectroscopy matches very well with the previously reported results. LOQ defining the smallest detectable concentration is calculated to 8.4 nM, which is similar

value from the minimum concentration showing the apparent spectral shift in real-time binding kinetics. The temporal resolution of the instrument, which is 1-2 sec, can be improved by using a CCD or CMOS camera with faster data transfer rates. Since this general-purposes multi-channel imaging system allows acquiring full spectrum with high-throughput and allows individual functionalization of each channel with a wide range of receptors, our instrument will benefit a wide range of bioanalytical research.

CHAPTER 6

SURFACE-ENHANCED RAMAN SPECTROSCOPY (SERS) FOR BIOSENSING

Although SPR biosensors are actively used for real-time label-free biosensing, they do not provide us any chemical information. We can only tell whether there have been specific bindings between the receptors and analytes based on the refractive index changes. This mass redistribution-based sensing technique is powerful in some sense but always gives us indirect information, sometimes misleading the analysis to false-positive due to potential non-specific bindings. In contrast, surface-enhanced Raman spectroscopy (SERS), which is achieved by electromagnetic (EM) field enhancement, provides both the detection and the identification capability. This is because the inelastic Raman scattering either absorbed by or lost from the molecules is related to their specific vibrational or rotational motions of their molecular structure. Based on this unique SERS capacity, this technique has been widely used as a promising analytical tool for various

types of molecules such as anthrax[164], pollutants[165-167], nuclear waste detection[168] cellular sensing[169], and in vivo clinical research.[170] In this chapter, highly reproducible self-assembled nanohole SERS substrates using the NSL method will be presented. In addition, rapid and ultrasensitive SERS sensing using dielectrophoresis (DEP) will be presented. The work presented in the chapter 6.2 is the result of a collaborative effort with Professor Haynes group (with Dr. Kyle Bantz) and is mainly derived from the following publication:[65]

1. **S. H. Lee**, K. C. Bantz, N. C. Lindquist, S. -H. Oh, C. L. Haynes, ***Langmuir*** 25 (23), 13685-13693 (2009)

The chapter 6.3 is the result of a collaborative group effort, derived mainly from the following work:

2. S. H. Lee, S. Cherukulappurath, C. L. Haynes, S. -H. Oh, in preparation

6.1 Surface-enhanced Raman spectroscopy

6.1.1 Raman scattering

When a beam or wave collides with particles in the medium, light scatters. Mostly, this scattering conserves the initial energy, i.e. elastic scattering. Only the direction of light is changed randomly. In 1928, *Sir* C. V. Raman and K. S. Krishnan discovered new phenomena that small portion of photons scatter by molecules in liquids or gases inelastically with *degraded frequency*.[171] In their observation, every molecule shows a different degree of inelastic scattering, later termed a "fingerprint" of each molecule. This

unique capability has established this technique as a promising analytical tool for label-free molecular detection as well as identification.

The understanding of this inelastic scattering can be start with the quantum mechanics model. Figure 6.1 depicts the quantum mechanical model for three types of scattering. Incoming photon having energy $\hbar\omega_0$ excites the molecule to a higher-energy state. During the energy relaxation (scattering), if the energy is conserved, i.e. incoming photons do not interact with molecules, energy level comes back to the ground level. This type of scattering is called "elastic" or "Rayleigh" scattering. However, when incoming photons are related to vibrational and rotational motion of molecule, scattered photons can be relaxed to a different level of energy. This inelastic scattering is called "Raman" scattering named after C. V. Raman. If the scattered photon $\hbar(\omega_0 - \omega_1)$ has a lower energy than the incoming photons $\hbar\omega_0$, the energy is absorbed by the molecules at the vibrational or rotational state. It is called Stokes Raman scattering. Contrarily, if the scattered photon gains energy from the molecules $\hbar(\omega_0 + \omega_1)$, it is called anti-Stokes Raman scattering which shows typically weak intensity.

Although Raman scattering, compared to fluorescence, is very feeble in intensity, approximately 1 in 10^6-10^{10} photons are scattered inelastically,[171-173] it provides much more information about molecular structure and orientation than fluorescence. However, there is a way to boost this tiny signal to useable levels. When molecules are placed near a rough metallic surface, the Raman signal can be enhanced on the order of 10^4 ~ 10^8.[16,77,174] The coming chapter will discuss the mechanism and methods to confine the electromagnetic field in a small volume to understand this enhanced Raman signal.

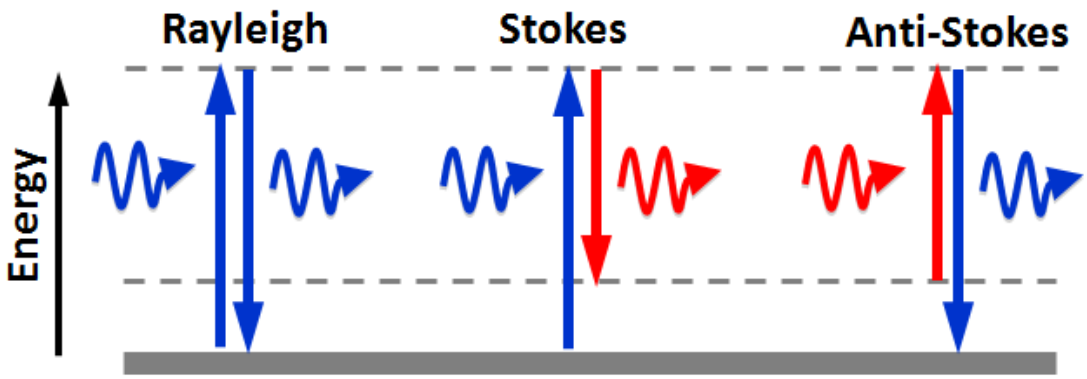

Figure 6.1 Quantum mechanical model of Raman scattering. An incoming photon will be relaxed to the same energy level during Rayleigh scattering. When it interacts with the molecular vibration and rotational movement, the scattered photon can lose the energy to the molecules or gain the energy from the molecules. The former is called Stokes Raman scattering, the latter is called anti-Stokes Raman scattering.

6.1.2 Surface-enhanced Raman scattering

Since Raman signal is a second order process, its intensity is very weak with a cross section of $10^{-29} \sim 10^{-31}$ cm^2/molecule. This characteristic of Raman requires a high power light source and a high density of analyte to be detected. Therefore, the Raman technique was not an effective tool for being used widely in the analytical chemistry field until the enhanced Raman effect was observed. Martin Fleischmann *et al.* observed an enhanced Raman effect on a roughened Ag film in 1974.[175] They concluded this enhancement was due to the increased electrode's surface area. However, three years later, Jeanmarie & Van Duyne first recognized this enhanced Raman intensity cannot be explained only with

the increased surface area, but is also do to another phenomenon to be discussed.[16] This enhancement was later termed surface-enhanced Raman scattering (SERS).

Figure 6.2 shows the surface enhanced Raman spectroscopy mechanism related with electromagnetic enhancement. An incident EM field resonantly is localized and amplified by the nanoparticle. Likewise, the scattered Raman signal will be also localized and intensified by the nanoparticle. Because both fields are enhanced, the SERS signal scales with the fourth power of the field enhancement. This electromagnetic enhancement due to the LSPR and enhanced field intensity near the nanostructure is typically on the order of $10^4 \sim 10^8$. In addition, an extra $10 \sim 100 \times$ enhancement is attributed to chemical enhancement which is related with charge interactions between the metal and adsorbed molecules.[172]

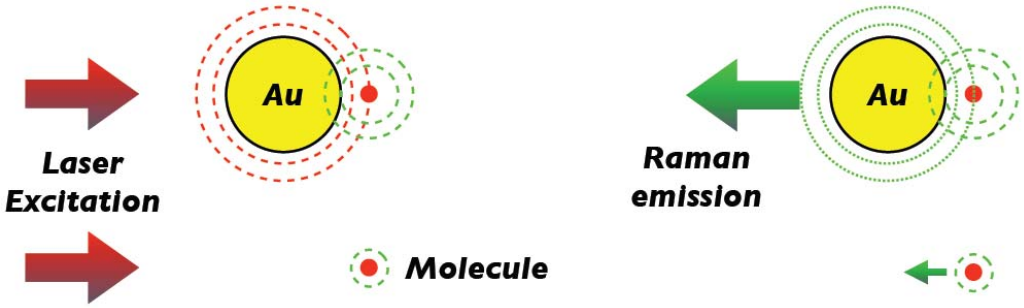

Figure 6.2 Mechanisms of electromagnetic enhancement. A gold nanostructure will enhance both (a) incident and (b) scattered fields. When the molecules are palced near the nano-size metallic surface, the Raman signal will be enhanced by the fourth power of the field.

6.2 Self-assembled plasmonic SERS substrate

One of the necessary components to create SERS has been sub-wavelength structural features, i.e. nanostructures. Because of this dependence on size which is technologically challenging to producenumerous fabrication methods have been employed to develop effective and reproducible SERS substrates.[64,79,176-179]

Besides being useful as an SPR biosensor platform, nanohole arrays are also inherently promising as surface-enhanced Raman spectroscopy (SERS) substrates. With the advance of nanofabrication methods, various techniques for nanoholes as well as the process parameters such as hole lattice spacing have been explored to achieve SERS activity.[176,180-182] While these results are promising, further demonstration of improved SERS on nanohole arrays is warranted, particularly if this can be accomplished using arrays produced using a massively parallel fabrication strategy.

6.2.1 Fabrication of elliptical nanohole arrays

In chapter 3, the fabrication method of self-assembled nanohole arrays was introduced. Elliptical nanoholes can also be created by using same NSL method with angle-resolved metal deposition process after shrinking the nanospheres by RIE. Figure 6.3 shows SEM of different shapes of nanohole arrays fabricated with being tilted to 0^o, 30^o, 45^o, and 60^o during metal deposition. The aspect ratio (AR) at 30^o, 45^o, and 60^o tilt angle was calculated to 1.1, 1.2, 1.4, respectively. The AR, an important parameter for ellipses, is dependent on the tilt angle of the substrate as well as the sphere size. However, the

nanospheres at high tilt angle or having a small size will not be removed readily, limiting a high AR elliptical hole fabrication.

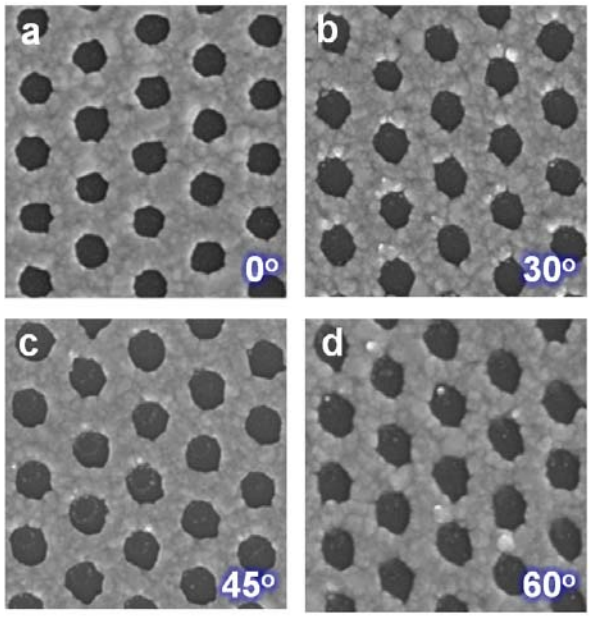

Figure 6.3 SEM of the elliptical nanohole arrays. The substrate was tiled at (a) 0^{o}, (b) 30^{o}, (c) 45^{o}, (d) 60^{o}. The aspect ratio (AR) ranges from (b) 1.1, (c) 1.2, (d) 1.4.

6.2.2 Fabrication of "spiky" plating on the nanohole arrays

Electroless plating of silver onto the nanohole array was prepared using a protocol described by Halas and coworkers.[183] A nanohole array substrate was submerged in a solution of 1.2 mL of Acacia (500 mg/L) with 0.2 mL of buffer solution (1.5 M citric acid/0.5 M sodium citrate, pH = 3) and 0.3 mL of silver lactate (37 mM in water). Then, 0.3 mL of hydroquinone (0.52 M in water) was added while stirring the mixture vigorously. The Acacia stabilizes the silver ions and allows for slower reduction of the

silver, which causes the formation of "spiky" silver deposition. The substrates were removed from the solution after 4, 6 or 8 min. Figure 6.4a shows the resulting structures after 4 minutes in the plating solution; 6 minute plating bath exposure was also performed on identical substrates (Figure 6.4b).

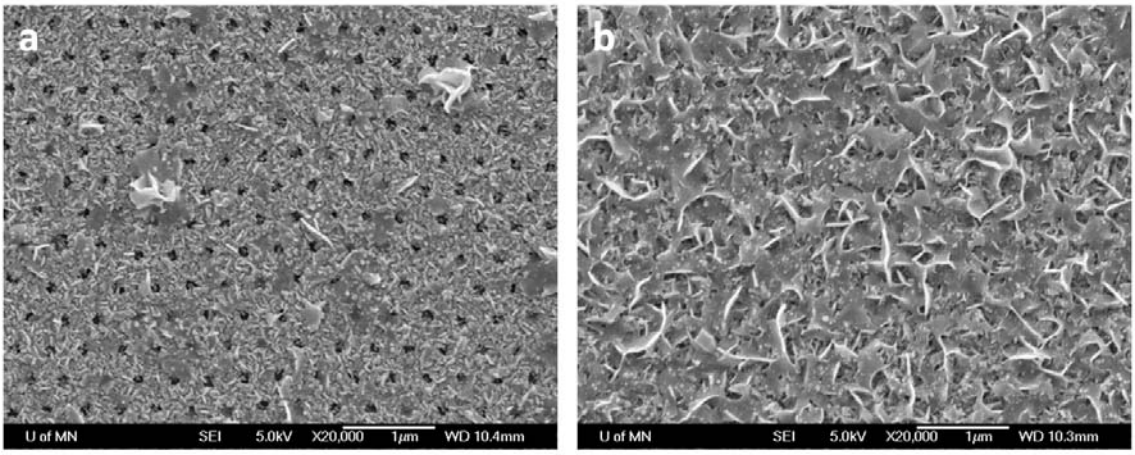

Figure 6.4 SEM of Ag electroless plating onto the nanohole array. (a) 4 min and (b) 6 min After 6 min, most of nanohole arrays are blocked by “spiky” plating. Figure is adapted from Lee *et al*.,[65]

6.2.3 SERS from the self-assembled nanohole arrays

After fabricating nanohole arrays, SERS measurements were performed using benzenethiol (BZT) molecules. For initial SERS characterization, all substrates were dosed with 1mM BZT in ethanol, an efficient Raman scatterer with well-characterized surface coverage. SERS measurements were performed on the circular nanohole arrays as well as the elliptical nanohole arrays and compared to both flat Ag substrates and the

commonly used AgFON substrate. Each substrate was placed in 2 mL of the ethanolic BZT solution for 16 h at ambient conditions to facilitate monolayer formation. The substrates were then removed from the ethanolic solution and rinsed with ethanol before they were mounted in the microscale Raman sample holder. SERS was excited with a Millenia Vs 532 nm excitation laser with p-polarization (Spectra-Physics, Mountain View, CA) or a 12 mW HeNe 632.8 nm excitation laser with random polarization (Newport Corporation, Irvine, CA). Neutral density filters were added to the optical path to achieve desired incident powers. In both cases, the laser beam was first passed through the appropriate interference filter (Melles-Griot, Rochester, NY) and then guided into a 20× microscope objective (Nikon, Melville, NY) and onto the sample. The scattered light was collected back through same 20x objective and Rayleigh scattered light was removed using the appropriate notch filter (Semrock, Rochester, NY) before collection. Detection was accomplished using a 0.5 m Spectra-Pro 2500i single monochromator and a Spec 400B liquid nitrogen-cooled CCD chip (both from Princeton Instruments/Acton, Trenton, NJ). In all cases, SERS spectra were measured from three randomly chosen areas on a given substrate. Spectra recorded with near-infrared excitation (752 nm) were excited using an Innova90 Krypton laser (Coherent Inc., Santa Clara, CA) and collected with a WITec alpha300 R scanning confocal Raman microscope with a UHTS300 spectrometer and DV401 CCD detector (all from WITec, Savoy, IL) with a 100× objective (Olympus, Center Valley, PA). In this case, spectra were measured from a 10 μm × 10 μm area.

As can be seen in Figure 6.5b, the circular nanohole arrays yield high signal-to-noise SERS spectra, with no spectral evidence for polystyrene residue on the substrate. At 532 nm excitation wavelength, the calculated enhancement factor, 1.70×10^4, is comparable to that measured from a AgFON, 2.62×10^4 (Figure 6.5a), and significantly higher than that measured from a flat 50-nm-thick Ag film, 1.07×10^3(Figure 6.5c). Based on the understanding that SERS enhances both exciting and scattered photons, the ideal nanohole substrate would have a SPR centered between the excitation wavelength and the Stokes scattering wavelength of interest.

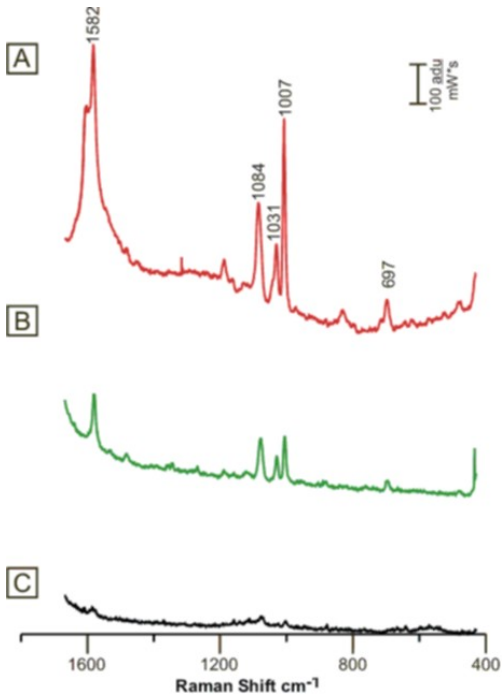

Figure 6.5 SERS spectra of 1 mM BZT. (a) on a AgFON, (b) on a circular nanohole array and (c) on 50 nm flat silver. P = 0.32 mW, t = 180 s, and λ_{ex} = 532 nm. Figure is adapted from Lee *et al*.,[65]

6.2.4 Enhancement factors (EFs)

EFs were all calculated with the intense benzene breathing stretch at approximately 1000 cm^{-1} shift for both the liquid and surface-adsorbed BZT using the equation:

$$EF = \frac{N_{vol} \times I_{surf}}{N_{surf} \times I_{vol}} \tag{6.1}$$

,where N_{vol} is the number of BZT molecules contributing to the normal Raman signal, N_{surf} is the number of BZT molecules contributing to the SERS signal, and I_{surf} and I_{vol} are the intensities of the scattering band of interest in the SERS and normal Raman spectra, respectively. The packing density for BZT on Ag, as reported in the literature, is 6.8 x 10^{14} molecules/cm^2.[184,185] Using the surface area obtained from AFM or SEM measurements and the laser spot size, it is then possible to calculate N_{surf} and the resulting enhancement factor.

Table 6.1 summarizes the enhancement factors measured at all three excitation wavelengths for the circular nanohole arrays, with values up to 8 × 10^5. These enhancement factors are comparable to or higher than those reported in the literature for nanohole arrays fabricated using traditional methods,[181,182] and as expected, are significantly larger with the on-resonance 632.8 and 752 nm excitation wavelengths than with the off-resonance 532 nm excitation. Comparison to a flat Ag film of the same thickness demonstrates that the nanohole array gives an order of magnitude better average enhancement. In addition, SERS spectra were also measured from the elliptical nanohole array substrates (Table 6.1). In general, the elliptical profile did not yield a significantly different enhancement factor than the circular profile.

Table 6.1 Average EF values over three different wavelengths. Table is adapted from Lee *et al*.,[65]

Sample Tilt Angle	Average EF		
	λ_{ex} = 532 nm	λ_{ex} = 633 nm	λ_{ex} = 752 nm
0°	1.70E+04	8.13E+05	1.24E+05
30°	1.85E+04	1.88E+06	4.18E+04
45°	1.63E+04	7.51E+05	2.05E+04
50°	1.35E+04	7.15E+05	8.98E+04
55°	2.23E+04	5.42E+05	7.03E+04
60°	2.97E+04	1.11E+06	4.48E+04
Flat Ag	1.07E+03	5.55E+04	N/A
AgFON	2.62E+04	9.04E+04	N/A

6.2.5 SERS from the "spiky" plating on the nanohole arrays

While the periodic structure of the nanohole array clearly yields improved SERS performance, further improvement of the enhancement factor would facilitate lower detection limits in future sensor applications. The FDTD simulations performed in the chapter 3.1.5 suggest that the majority of the electromagnetic enhancement originates at the edges of the nanoholes. In an effort to exploit the remainder of the substrate, the nanohole arrays were immersed in a Ag plating bath known for producing high surface area "spiky" features.[183] For control purposes, a flat Ag film was immersed in the plating bath simultaneously. Figure 6.6 includes representative benzenethiol SERS spectra recorded from both the normal and enhanced substrates with 532 nm excitation while Table 6.2 delineates the measured enhancement factors using both 532 nm and 632.8 nm excitation for both flat and nanohole array substrates before plating and after either 4 or 6

minutes in the plating bath. These data demonstrate that a 4 minute immersion in the plating bath gives an additional order of magnitude SERS enhancement on either a flat or a nanohole array substrate at either excitation wavelength, yielding enhancement factors as large as 3×10^6. Transmission measurements of the SPR were attempted on these substrates but the recorded spectra were very broad, indicating extremely heterogeneous topographical features. While the substrates that were immersed in the plating bath for 6 minutes do give a slightly improved enhancement factor over the unplated substrates, these substrates were not as efficient as the substrates immersed for only 4 minutes. Electron microscopy analysis of the substrates immersed for 6 minutes (Figure 6.4b) revealed that the nanohole structure was nearly entirely obscured, largely negating the enhancement introduced by the nanohole grating structure. Effort was made to avoid obscuring the nanohole substrate by performing the plating directly on the RIE-etched template before sphere removal (without a vapor deposited metal layer). Plating bath immersion times of 4, 6, and 8 minutes all produced a substrate where the nanosphere mask could not be removed by normal means; thus, it was not possible to achieve the desired nanohole array structure.

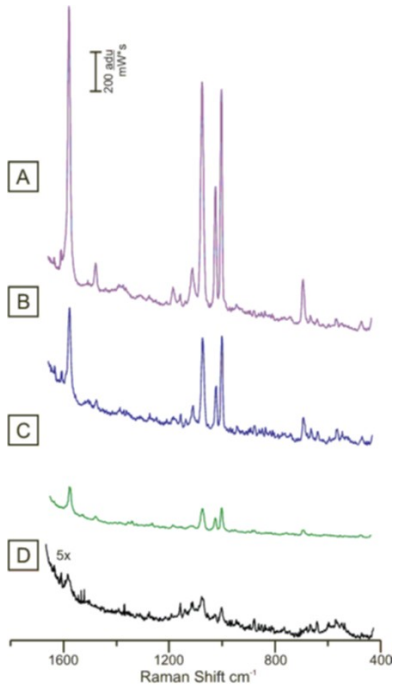

Figure 6.6 SERS spectra from both the enhanced and normal substrates. (a) 4 min Ag plated nanohole array, (b) 4 min Ag plated flat silver film, (c) a standard nanohole array and (d) 5x a flat silver film. All substrates were exposed to 1 mM BZT prior to SERS measurements. P = 0.32 mW, t = 180 s, and λ_{ex} = 532 nm. Figure is adapted from Lee *et al*.,[65]

Table 6.2 Average EF values for two different plating conditions and wavelengths.

Table is adapted from Lee *et al*.,[65]

Sample	Average EF	
	λ_{ex} = 532 nm	λ_{ex} = 633 nm
Nanohole array	1.70E+04	8.13E+05
Nanohole array + 4 minute plating	1.58E+05	3.26E+06
Nanohole array + 6 minute plating	7.51E+04	2.08E+05
Flat Ag film	1.07E+03	5.55E+04
Flat Ag film + 4 minute plating	2.39E+04	1.18E+06
Flat Ag film + 6 minute plating	2.09E+04	6.11E+04

6.3 Rapid and ultrasensitive SERS detection using Dielectrophoresis (DEP)

To excite Raman-active molecules with the strong electromagnetic fields, various nanostructures such as Ag film over nanosphere (AgFON), nanohole, nanowire, nanotip, nanoshell have been employed as Surface Enhanced Raman Spectroscopy (SERS) substrates.[65,176,186-192] Among them, metallic nanogap substrates have been investigated extensively in SERS application since the metal-insulator-metal (MIM) structure is optimum for extreme electromagnetic (EM) field confinement, leading to dramatically enhanced EFs. Since localized surface plasmon resonance (LSPR) plays a key role in SERS enhancement, it is highly advantageous to make the size of gap within the decay length of local electromagnetic field, (l_d ~ 5 - 6 nm). However, the most gap size fabricated by conventional techniques such as EBL, NSL for SERS are in the range of 100 nm. [193,194] To address this fabrication barrier, new approaches for squeezing the gap size to the length scale of localized evanescent field has been implemented by many innovative works.[178,195] Recently, Im et al demonstrated wafer-scale fabrication having sub-10-nm vertical nanogap arrays and reported more than 10^9 EFs at 5 nm gaps.[179] Such planar-type nanogap structures have made great progress on improving the 'enhancement factor', however, it is not the best way for a rapid SERS detection since it requires a long incubation time for molecules to reach to the vicinity where strong electromagnetic fields are (i.e. inside the nanogap). Particularly, it is not a trivial work to position the target molecules on these nano-scale hotspots at ultra-low concentrations, i.e. picomolar (pM) or attomolar (aM). This diffusion-driven molecular adsorption method prohibits the use

of such enhanced devices for ultra-low concentration immunochemical biosensing or rapid SERS detection. To solve this diffusion limited molecular immobilization problem, new approaches which use suspension-type sensors have gained great attention recently.[196,197] Giant magnetoresistance (GMR) is one typical example of the suspension type sensors. Because the ability to scout the molecules in solution and bring them to the sensing area, GMR biosensor has successfully demonstrated ultra-sensitive device performance.[198-200] To implement this advantage of a suspension-type sensor for rapid and ultrasensitive SERS detection, dielectrophoresis (DEP) using Au nanoparticles (NPs) will be introduced and investigated in this work.

6.3.1 Dielectrophoresis

Dielectrophoresis (DEP) is a phenomenon where a non-uniform electric field exerts a force on a particle. By polarizing particles with alternating AC field, they are trapped toward or away from the high electric field intensity.[201,202] By optimizing the electrode design and DEP parameters used, high-density and dynamic nanogap structures can be formed between the electrodes with conventional micron-scale fabrication.

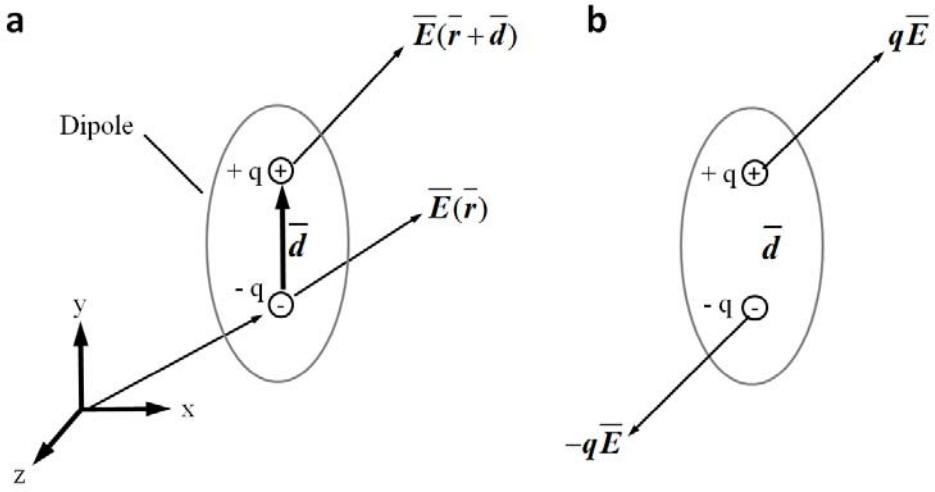

Figure 6.7 Representation of the force and torque exerted upon a small dipole by an electric field of force. (a) Net force on a small dipole of strength $p=qd$ in a nonuniform electric field. (b) Coulombic force components creating net torque on a small dipole of strength $p=qd$ in a uniform electric field. Figure is adapted from Jones *et al*.,[202]

Figure 6.7 shows the representation of the dipole in a non-uniform electric field. When the electric field $\vec{E}$ is applied on a small dipole, the net force on a small dipole is given by:

$$\vec{F} = q\vec{E}(\vec{r}+\vec{d}) - q\vec{E}(\vec{r}) \tag{6.2}$$

Here, the electric field can be expanded using a vector Taylor series expansion:

$$\vec{E}(\vec{r}+\vec{d}) = \vec{E}(\vec{r}) + \vec{d}\cdot\nabla\vec{E}(\vec{r}) + \cdots \tag{6.3}$$

since d is very small, it is natural to neglect above the second order terms. When substituting (6.3) into (6.2), net force equation yields:

$$\vec{\boldsymbol{F}} = \boldsymbol{q}\vec{\boldsymbol{d}} \cdot \nabla \vec{\boldsymbol{E}} = \vec{\boldsymbol{p}} \cdot \nabla \vec{\boldsymbol{E}} \tag{6.4}$$

, where p is dipole moment. For a small spherical neutral particles ($\boldsymbol{r}_p$) having a permittivity, ε_p, in a dielectric medium with permittivity ε_m, this ideal dipole moment p can be replace with p_{eff} :

$$\vec{\boldsymbol{p}}_{\boldsymbol{eff}} = 4\pi \boldsymbol{r}_p^3 \varepsilon_m \frac{(\varepsilon_p - \varepsilon_m)}{(\varepsilon_p + 2\varepsilon_m)} \vec{\boldsymbol{E}} \tag{6.5}$$

Thus, the idealized net force acting on a spherical particle in a non-uniform electric field now can be expressed as:

$$\vec{\boldsymbol{F}} = \vec{\boldsymbol{p}}_{\boldsymbol{eff}} \cdot \nabla \vec{\boldsymbol{E}} = 2\pi \boldsymbol{r}_p^3 \varepsilon_m (\frac{\varepsilon_p - \varepsilon_m}{\varepsilon_p + 2\varepsilon_m}) \nabla \left| \vec{\boldsymbol{E}} \right|^2 \tag{6.6}$$

Since conductivity of both particle and medium is dependent of applied frequency, the particle and medium will have a complex permittivity ($\varepsilon_p^*, \varepsilon_m^*$). The net force generated by the non-uniform AC electric field can be defined as:

$$\vec{\boldsymbol{F}} = \vec{\boldsymbol{p}}_{\boldsymbol{eff}} \cdot \nabla \vec{\boldsymbol{E}} = 2\pi \boldsymbol{r}_p^3 \varepsilon_m \boldsymbol{K}(\omega) \nabla \left| \vec{\boldsymbol{E}} \right|^2 \tag{6.7}$$

,here $\boldsymbol{K}(\omega)$ is the complex Clausius-Mossotti (C-M) factor which can be shown as:[202]

$$\boldsymbol{K}(\omega) = (\frac{\varepsilon_p - \varepsilon_m - \boldsymbol{j}(\sigma_p - \sigma_m)/\omega}{\varepsilon_p + 2\varepsilon_m - \boldsymbol{j}(\sigma_p + 2\sigma_m)/\omega}) \tag{6.8}$$

At low frequency regime, the C-M factor becomes conductivity dependent:

$$\mathrm{Re}\left[\boldsymbol{K}\right] = (\frac{\sigma_p - \sigma_m}{\sigma_p + 2\sigma_m}), \text{ for } \omega \to 0 \tag{6.9}$$

,and at high frequency regime, the C-M factor becomes permittivity dependent:

$$\mathrm{Re}[\boldsymbol{K}] = \left(\frac{\varepsilon_p - \varepsilon_m}{\varepsilon_p + 2\varepsilon_m}\right), \text{ for } \omega \gg 0 \tag{6.10}$$

By using the C-M factor, the DEP force generated by the non-uniform AC electric field can be defined as:

$$\vec{\boldsymbol{F}}_{DEP} = 2\pi\varepsilon_m \boldsymbol{r}^3 \,\mathrm{Re}[\boldsymbol{K}]\nabla \boldsymbol{E}_{rms}^2 \tag{6.11}$$

,where ε_m is the permittivity of the surrounding medium, r is the radius of the nanoparticle, $\mathrm{Re}[\boldsymbol{K}]$ is the real part of the C-M factor, and $\boldsymbol{E}_{rms}$ is the root-mean-squared value of the applied electric field. Figure 6.8 shows the DEP spectra having different combinations of conductivity and permittivity. Figure 6.8a shows when the medium has higher conductivity and lower permittivity such as insulating polymer materials in liquid medium. Figure 6.8b shows the case of Au NPs, most popular material for DEP, suspended in aqueous solution.

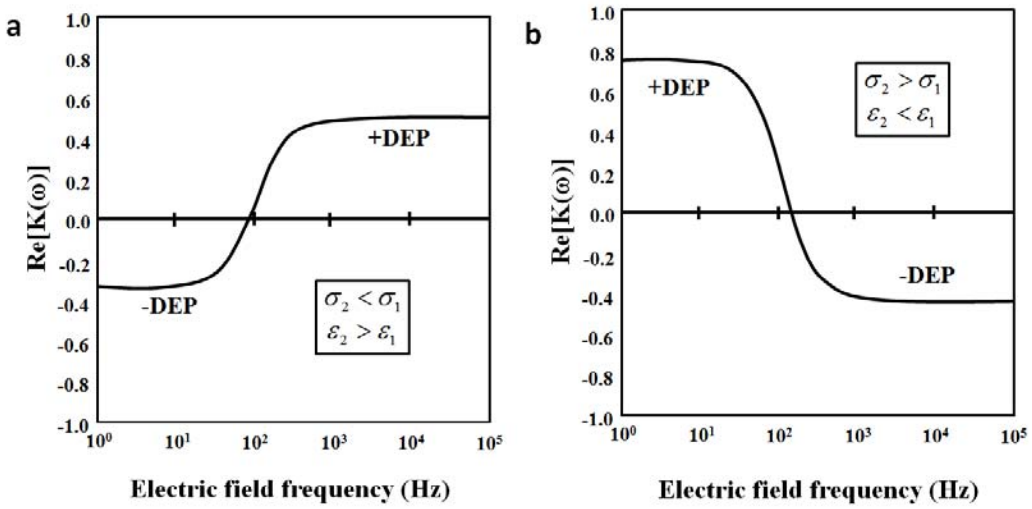

Figure 6.8 Dielectrophoresis (DEP) spectra of homogeneous dielectric spheres with ohmic loss. (a) $\sigma_p < \sigma_m$, $\varepsilon_p > \varepsilon_m$ (b) $\sigma_p > \sigma_m$, $\varepsilon_p < \varepsilon_m$. Figure is adapted from Jones et al.,[202]

Since the C-M factor of Au NPs in water shows close to +1 below 10 GHz,[203] the Au NPs in an aqueous medium will experience positive DEP force, and will be attracted toward the electrodes during the experiment.

6.3.2 Au nanoparticle pearlchain formation by DEP

Formerly, nanogaps using a Au NPs suspension were formed by random aggregation or DNA hybridization.[204,205] By carefully monitoring the signal from the sub-10-nm size gap, many spectroscopic measurements for LSPR biosensing and SERS detection have successfully been done with this technique. After the fundamental study for electromechanics of particles,[202] Many attempts have been made to control the formation of dynamic nanogaps. For a pearlchain formation using DEP, the parametric studies for

highly anisotropic pearl-chains containing sub-10-nm gaps were reported.[206,207] Figure 6.9a shows the concept of a dynamic nanogap formation for rapid SERS detection. Au NPs are mixed in a solution with the molecules of interest before the DEP process. During the vortex mixing, SERS molecules interact with Au NPs and adhere to the Au surface. Since the Au NPs can approach to the vicinities of the molecules during mixing, it is possible to shorten the incubation time dramatically (< 30 sec) at the *nM* level concentration. During the DEP process, molecules adhered to Au NPs are attracted together and scatter inelastic Raman signal strongly due to the enhanced EM field in the nanogap. Figure 6.9b shows a scanning electron micrograph (SEM) of the comb type electrode pattern used in the experiments. The comb patterns have been fabricated by a photolithography followed by 200nm-thick Au deposition with a 5 nm Ti adhesion layer, and lift-off process. The width and gap between the electrodes are set to 1 μm aiming to obtain strong fields between the electrodes and to minimize the pearlchain formation time. A single device consists of five such electrodes that are connected in common to two electric contact pads. Wafer scale fabrication of DEP device enables the dynamic nanogap formation with a minimum cost, enabling the intensive SERS study for the detection and the identification of SERS active molecules (Figure 6.9c). The measured absorption peak of the Au NPs is found to be around 520 nm, which is a good agreement with that of the similar size of Au NPs.[208] Before DEP experiments, the Au NPs solution is filtered through a membrane filter having 0.45 μm diameter holes to maintain the homogeneous particle size.

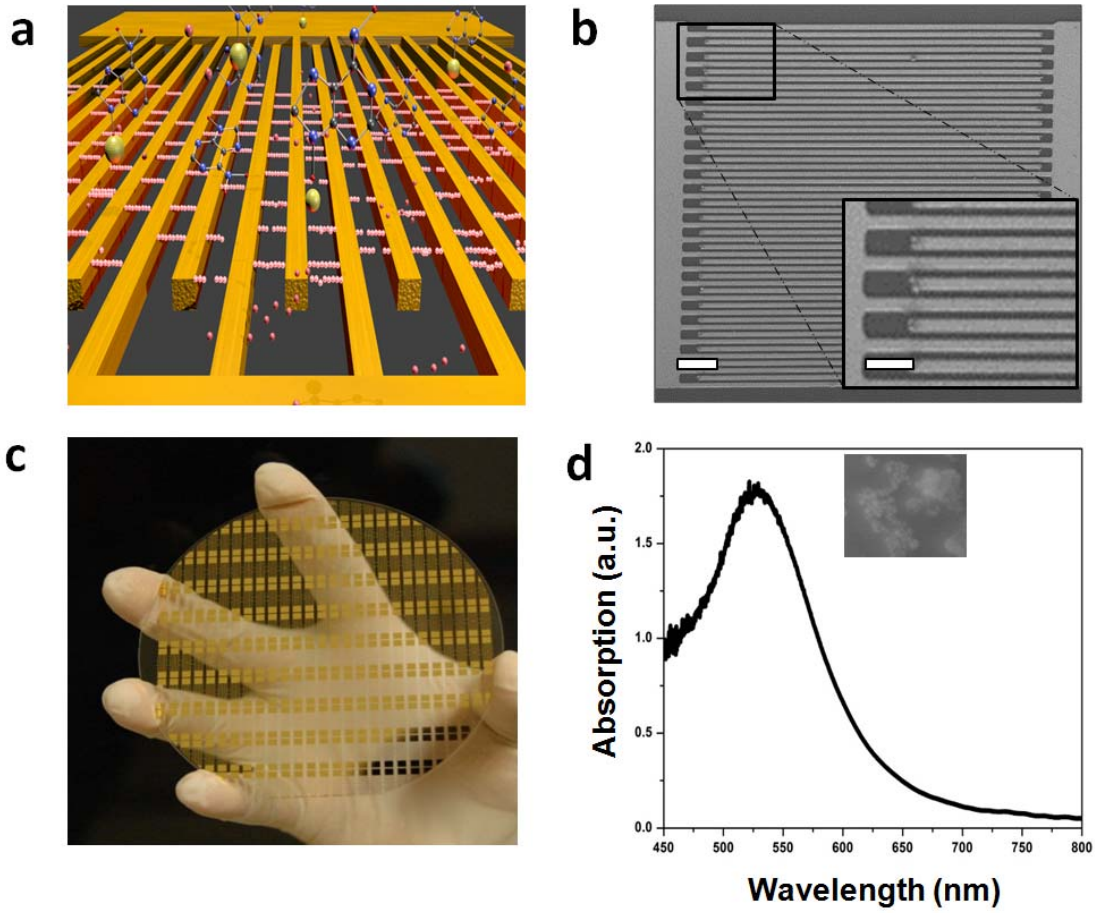

Figure 6.9 DEP Methods and materials. (a) Schematic illustration of pearlchain formation by DEP and in-situ SERS detection. (b) SEM image of an electrode used in the experiment. Each electrode consists of comb like pattern as shown in the inset. Each device had 5 such electrodes. Scale bar is 10 μm in the main image and 1 μm in the inset. (c) A whole wafer of several such devices fabricated by photolithography, Au (200nm thick) / Ni (5 nm thick) deposition, followed by lift-off method. (d) Extinction spectrum of Au NPs used in the experiment.

In order to form dynamic nanogap structures by DEP, a 2uL of the Au NPs solution was drop casted on the electrode and covered with a glass cover slip to reduce evaporation. The addition of a cover slip also increases the amount of Au NPs near the

electrodes. To achieve a highly directional pearl-chain formation, extensive experiments have been conducted to find the optimum frequencies, field potential, and formation time.{Hermanson,2001;Gierhart,2004;Zheng,2003;Kretschmer,2004;Holzel,2005}. An AC potential of 10 Vpp at 1MHz was applied through wire probes connected to the electrode leads. In order to determine the optimal time for pearl chain formation and to avoid heating and subsequent melting of the Au NPs, DEP was performed on several devices for different amounts of time. Figure 6.10 shows the scanning electron micrograph (SEM) of pearlchain formation at different times after applying the potential. After 40 seconds of application of the AC field, Au NPs start to form pearl chains at the edge of the electrodes. With time the pearl chain grows as greater numbers of Au NPs are attracted by the DEP force. In 1 min and 45 sec the pearl chain is completed and the two electrodes get connected and brought to a common potential. Applying potential any further will increase the current flow through the pearl chains, heat them up, and eventually melt the Au NPs (Figure 6.10e and 6.10f). The series of images in Figure 6.10 clearly show that the optimum time for nice pearl chain formation is about 1 min and 45 sec. Pearlchains are formed over the entire electrode area in this time as shown in Figure 6.10h. A zoomed-in image depicts the quality of the pearlchains formed (Figure 6.10g).

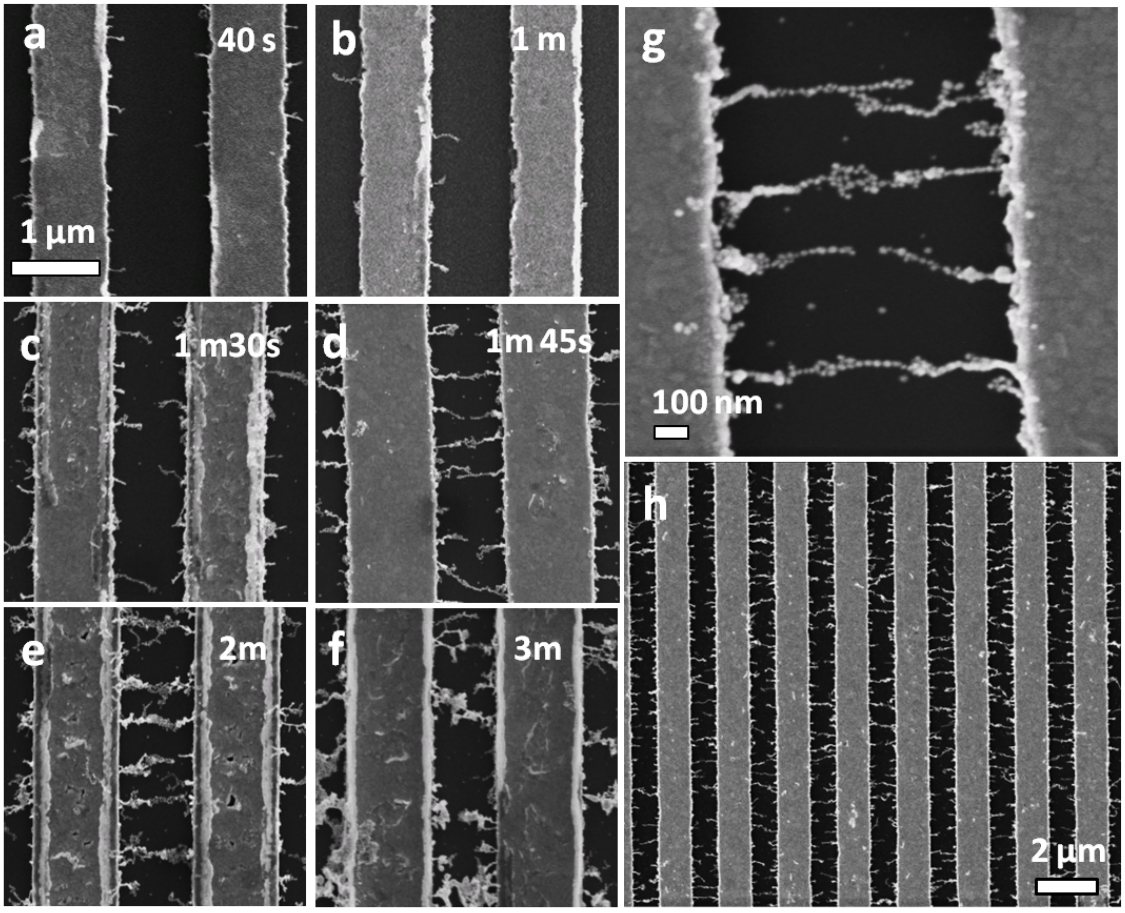

Figure 6.10 SEM images of pearlchain formation. After (a) 30 s (b) 1 min (c) 1 min 30s (d) 1 min 45s (e) 2 min (f) 3 min of application of AC voltage of 10 Vpp at 1 MHz to the electrodes. (g) Zoomed in SEM image to illustrate the quality of the pearlchains. (h) Multiple pearlchains are formed.

6.3.3 In-situ, rapid SERS detection

In order to correlate the pearlchain formation with SERS signal enhancement, the device on which pearl chains were formed by DEP for 1 minute and 45 seconds was incubated with 1mM benzenethiol (BZT) solution, whose Raman spectrum is well characterized. Figure 6.11a shows the SERS spectrum of BZT from the pearlchains. Diffraction limited spot from a 752 nm Kr laser was used as the Raman excitation source. Confocal Raman microscopy was used to map the distribution of high SERS spots in the sample. Raman intensity peak of BZT at 1069 cm^{-1} representing the in-plane C-C-C bending as well as the C-S stretching modes was used to generate the confocal scanning image over an area of 20 um^2 on the comb structures. It is clear that the intense hotspots (high intensity SERS signals) are between the electrodes and are coming from the pearlchains in the gap (Figure 6.11b). A zoomed-in confocal image shown in the inset in Figure 6.11b confirms that the signal is indeed coming from the pearl chains. Due to the low resolution (~ 500 nm) of the system at this wavelength, it is not possible to resolve signals from individual nanoparticles.

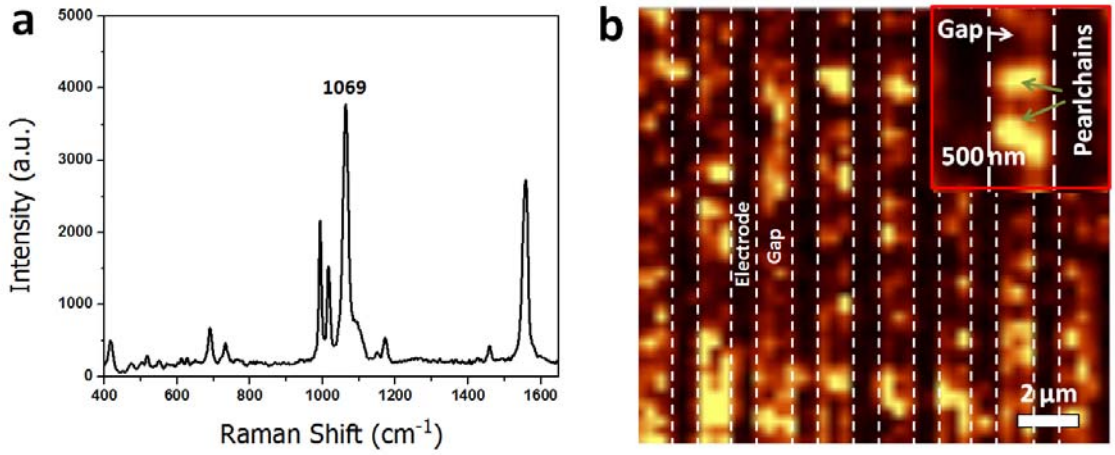

Figure 6.11 Scanning confocal Raman imaging on benzenethiol-incubated pearlchains. (a) SERS spectra of 1mM benzenethiol (BZT) incubated on the pearl chains formed by DEP. 1069 cm^{-1} peak of this spectra is used to construct the subsequent images (b) Confocal Raman image of the device after pearl chain formation using DEP and incubation with 1mM BZT. A zoom-in image showing the SERS signals coming from the pearlchains formed between the electrodes (Inset). The confocal Raman result is courtesy of Sudir Cherukulappurath in our group.

In order to demonstrate the rapid in-situ SERS measurement capability of the device, DEP experiments were conducted during SERS measurements. 2µL of 1mM BZT and the Au NPs were drop casted on the electrodes and capped with a glass cover slip. To measure real-time SERS signal with DEP, a 785 nm laser output from a diode source was loosely focused with a 50x objective (NA=0.75) on to the electrode pattern. The excitation power of the laser was 10 mW at the sample. Backscattered SERS signal from the sample was collected using the same objective and coupled to an Ocean-optics QE65000 Raman spectrometer through a multimode fiber. Real-time measurements were performed with 5 seconds integration time. After a few seconds of stabilization, an AC

potential of 10 Vpp at 1MHz was applied to the electrodes and measurements were recorded at every 5 seconds. The evolution of the SERS signal with time for BZT mixed with Au NPs is shown in Figure 6.12a. The lower spectrums in the plot are taken when there is no DEP force. As can be observed from this plot there is no measurable BZT peaks at this stage. The solution was maintained in this condition for a few acquisitions for stabilization. As soon as the DEP voltage is turned on, the SERS signal from BZT starts to develop and continues to increase. This indicates the growth of pearlchains of nanoparticles in the gap between the electrodes as demonstrated in the SEM images in Figure 6.10. As the process goes on, the density of pearlchains containing BZT molecules increases, showing increasing SERS signals. The SERS signal reaches a maximum and then starts to decrease with time depicting a destructive melting process of the pearlchains. It should be noted that the whole experiment lasted less than 2 minutes. Figure 4b shows the evolution of the 1069 cm^{-1} peak representing the breathing mode of BZT with time. The voltage was switched on after 30 s of initial stabilization time. There is a linear rate of increase in the SERS signal lasting for a 1 minute and 30s after which the signal starts to decrease. This decrease in SERS signal implies melting of the pearlchains thus reducing the SERS scattering cross section. A maximum signal is obtained when the quality of the nanoparticle chains is at its best. In Figure 6.12c is shown a comparison of the measured SERS signal before and after DEP. There is a 1000-fold increase in the signal after DEP. Such rapid detection of the analyte without long incubating times is one major advantage of this method.

To demonstrate the capability of this method for ultrafast biomolecular detection, adenine, one of the four basic nucleotide molecules, was used for another in-situ SERS detection. Adenine is known for its strong binding to noble metal surfaces[23,209-211] allowing easy detection under enhanced fields. In this context, it is interesting to note that the presence of DNA molecules is often detected by the intense peak of adenine due to the purine stretching at 735cm^{-1}.[210,212] In this experiment, 1mM aqueous solution of adenine was prepared from adenine powder (purchased from Sigma-Aldrich, 99.9% pure). An aliquot of 2 μL from the 1mM solution was dropped onto the substrate along with 2 μL of a Au NP solution and covered with a microscope coverslip. After few initial acquisitions, the AC potential was turned on to initiate the DEP process. In a few seconds, strong signals from DEP are observed. The 735 cm^{-1} peak depicting the adenine ring breathing vibrational mode clearly dominates the spectrum (Figure 6.12d). It is interesting to note that the SERs signal from adenine was observed within 2 minutes without requiring the long incubation times as previously reported.[26] This experiment demonstrates well the capability of this method for performing ultrafast biomolecule detection. Particularly, this capability will be very useful to detect environmental pollutants, or nuclear waste on site.

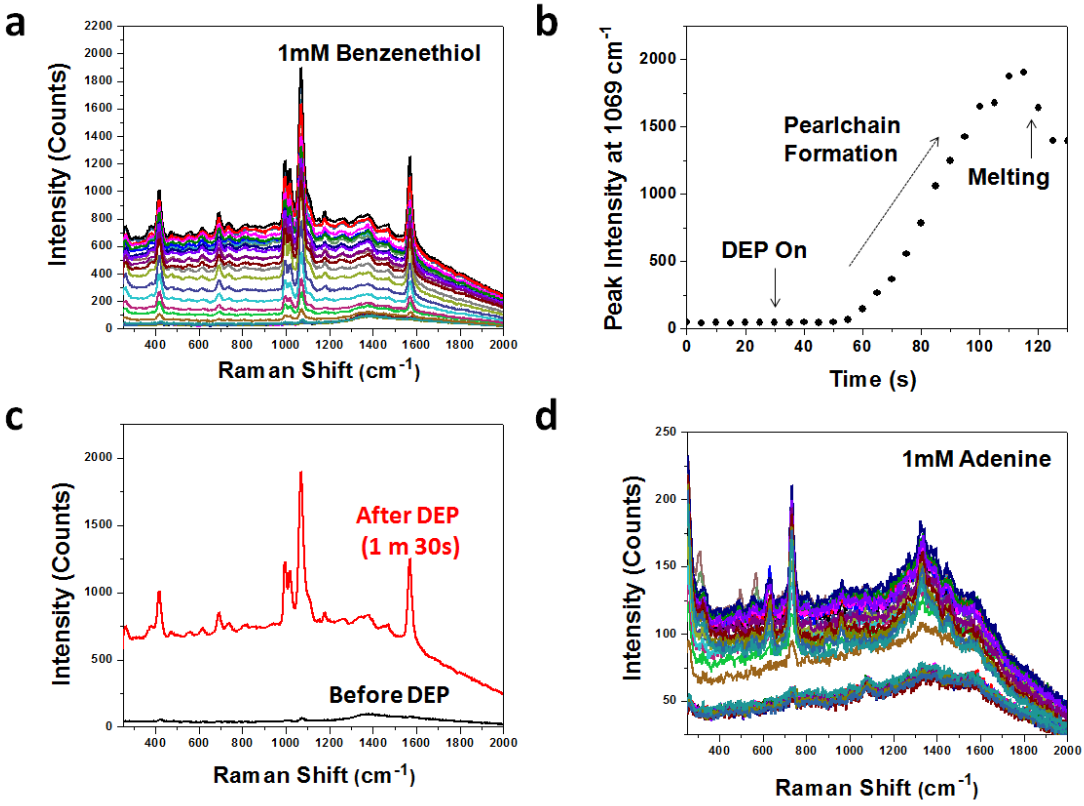

Figure 6.12 In situ SERS detection with DEP. (a) time evolution of SERS signal from BZT with DEP after mixing with Au NPs. (b) SERS intensity evolution with time for the experiment in (a). DEP is switched on after 30s of stabilization time. SERS signal increases linearly with time indicating the pearl chain formation. (c) BZT SERS signal before and after DEP. (d) SERS signal evolution from 1 uM adenine. In all the experiments, DEP was performed at 1 MHz, AC potential of 10 Vpp. A 785 nm diode laser with 10 mW power was used for Raman excitation. SERS results are courtesy of Sudir Cherukulappurath in our group.

6.3.4 Ultra-low concentration adenine detection

For real applications, the ability to detect biomolecules in a very low concentration is important. Recently there have been many reports on ultra-low concentration detection

including single-molecule SERS.[26,213,214] In order to test the detection limit of our method, SERS detections with adenine concentration ranging from *mM* to *pM* were investigated. To improve upon the diffusion process after mixing the solutions, the mixture was vortexed for 10 seconds. 2μL of the mixture was then drop casted on the electrode and capped with a glass cover slip. The same DEP process that was introduced previously was used. Negative control experiments with no Au NPs and with no adenine were done separately to ensure that the SERs signal is coming from adenine bound to Au NPs and not from any contaminations or the citrate capping of Au NPs. Figure 6.13a, b, and c show SERS signal from adenine for three different concentrations (100 μM, 100 nM and 100 pM, respectively). Even at picomolar concentrations, the distinct adenine peak of 735 cm^{-1} shift is clearly observable. This enhanced detection limit is achieved due to the adenine molecules being attracted to the Au NPs and placed in the region of SERS "hotspots". In order to take into account the spatial variation of SERS signal on the substrate, measurements were taken at several points on the sample, from which the maximum signal obtained is reported.

To evaluate the limit of detection (LOD), SERS signal at 100 fM of the adenine concentration amount of few hundred molecules in a 2 μL drop was measured. To improve the adsorption of adenine molecules to Au NPs, a 2 μL of each solution was mixed, vortexed and then left to incubate for an hour. To measure SERS from such low concentrations, the confocal Raman system (WITec alpha300R) with a 752 nm excitation laser was used. In Figure 6.13d is shown the SERS spectra from 100 fM adenine solution after DEP process. Due to the strong enhancement of Raman signals from the pearlchain,

it is possible to detect a small number of molecules without long incubation times. A comparison of SERS signals from adenine concentration of 100 µM and 100 fM is shown in Figure 6.13e. Although the signal intensity at 100 fM is weak for most frequencies, the 735 cm^{-1} signature peak of adenine can be clearly detected.

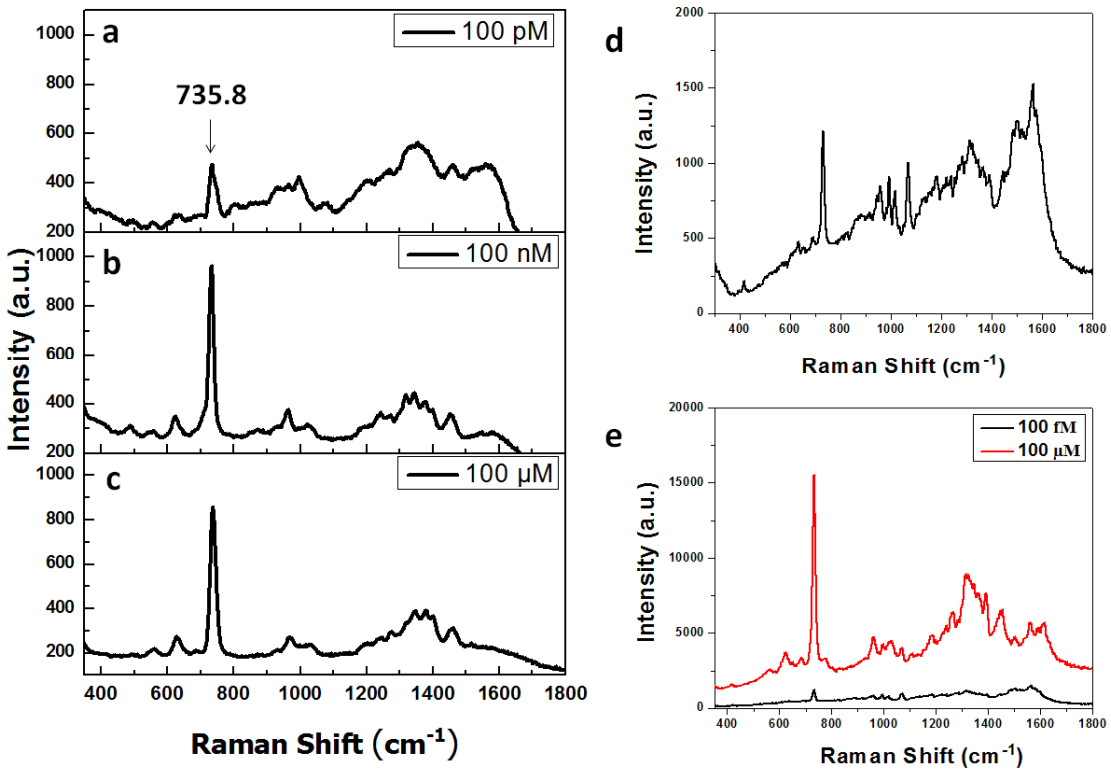

Figure 6.13 Ultralow concentration detection of adenine. (a) SERS signal from 100 µM (b) 100 nM and (c) 100 pM adenine solution after DEP. 2 µL of adenine and Au NPs were mixed and vortexed before performing DEP. (d) SERS from 100 fM adenine after DEP. SERS was measured using confocal Raman set up with a 752 nm excitation laser. (e) SERS from 100 fM and 100 uM adenine plotted together for comparison. The 735 cm^{-1} SERS peak of adenine can be observed. SERS results are courtesy of Sudir Cherukulappurath in our group.

6.4 Conclusion

In this chapter, two novel approaches for SERS substrates have been introduced. First, self-assembled nanohole arrays fabricated by NSL are evaluated at three different excitation wavelengths and are confirmed as a reproducible SERS substrate with the largest enhancement factors (EFs), 8×10^5, occurring when the plasmon resonance is nearly centered between the excitation wavelength and the Raman scattering wavelength. Besides circular nanohole arrays, elliptical hole arrays having different aspect ratios also evaluated. By introducing Ag electroless plating, giving additional surface roughness to the substrate region between the nanoholes, EFs is increased to 3×10^6.

The second novel SERS approach, to achieve rapid and ultrasensitive SERS detection, highly anisotropic dynamic nanogaps are formed using dielectrophoresis (DEP). Based on the extensive experiments, the DEP process is optimized to produce long pearlchains between the two electrodes. Due to this highly controlled, fast sub-10-nm gap fabrication process, enhanced SERS detections are observed at benzenethiol (BZT) and adenine molecules. Confocal SERS images also confirm the signal is coming from the pearlchains in the gap. Rapid SERS detection is performed by conducting in-situ measurements with a mixed solution (Au NPs and Raman active molecules). Due to the extremely confined EM energy formed by DEP process, ultra-low concentration down to 100 fM adenine is clearly detected.

CHAPTER 7

SELF-ASSEMBLED PLASMONIC ELECTRODES FOR HIGH-PERFORMANCE ORGANIC PHOTOVOLTAICS

Plasmonic photovoltaic cells aim to harness surface plasmons (SPs) for capturing light and enhancing optical absorption for efficient photoconversion. Evanescent SP waves are generated when light scatters from subwavelength metallic features, and permit the manipulation and enhancement of optical fields well below the diffraction limit.[135] Various plasmonic nanostructures have been integrated in photovoltaic cells to exploit SPs for increased optical absorption by resonantly enhancing the local field or redirecting incident light to increase the optical path length.[39,106,215-220] Plasmonic nanostructures are particularly useful in organic photovoltaic cells (OPVs) where absorption leads to the formation of excitons, which must diffuse to a dissociating heterojunction in order to contribute to the photocurrent.[221] In this chapter, thin Ag plasmonic nanohole arrays are fabricated and investigated as transparent conducting electrodes for high-performance organic photovoltaic cells. The work presented in this

chapter is the result of a collaborative effort with Professor Holmes group (with Dr. Wade Luhman) and is mainly derived from the following publication:

1. W. A. Luhman*, **S. H. Lee***, T. J. Johnson, R. J. Holmes, S. -H. Oh, *Applied Physics Letter* ,99 , 103306 (2011) * : Joint first authors

7.1 OPVs device physics and fabrication

7.1.1 General OPVs working principles

When light illuminates organic semiconductor materials, electrons in the highest occupied molecular orbit (HOMO) are excited to the lowest unoccupied molecular orbit (LUMO), generating electron-hole pairs. Unlike conventional semiconductor photovoltaic devices, organic semiconductor materials form excitons, which are strongly bound electron-hole pairs. After excitons formation, they diffuse into the organic semiconductor materials. Typically, the diffusion length of excitons in the organic semiconductor material is around 10 nm. When the excitons reach the interface between the donor and acceptor organic semiconductor materials they separate. The hole dissociates into the HOMO state in the donor material and the electron dissociates into the LUMO state in the acceptor material. If the offset between the LUMOs of the materials exceeds the binding energy, the charges will be transported to opposite electrodes and collected. Figure 7.1a shows the four-step processes for photocurrent

generation. Based on this working principle, η_{EQE}, the external quantum efficiency, represents the percentage of electrons collected per incident photon and can be expressed as the product of the efficiencies for each step.[222]

$$\eta_{EQE} = \eta_A \times \eta_{ED} \times \eta_{CT} \times \eta_{CC} \quad (7.1)$$

, where η_A, η_{ED}, η_{CT}, and η_{CC} denote the optical absorption efficiency, exciton diffusion efficiency, charge transfer efficiency, and charge collection efficiency, respectively.

Figure 7.1b shows the structure of the plasmonic organic photovoltaic (OPV) device studied in this research. The OPV consists of a 20-nm-thick electron donor layer of copper phthalocyanine (CuPc) deposited directly onto the self-assembled nanohole array anode, followed by a 40-nm-thick electron acceptor layer of C_{60}, and a 10-nm-thick layer of 2,9-dimethyl-4,7-diphenyl-1,10-phenanthroline (BCP) which serves as an exciton blocking layer.[223]After depositing organic photovoltaic materials, the structure is capped with a 50-nm-thick Al cathode.

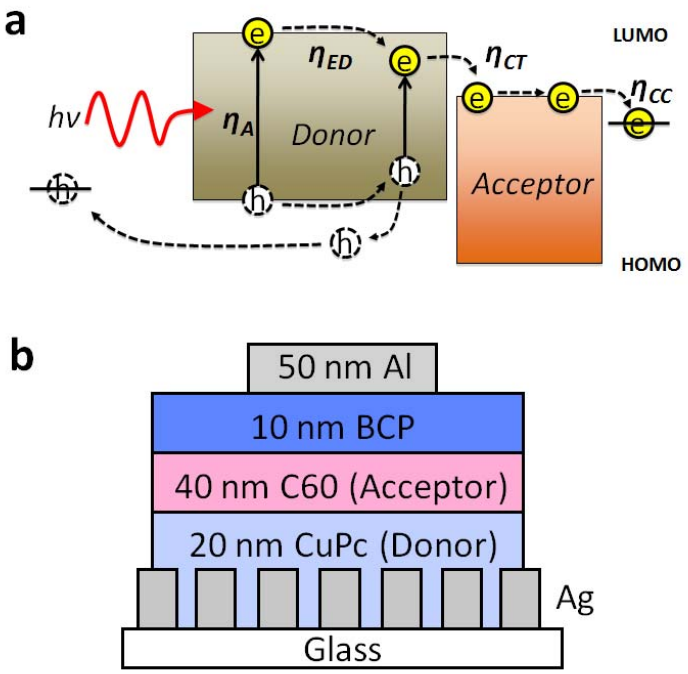

Figure 7.1 OPV device operation principle and the structure of plasmonic OPV device. (a) The four-setup process for photocurrent generation. η_A denotes the optical absorption efficiency, η_{ED} denotes exciton diffusion efficiency, η_{CT} denotes charge transfer, and η_{CC} denotes charge collection efficiency, respectively. The total external quantum efficiency η_{EQE} is the product of these efficiencies. (b) The organic photovoltaic (OPV) device structure.

7.1.2 Device fabrication

Nanopatterned Ag films were fabricated using self-assembled polystyrene nanospheres having a diameter of 400 nm. Overall, single-crystalline domains of ~10 μm × 10 μm were obtained with larger areas consisting of adjacent single-crystalline grains forming

polycrystalline films. Due to scattering from subwavelength holes, the SP propagation length within the nanohole array is short, and these polycrystalline structures exhibit spectral features that depend mainly on the periodicity of a single-crystalline domain.

Nanostructured Ag films were integrated into OPVs and performance was characterized as a function of Ag film thickness to determine the optimal electrode conditions. It was found that for Ag film thicknesses below 12 nm, the electrical performance of the patterned electrode is degraded. Figure 7.2a displays an electron micrograph of a 20-nm-thick Ag film with periodic nanohole arrays consisting of 175 nm holes having a periodicity of 400 nm. Films structured in this fashion were utilized as OPV anodes as shown in the device structure of Figure 7.2b.

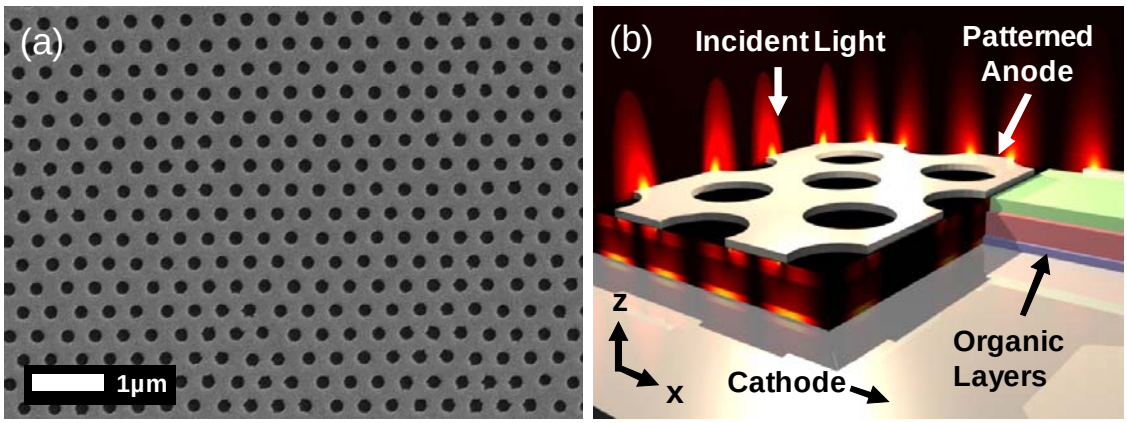

Figure 7.2 A SEM of the periodic nanohole arrays and a OPV structure. (a) A scanning electron micrograph of the periodic nanohole structure for a 20-nm-thick Ag film with holes having a periodicity of 400 nm and a diameter of 175 nm. (b) A schematic displaying the completed OPV architecture including a nanopatterned metallic anode. Figure is adapted from Luhman and Lee *et al*.,[40]

7.2 Optical characterization of nanostructured Ag films

The optical properties of the patterned Ag films was characterized by measuring broadband optical transmission of the nanostructured electrodes in the absence of the organic layers and the cathode. Normalized transmission spectra for both patterned and unpatterned Ag films having thicknesses of 12 nm, 16 nm and 20 nm are shown in Figure 7.3. The hole size increases as the Ag thickness is decreased due to the spherical shape of the nanosphere. Average holes sizes of 250 nm, 200 nm and 175 nm were measured for Ag films of 12 nm, 16 nm and 20 nm, respectively. For each thickness, the transmission spectrum of indium-tin-oxide (ITO) is also shown for comparison. The transmission of the unpatterned Ag decreases with increasing thickness. A significant increase in transmission is observed at wavelengths beyond 600 nm upon patterning with hexagonal hole arrays having a 400 nm periodicity. Theoretical studies by Rodrigo et al. have shown that the EOT peaks in square hole arrays increase in intensity and shift to longer wavelengths as the thickness of the metal film decreases to the skin depth, due to the coupling of light with short-range SPs.[224] The optical transmission spectra of the hexagonal hole arrays used in this work also show the same qualitative behavior, and exhibit a broad transmission peak in the near-infrared region. The results shown in Figure 7.3 also demonstrate that even in Ag films as thin as 12 nm, nanopatterning and the resulting plasmonic effects can further enhance the optical transmission. However, simple far-field optical transmission measurements do not capture the local field enhancement mediated by SPs. In fact, the excitation of bound SP modes in the metal film can lead to decreased optical transmission at the excitation wavelength,[8] and finite-difference time-

domain (FDTD) simulations confirm highly localized fields are present even at the transmission minimum. Therefore, while useful in characterizing the plasmonic behavior of an electrode, the transmission spectrum alone is not sufficient to determine the increased internal plasmonic field and the impact on power conversion efficiency. The latter can only be assessed from fully integrated OPVs.

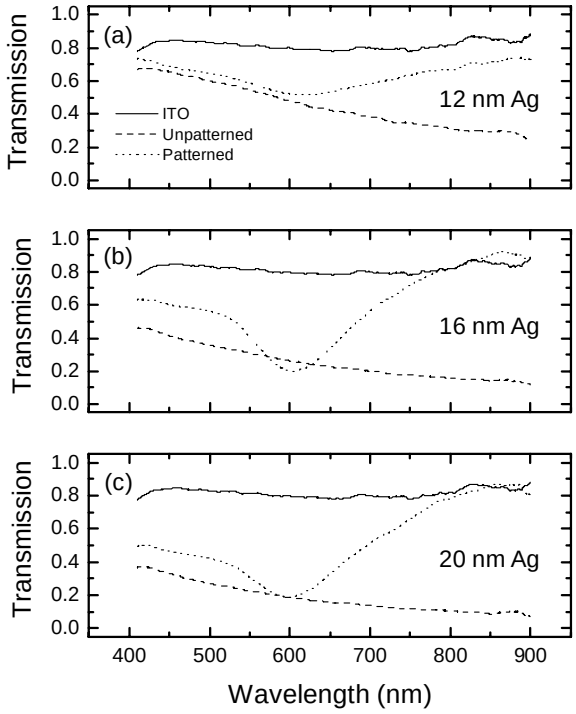

Figure 7.3 Measured transmission spectra for ITO. (a) 12 nm, (b) 16 nm and (c) 20 nm Ag films on a glass substrate. The transmission increases uniformly with decreasing Ag thickness and spectral features arise due to patterning. As noted in the text, patterned Ag films exhibit a dip and a peak in the transmission due to the excitation of surface plasmons. Figure is adapted from Luhman and Lee *et al*.,[40]

7.3 OPVs device performance

To characterize the performance of nanopatterned Ag films as plasmonic electrodes, devices were fabricated on unpatterned and patterned Ag electrodes as well as on conventional ITO substrates using the procedures discussed in the Materials and Methods section. The OPV consisted of a 20-nm-thick electron donor layer of copper phthalocyanine (CuPc) deposited directly onto the anode, followed by a 40-nm-thick electron acceptor layer of C_{60}, and a 10-nm-thick layer of 2,9-dimethyl-4,7-diphenyl-1,10-phenanthroline (BCP) which serves as an exciton blocking layer.[223] The structure is capped with a 50-nm-thick Al cathode.

Devices were characterized under AM 1.5G solar simulated illumination by measuring current density-voltage characteristics. Figure 7.4 compares data collected from devices constructed on ITO and those constructed on Ag anodes having a thickness of 12 nm. For all of the devices fabricated on Ag, the 12 nm thick anodes demonstrated the highest efficiency due to the balance of plasmonic enhancement of the optical field and increased direct transmission. The open-circuit voltage (V_{OC}) and fill factor (FF) are comparable for all three electrodes, demonstrating that the nanopatterning does not adversely affect the electrical properties of the anode (Fig. 3a). The main performance difference with patterning is in device responsivity (Fig. 3b). Devices constructed on unpatterned Ag show the lowest responsivity, reflecting the low optical transmission shown in Figure 7.3. Devices fabricated on patterned Ag show a larger responsivity than that those on ITO, even though transmission through the bare electrode is lower than that of ITO. This difference comes from the excitation of SPs along the metallic electrode. As noted

previously, measurements of the far-field transmission do not fully reflect the large local fields generated near the metal electrode that contribute to device efficiency. Consequently, the power conversion efficiency for devices fabricated on patterned Ag is larger than that measured for devices constructed on ITO, and is almost twice that obtained for devices constructed on unpatterned Ag (Fig. 3c). Device response was found to be independent of light polarization, in contrast to previous work related to OPVs containing linear metallic gratings.[216]

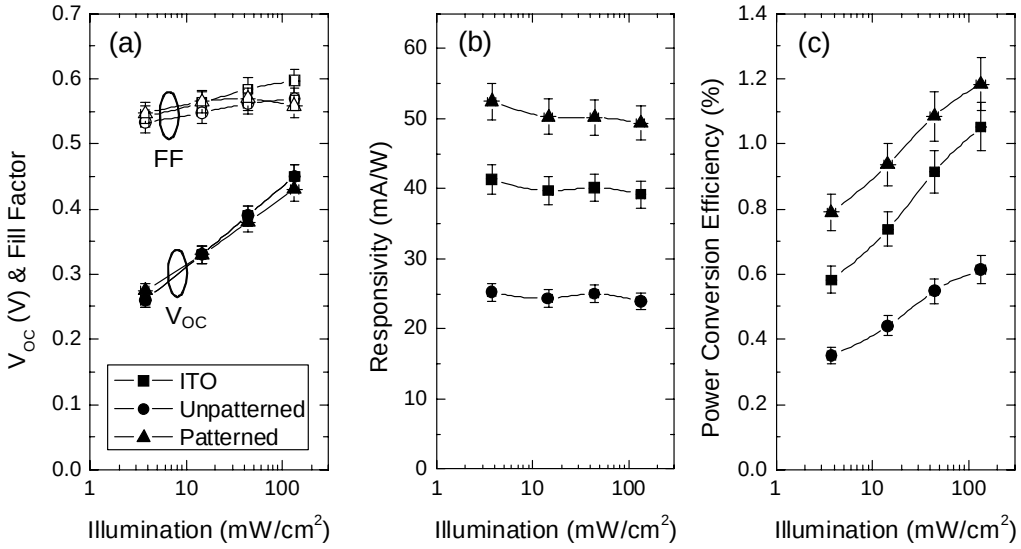

Figure 7.4 Device performance parameters under broadband AM 1.5G simulated solar illumination. (a) Comparable values for the open-circuit voltage (V_{OC}) and fill factor (FF) are obtained for all anodes, demonstrating comparable electrical performance. (b) Devices with a patterned anode show the highest responsivity due to the optical plasmonic field enhancement. (c) The increased responsivity of the patterned device leads to a higher power conversion efficiency than devices using either a conventional ITO or unpatterned Ag anode. Figure is adapted from Luhman and Lee *et al*.,[40]

Figure 7.5 shows external quantum efficiency (η_{EQE}) spectra for devices constructed on ITO as well as on patterned and unpatterned Ag films with a thickness of 12 nm. All devices show comparable η_{EQE} for wavelengths below 500 nm. The spectra begin to diverge at wavelengths greater than 500 nm due to the generation of SPs (Fig. 7.3). For wavelengths larger than 500 nm the spectral response for the patterned Ag anode device is superior to that of both the unpatterned and ITO devices. Increased response, when compared to the unpatterned device, can be expected as the patterned anode also shows a larger overall transmission in this region. However, when comparing the patterned anode device to the ITO device, which has a larger broadband transmission, this result is not obvious. This region of increased η_{EQE} also corresponds to the region of high optical absorption for the donor material CuPc. The relative increase in the spectral response of the CuPc contribution is due to the large local field enhancement generated near the patterned metal anode that is in contact with the CuPc layer.

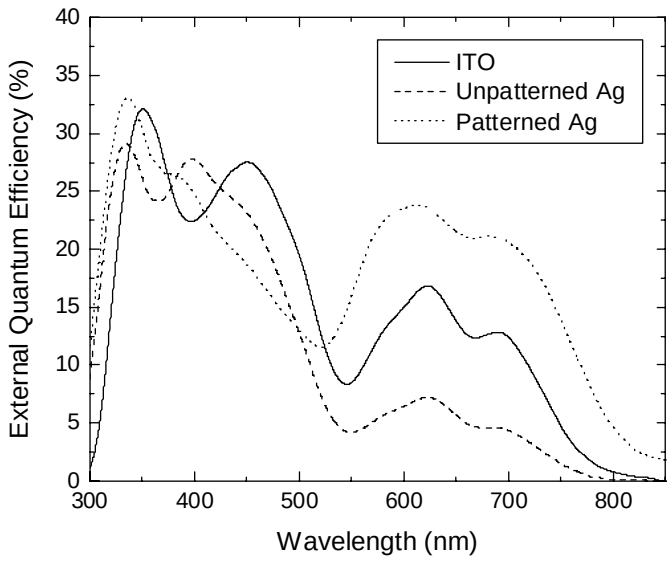

Figure 7.5 External quantum efficiency (ηEQE) for devices with anodes consisting of ITO, unpatterned Ag (12 nm) and patterned Ag (12 nm). The increase in η_{EQE} for devices with a patterned anode at wavelengths larger than 500 nm reflects the enhanced absorption in the CuPc donor arising from spectrally-broad plasmonic contributions at the anode-donor interface. Figure is adapted from Luhman and Lee *et al*.,[40]

7.4 Simulations of the electromagnetic fields

The electromagnetic field distribution of the entire device was visualized using FDTD calculations. Full 3-D FDTD calculations were performed on a unit-cell consisting of two holes with periodic boundary conditions in the x- and y-dimensions simulating an infinite hexagonal array and perfectly matched layer absorbing boundary conditions in the z-dimension. A constant grid size of 3 nm was used in the x- and y-dimensions while a non-uniform grid scaled from 5 nm in the bulk down to 1 nm in the Ag and organic layers was used in the z-dimension. Material constants for the simulations were obtained via

ellipsometry for the organic layers and from Rakic[37] for the metals and numerically fit to a Lorentz/Drude model. Figure 5 shows simulated, time-averaged cross-sectional field intensity maps at an incident wavelength of 622 nm, close to the absorption maximum of CuPc. Figure 7.6a shows a reference field map for a device which has a 12 nm unpatterned Ag anode. When the anode is patterned with 250 nm nanoholes having a periodicity of 400 nm, strong cavity resonances and higher field intensities within the organic semiconductor layers are observed (Fig. 7.6b). To help distinguish between plasmonic and non-plasmonic effects the same simulation was performed where the patterned Ag anode was replaced with a patterned Cr anode, a lossy material that does not efficiently support surface plasmons in this wavelength range. The results (Fig. 7.6c) show a slight increase in field when compared to the unpattered Ag anode, however, the strong plasmonic resonances like those in Figure 5b are not observed. Overall, these FDTD simulations confirm that subwavelength hole arrays in optically thin (12 nm) Ag films are able to produce intense local fields that can enhance the power conversion efficiency of integrated OPVs.

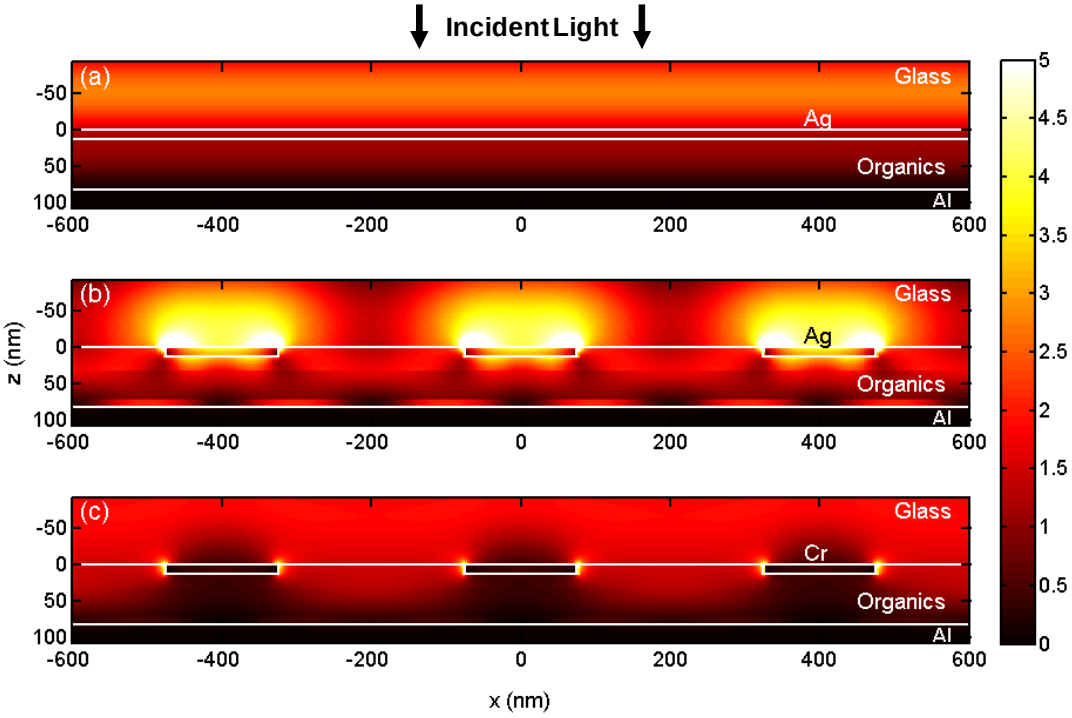

Figure 7.6 Simulated cross-sectional device field intensity maps at a wavelength of 622 nm. The anode is varied to demonstrate the difference in plasmonic enhancement for (a) 12 nm unpatterned Ag, and (b) 12 nm patterned Ag having 250 nm hexagonally close-packed holes with a periodicity of 400 nm and (c) a similarly patterned Cr anode. The difference between (a) and (b) demonstrates the presence of plasmonic contributions as patterning is introduce. A comparison of (b) and (c) displays the disparity in field enhancement between a metal that efficiently supports surface plasmons (Ag) and one that is extremely lossy (Cr). Figure is adapted from Luhman and Lee *et al.*,[40] The FDTD image is courtesy of Tim Johnson in our group.

7.5 Conclusion

In this chapter, thin patterned Ag electrodes have been fabricated by NSL and used to demonstrate OPV efficiencies that exceed those for devices constructed on a conventional ITO anode. The increase in device performance is attributed to the excitation of surface plasmons and the associated large field enhancements near the anode-donor interface that enhances absorption in the CuPc donor layer. The solution-based NSL technique allows for processing compatible with low-cost OPV fabrication techniques. This process is also highly tunable, allowing for patterned metallic films of varying hole size and periodicity. Since the NSL technique can be readily extended to massively parallel nanopatterning, it is a promising option to realize low-cost plasmonic photovoltaics using OPVs and other thin-film semiconductors.

CHAPTER 8

CONCLUSIONS

This dissertation presented new large-scale nanostructure fabrication techniques and their applications for surface plasmon resonance (SPR) biosensing and surface-enhanced Raman spectroscopy. First, to achieve high-quality, low-cost and large-area cm-scale periodic nanohole arrays, two novel approaches were considered. Nanosphere lithography (NSL) was applied for producing self-assembled nanohole arrays without any expensive photo-lithographic tools. Template stripping method was used to address the limit of self-assembly process such as large variation of resonance peak positions. After optimizing process conditions for NSL, a large defect-free areas (>30 × 30 μm^2) of noble metal nanohole arrays across a cm-sized patterning area was produced. In addition, by controlling the original nanosphere size, etching time, metal deposition thickness, and metal deposition angle, it was possible to tune the nanohole spacing, size and aspect ratio, and accordingly, the plasmonic properties. For template-stripped nanohole arrays, Si templates were fabricated by nanoimprint, followed by the RIE for anisotropic Si etching. A batch metal evaporation process completes the patterning of nanohole arrays in every

mold simultaneously. After curing with an optical epoxy, the patterned metallic films could be peeled off just prior to use to avoid unwanted contamination or oxidation. Because of the uniform Si trenches, template-stripped nanohole arrays showed extremely homogeneous sensitivity and optical properties across positions and samples. Since the master templates can be reused multiple times after a template-cleaning, this fabrication technique will benefit a lot for whom very extensive proteomics research is needed or high-resolution lithography equipment is hard to access.

For biosensing, it is highly desirable to obtain sharp resonance peaks because the spectral shift can be distinguished clearly even at the small amount of binding, increasing the dynamic range of sensor. This essential requirement can be accomplished by reducing the radiative damping of SPPs through the nanoholes or the material damping in the metals. The template stripping process provided large-scale hole-size tunability. When the nanohole size was above ~200 nm, the linewidth at visible frequencies was predominantly determined by the radiative scattering of SPPs by the large nanoholes. Below ~150 nm nanohole size, materials loss dominated the linewidth, and smooth Ag films further sharpened the EOT peaks in that regime. The measured linewidth from nanoholes immersed in water was measured to be 9.9 nm, and the simulated value was 3.8 nm. Furthermore, the measured Q-factor of the EOT peak in template-stripped nanohole arrays was as high as 71 at visible frequencies in aqueous conditions.

After acquiring large area nanohole arrays and optimizing the linewidth of the resonance peak, SPR spectral imaging combined with multichannel microfluidics was investigated. The instrument combines an imaging spectrometer, a cooled CCD camera

and a multi-channel microfluidic chip to produce high throughput full-spectral imaging and accurate quantification of receptor-ligand binding kinetics. Highly uniform optical properties, which are the prerequisite for SPR spectral imaging was acquired by the template-stripping method. Device sensitivity extracted from the multichannel SPR spectral image was highly consistent over all channels. The measured refractive index resolution was around 7.7×10^{-6} RIU level. To confirm the utility of our system, various conditions for binding kinetics of cholera toxin b subunit (CTX-b) to gangliosidemonosialic (GM1) receptors were measured in a single experiment. The dissociation constant (~sub-nM) acquired from nanohole-based multichannel SPR imaging spectroscopy matched very well with the previously reported results. LOQ defining the smallest detectable concentration was calculated to 8.4 nM, which was similar value from the minimum concentration showing the apparent spectral shift in real-time binding kinetics.

Although SPR biosensors can detect molecular interactions between analyte and target molecules, they do not provide any chemical information. On the other hand, Raman spectroscopy which detects in-elastic scattering of incident light after colliding with molecules provides molecular structures. Raman signal is extremely weak, however, this feeble in-elastic scattering can be increased drastically when the molecules are located near the subwavelength size metallic surface. Two novel approaches for surface-enhanced Raman spectroscopy (SERS) substrates were introduced in this dissertation. First, self-assembled nanohole arrays fabricated by NSL were evaluated at three different excitation wavelengths and were confirmed as a reproducible SERS substrate. Besides

circular nanohole arrays, elliptical hole arrays having different aspect ratios were also evaluated. By introducing Ag electroless plating, giving additional surface roughness to the substrate region between the nanoholes, EFs was increased to 3×10^6. The second novel SERS substrates to achieve rapid and ultrasensitive SERS detection were achieved by forming highly anisotropic dynamic nanogaps using dielectrophoresis (DEP). Confocal SERS images also confirmed the signal was coming from the pearlchains in the gap. Rapid SERS detection was performed by conducting in-situ measurements with a mixed solution of Au NPs and Raman active molecules. Due to the extremely confined EM energy at high density nanogap pearlchains formed by DEP process, ultra-low concentration down to 100 fM adenine was clearly detected.

Last chapter outlined low-cost organic photovoltaic devices fabricated by self-assembled plasmonic nanohole arrays. Thin patterned Ag electrodes were prepared by NSL and used to demonstrate OPV efficiencies that exceed those for devices constructed on a conventional ITO anode. The increase in device performance was attributed to the excitation of surface plasmons and the associated large field enhancements near the anode-donor interface that enhances absorption in the CuPc donor layer. Since the NSL technique can be readily extended to massively parallel nanopatterning, it is a promising option to realize low-cost plasmonic photovoltaics using OPVs and other thin-film semiconductors.

Bibliography

1 Langley, J. N. On the reaction of cells and of nerve-endings to certain poisons, chiefly as regards the reaction of striated muscle to nicotine and to curari. *The Journal of physiology* **33**, 374-413 (1905).

2 Ahlquist, R. P. A study of the adrenotropic receptors. *The American journal of physiology* **153**, 586-600 (1948).

3 Munos, B. Lessons from 60 years of pharmaceutical innovation. *Nature Reviews Drug Discovery* **8**, 959-968, (2009).

4 Kola, I. The state of innovation in drug development. *Clinical Pharmacology & Therapeutics* **83**, 227-230, (2008).

5 Mayer, T. U. *et al.* Small molecule inhibitor of mitotic spindle bipolarity identified in a phenotype-based screen. *Science* **286**, 971-974, (1999).

6 Lofas, S. *et al.* Bioanalysis with surface-plasmon resonance. *Sensors and Actuators B-Chemical* **5**, 79-84, (1991).

7 Jensen, K. K., Orum, H., Nielsen, P. E. & Norden, B. Kinetics for hybridization of peptide nucleic acids (PNA) with DNA and RNA studied with the BIAcore technique. *Biochemistry* **36**, 5072-5077, (1997).

8 Rutz, M. *et al.* Toll-like receptor 9 binds single-stranded CpG-DNA in a sequence- and pH-dependent manner. *European Journal of Immunology* **34**, 2541-2550, (2004).

9 Cooper, M. A., Hansson, A., Lofas, S. & Williams, D. H. A vesicle capture sensor chip for kinetic analysis of interactions with membrane-bound receptors. *Analytical Biochemistry* **277**, 196-205, (2000).

10 Myszka, D. G. Analysis of small-molecule interactions using Biacore S51 technology. *Analytical Biochemistry* **329**, 316-323, (2004).

11 Ritchie, R. H. Plasma losses by fast electrons in thin-films. *Current Contents/Engineering Technology & Applied Sciences*, 18-18 (1985).

12 Homola, J., Yee, S. S. & Gauglitz, G. Surface plasmon resonance sensors: review. *Sensors and Actuators B-Chemical* **54**, 3-15, (1999).

13 Jung, L. S., Campbell, C. T., Chinowsky, T. M., Mar, M. N. & Yee, S. S. Quantitative interpretation of the response of surface plasmon resonance sensors to adsorbed films. *Langmuir* **14**, 5636-5648, (1998).

14 BIAcore. *BIAtechnology handbook.* (BIAcore, 1998).

15 Ebbesen, T. W., Lezec, H. J., Ghaemi, H. F., Thio, T. & Wolff, P. A. Extraordinary optical transmission through sub-wavelength hole arrays. *Nature* **391**, 667-669, (1998).

16 Jeanmaire, D. L. & Van Duyne, R. P. Surface raman spectroelectrochemistry: Part I. Heterocyclic, aromatic, and aliphatic amines adsorbed on the anodized silver electrode. *Journal of Electroanalytical Chemistry* **84**, 1-20 (1977).

17 Albrecht, M. G. & Creighton, J. A. Anomalously intense Raman-spectra of pyridine at a silver electrode. *Journal of the American Chemical Society* **99**, 5215-5217, (1977).

18 Nie, S. M. & Emery, S. R. Probing single molecules and single nanoparticles by surface-enhanced Raman scattering. *Science* **275**, 1102-1106, (1997).

19 Lyandres, O. *et al.* Real-time glucose sensing by surface-enhanced Raman spectroscopy in bovine plasma facilitated by a mixed decanethiol/mercaptohexanol partition layer. *Analytical Chemistry* **77**, 6134-6139, (2005).

20 Huang, G. G., Hossain, M. K., Han, X. X. & Ozaki, Y. A novel reversed reporting agent method for surface-enhanced Raman scattering; highly sensitive detection of glutathione in aqueous solutions. *Analyst* **134**, 2468-2474, (2009).

21 Deckert-Gaudig, T., Bailo, E. & Deckert, V. Tip-enhanced Raman scattering (TERS) of oxidised glutathione on an ultraflat gold nanoplate. *Physical Chemistry Chemical Physics* **11**, 7360-7362, (2009).

22 Singhal, R. *et al.* Small diameter carbon nanopipettes. *Nanotechnology* **21**, 015304 (2010).

23 Barhoumi, A., Zhang, D., Tam, F. & Halas, N. J. Surface-enhanced Raman spectroscopy of DNA. *Journal of the American Chemical Society* **130**, 5523-5529, (2008).

24 Domke, K., Zhang, D. & Pettinger, B. Tip-enhanced Raman spectra of picomole quantities of DNA nucleobases at Au(111). *Journal of the American Chemical Society*, 6708-6709, (2007).

25 Green, M., Liu, F. M., Cohen, L., Kollensperger, P. & Cass, T. SERS platforms for high density DNA arrays. *Faraday Discussions* **132**, 269-280, (2006).

26 Cho, H. S., Lee, B., Liu, G. L., Agarwal, A. & Lee, L. P. Label-free and highly sensitive biomolecular detection using SERS and electrokinetic preconcentration. *Lab on a Chip* **9**, 3360-3363, (2009).

27 Han, X., Zhao, B. & Ozaki, Y. Surface-enhanced Raman scattering for protein detection. *Analytical and Bioanalytical Chemistry*, 1719-1727, (2009).

28 Podstawka, E., Ozaki, Y. & Proniewicz, L. M. Part I: Surface-enhanced Raman spectroscopy investigation of amino acids and their homodipeptides adsorbed on colloidal silver. *Applied Spectroscopy* **58**, 570-580 (2004).

29 Drude, P. Zur elektronentheorie der metalle. Annalen der Physik, **306**, 566 (1900).

30 Drude, P. Zur elektronentheorie der metalle; ii. teil. galvanomagnetische und thermomagnetische effecte. Annalen der Physik, **308**, 369 (1900).

31 Raether, H. *Surface plasmons on smooth and rough surfaces and on gratings*. (Springer-Verlag, 1986).

32 Maier, S. A. *Plasmonics: Fundamentals and applications*. (Springer, 2007).

33 Kretschmann, E. Die Bestimmung optischer Konstanten von Metall.en durch Anregung von Oberflächenplasmaschwingungen. *Z. Phys.* **241**, 313-324 (1971).

34 Bethe, H. A. Theory of diffraction by small holes. *Phys. Rev*. **66**, 163–182 (1944).

35 Brolo, A. G., Gordon, R., Leathem, B. & Kavanagh, K. L. Surface plasmon sensor based on the enhanced light transmission through arrays of nanoholes in gold films. *Langmuir* **20**, 4813-4815, (2004).

36 Bozhevolnyi, S. I., Volkov, V. S., Devaux, E., Laluet, J. Y. & Ebbesen, T. W. Channel plasmon subwavelength waveguide components including interferometers and ring resonators. *Nature* **440**, 508-511, (2006).

37 Challener, W. A. *et al.* Heat-assisted magnetic recording by a near-field transducer with efficient optical energy transfer (vol 3, pg 220, 2009). *Nature Photonics* **3**, 303-303, (2009).

38 Mansuripur, M. *et al.* Plasmonic nano-structures for optical data storage. *Optics Express* **17**, 14001-14014, (2009).

39 Atwater, H. A. & Polman, A. Plasmonics for improved photovoltaic devices. *Nature Materials* **9**, 205-213, (2010).

40 Luhman, W. A., Lee, S. H., Johnson, T. W., Holmes, R. J. & Oh, S.-H. Self-assembled plasmonic electrodes for high-performance organic photovoltaic cells. *Applied Physics Letters* **99**,103306 (2011).

41 Polman, A. & Atwater, H. A. Photonic design principles for ultrahigh-efficiency photovoltaics. *Nature Materials* **11**, 174-177, (2012).

42 Eggimann, W. H., Collin, R. E., Electromagnetic diffraction by a planar array of circular disks. IRE Trans. Microw. Theory Tech. **10**, 528-535, (1962)

43 Chen, C. C. Diffraction of electromagnetic waves by a conducting screen perforated periodically with circular holes. IEEE Trans. Microw. Theory Tech. **19**, 475-481,(1971)

44 McPhedran, R. C., Derrick, G. H., Botten, L. C. Electromagnetic Theory of Gratings. Springer-Verlag, Berlin, 227-276, (1980)

45 Dawes, D. H., McPhedran, R. C. Whitbourn, L. B. Thin capacitive meshes on a dielectric boundary – theory and experiment. Appl. Opt. 28, 3498-3510, (1989)

46 Moreno, L. *et al.* Theory of extraordinary optical transmission through subwavelength hole arrays. *Physical Review Letters* **86**, 1114-1117, (2001).

47 Krishnan, A. *et al.* Evanescently coupled resonance in surface plasmon enhanced transmission. *Optics Communications* **200**, 1-7, (2001).

48 Sarrazin, M., Vigneron, J. P. & Vigoureux, J. M. Role of Wood anomalies in optical properties of thin metallic films with a bidimensional array of subwavelength holes. *Physical Review B* **67**, (2003).

49 Muller, R., Malyarchuk, V. & Lienau, C. Three-dimensional theory on light-induced near-field dynamics in a metal film with a periodic array of nanoholes. *Physical Review B* **68**, (2003).

50 Barnes, W. L., Murray, W. A., Dintinger, J., Devaux, E. & Ebbesen, T. W. Surface plasmon polaritons and their role in the enhanced transmission of light through periodic arrays of subwavelength holes in a metal film. *Physical Review Letters* **92**, (2004).

51 Genet, C., van Exter, M. P. & Woerdman, J. P. Fano-type interpretation of red shifts and red tails in hole array transmission spectra. *Optics Communications* **225**, 331-336, (2003).

52 Chang, S. H., Gray, S. K. & Schatz, G. C. Surface plasmon generation and light transmission by isolated nanoholes and arrays of nanoholes in thin metal films. *Optics Express* **13**, 3150-3165, (2005).

53 Born, M., Wolf, E. *Principles of Optics: ElectromagneticTheory of Propagation, Interference and Diffraction of Light.(* Cambridge University Press, 1999).

54 Jackson, J. D. *Classical Electrodynamics,* (Wiley, New York, 1999).

55 O'shannessy, D. J., Brighamburke, M., Soneson, K. K., Hensley, P. & Brooks, I. Determination of rate and equilibrium binding constants for macromolecular interactions using surface plasmon resonance: use of nonlinear least squares analysis methods. *Anal. Biochem.* **212,** 457-468 (1993).

56 Gao, H., Henzie, J. & Odom, T. W. Direct Evidence for Surface Plasmon-Mediated Enhanced Light Transmission through Metallic Nanohole Arrays. *Nano Lett.* **6**, 2104-2108 (2006).

57 Altewischer, E. *et al.* Polarization tomography of metallic nanohole arrays. *Opt. Lett.* **30**, 90-92 (2005).

58 Brian, B., Sepulveda, B., Alaverdyan, Y., Lechuga, L. M. & Kaell, M. Sensitivity enhancement of nanoplasmonic sensors in low refractive index substrates. *Opt. Express* **17**, 2015-2023 (2009).

59 Kwak, E.-S. *et al.* Surface Plasmon Standing Waves in Large-Area Subwavelength Hole Arrays. *Nano Letters* **5**, 1963-1967, (2005).

60 Stewart, M. E. *et al.* Quantitative multispectral biosensing and 1D imaging using quasi-3D plasmonic crystals. *Proceedings of the National Academy of Sciences of the United States of America* **103**, 17143-17148, (2006).

61 Chen, J. *et al.* Gold nanohole arrays for biochemical sensing fabricated by soft UV nanoimprint lithography. *MICROELECTRONIC ENGINEERING* **86**, 632-635 (2009).

62 Masuda, H. & Fukuda, K. Ordered metal nanohole arrays made by a two-step replication of honeycomb structures of anodic alumina. *Science (Washington, D. C.)* **268**, 1466-1468 (1995).

63 Deckman, H. W. & Dunsmuir, J. H. Natural lithography. *Applied Physics Letters* **41**, 377-379 (1982).

64 Haynes, C. L. & Van Duyne, R. P. Nanosphere lithography: A versatile nanofabrication tool for studies of size-dependent nanoparticle optics. *Journal of Physical Chemistry B* **105**, 5599-5611, (2001).

65 Lee, S., Bantz, K., Lindquist, N., Oh, S. & Haynes, C. Self-Assembled Plasmonic Nanohole Arrays. *Langmuir*, 13685-13693, (2009).

66 Wang, X. D., Summers, C. J. & Wang, Z. L. Large-scale hexagonal-patterned growth of aligned ZnO nanorods for nano-optoelectronics and nanosensor arrays. *Nano Letters* **4**, 423-426, (2004).

67 Jiang, P. & McFarland, M. J. Wafer-Scale Periodic Nanohole Arrays Templated from Two-Dimensional Nonclose-Packed Colloidal Crystals. *J. Am. Chem. Soc.* **127**, 3710-3711 (2005).

68 Mihi, A., Ocana, M. & Miguez, H. Oriented colloidal-crystal thin films by spin-coating microspheres dispersed in volatile media. *Advanced Materials* **18**, 2244-2249, (2006).

69 Denkov, N. D. *et al.* 2-Dimensional crystallization. *Nature* **361**, 26-26 (1993).

70 Dimitrov, A. S. & Nagayama, K. Continuous convective assembling of fine particles into two-dimensional arrays on solid surfaces. *Langmuir* **12**, 1303-1311 (1996).

71 Fulda, K. U. & Tieke, B. Langmuir films of monodisperse 0.5μm spherical polymer with a hydrophobic core and a hydrophilic shell. *Advanced Materials* **6**, 288-290 (1994).

72 Wang, D. Y. & Mohwald, H. Rapid fabrication of binary colloidal crystals by stepwise spin-coating. *Advanced Materials* **16**, 244-247, (2004).

73 Xia, Y. N. & Whitesides, G. M. Soft lithography. *Annual Review of Materials Science* **28**, 153-184 (1998).

74 Koerkamp, K. J. K., Enoch, S., Segerink, F. B., van Hulst, N. F. & Kuipers, L. Strong influence of hole shape on extraordinary transmission through periodic arrays of subwavelength holes. *Physical Review Letters* **92**, (2004).

75 Gordon, R. *et al.* Strong polarization in the optical transmission through elliptical nanohole arrays. *Physical Review Letters* **92**, (2004).

76 van der Molen, K. L. *et al.* Role of shape and localized resonances in extraordinary transmission through periodic arrays of subwavelength holes: Experiment and theory. *Physical Review B* **72**, (2005).

77 Haynes, C. L. & Van Duyne, R. P. Plasmon-sampled surface-enhanced Raman excitation spectroscopy. *Journal of Physical Chemistry B* **107**, 7426-7433, (2003).

78 Kosiorek, A., Kandulski, W., Chudzinski, P., Kempa, K. & Giersig, M. Shadow nanosphere lithography: Simulation and experiment. *Nano Letters* **4**, 1359-1363, (2004).

79 Lu, Y., Liu, G. L., Kim, J., Mejia, Y. X. & Lee, L. P. Nanophotonic crescent moon structures with sharp edge for ultrasensitive biomolecular detection by local electromagnetic field enhancement effect. *Nano Letters* **5**, 119-124, (2005).

80 Choi, D. G. *et al.* Multifaceted and nanobored particle arrays sculpted using colloidal lithography. *Advanced Functional Materials* **16**, 33-40, (2006).

81 Thio, T., Ghaemi, H. F., Lezec, H. J., Wolff, P. A. & Ebbesen, T. W. Surface-plasmon-enhanced transmission through hole arrays in Cr films. *Journal of the Optical Society of America B-Optical Physics* **16**, 1743-1748, (1999).

82 Nagpal, P., Lindquist, N. C., Oh, S. H. & Norris, D. J. Ultrasmooth Patterned Metals for Plasmonics and Metamaterials. *Science* **325**, 594-597, (2009).

83 Plumer, J. D. Silicon VLSI Technology: Fundamentals, Practice, and Modeling. (Prentice Hall Electronics and VLSI series, 2000)

84 Im, H. *et al.* Template-Stripped Smooth Ag Nanohole Arrays with Silica Shells for Surface Plasmon Resonance Biosensing. *Acs Nano* **5**, 6244-6253, (2011).

85 Whitney, A. V. *et al.* Localized surface plasmon resonance nanosensor: A high-resolution distance-dependence study using atomic layer deposition. *Journal of Physical Chemistry B* **109**, 20522-20528, (2005).

86 Im, H., Lindquist, N. C., Lesuffleur, A. & Oh, S. H. Atomic Layer Deposition of Dielectric Overlayers for Enhancing the Optical Properties and Chemical Stability of Plasmonic Nanoholes. *ACS Nano* **4**, 947-954 (2010).

87 Love, J. C., Estroff, L. A., Kriebel, J. K., Nuzzo, R. G. & Whitesides, G. M. Self-assembled monolayers of thiolates on metals as a form of nanotechnology. *Chemical Reviews* **105**, 1103-1169, (2005).

88 Zhang, X. Y., Zhao, J., Whitney, A. V., Elam, J. W. & Van Duyne, R. P. Ultrastable substrates for surface-enhanced Raman spectroscopy: Al2O3 overlayers fabricated by atomic layer deposition yield improved anthrax biomarker detection. *Journal of the American Chemical Society* **128**, 10304-10309, (2006).

89 Gao, H., Henzie, J., Lee, M. H. & Odom, T. W. Screening plasmonic materials using pyramidal gratings. *Proceedings of the National Academy of Sciences of the United States of America* **105**, 20146-20151, (2008).

90 Hausmann, D., Becker, J., Wang, S. L. & Gordon, R. G. Rapid vapor deposition of highly conformal silica nanolaminates. *Science* **298**, 402-406, (2002).

91 Danelon, C., Perez, J. B., Santschi, C., Brugger, J. & Vogel, H. Cell membranes suspended across nanoaperture arrays. *Langmuir* **22**, 22-25, (2006).

92 Mager, M. D. & Melosh, N. A. Lipid bilayer deposition and patterning via air bubble collapse. *Langmuir* **23**, 9369-9377, (2007).

93 Voros, J. The density and refractive index of adsorbing protein layers. *Biophysical Journal* **87**, 553-561, (2004).

94 Vockenroth, I. K., Atanasova, P. P., Jenkins, A. T. A. & Koeper, I. Incorporation of alpha-hemolysin in different tethered bilayer lipid membrane architectures. *Langmuir* **24**, 496-502, (2008).

95 Castellana, E. T. & Cremer, P. S. Solid supported lipid bilayers: From biophysical studies to sensor design. *Surface Science Reports* **61**, 429-444, (2006).

96 Brian, A. A. & McConnell, H. M. Allogeneic stimulation of cyto-toxic t-cells by supported planar membranes. *Proc. Natl. Acad. Sci. U.S.A.* **81**, 6159-6163 (1984).

97 Tamm, L. K. & McConnell, H. M. SUPPORTED PHOSPHOLIPID-BILAYERS. *Biophysical Journal* **47**, 105-113 (1985).

98 Cremer, P. S. & Boxer, S. G. Formation and spreading of lipid bilayers on planar glass supports. *Journal of Physical Chemistry B* **103**, 2554-2559, (1999).

99 Keller, C. A., Glasmastar, K., Zhdanov, V. P. & Kasemo, B. Formation of supported membranes from vesicles. *Physical Review Letters* **84**, 5443-5446, (2000).

100 Jonsson, P., Jonsson, M. P. & Hook, F. Sealing of Submicrometer Wells by a Shear-Driven Lipid Bilayer. *Nano Letters* **10**, 1900-1906, (2010).

101 Yang, T. L., Jung, S. Y., Mao, H. B. & Cremer, P. S. Fabrication of phospholipid bilayer-coated microchannels for on-chip immunoassays. *Analytical Chemistry* **73**, 165-169, (2001).

102 Genet, C. & Ebbesen, T. W. Light in tiny holes. *Nature* **445**, 39-46, (2007).

103 Garcia-Vidal, F. J., Martin-Moreno, L., Ebbesen, T. W. & Kuipers, L. Light passing through subwavelength apertures. *Reviews of Modern Physics* **82**, 729-787, (2010).

104 Tetz, K. A., Pang, L. & Fainman, Y. High-resolution surface plasmon resonance sensor based on linewidth-optimized nanohole array transmittance. *Optics Letters* **31**, 1528-1530, (2006).

105 Henzie, J., Lee, M. H. & Odom, T. W. Multiscale patterning of plasmonic metamaterials. *Nature Nanotechnology* **2**, 549-554, (2007).

106 Menezes, J. W., Ferreira, J., Santos, M. J. L., Cescato, L. & Brolo, A. G. Large-Area Fabrication of Periodic Arrays of Nanoholes in Metal Films and Their

Application in Biosensing and Plasmonic-Enhanced Photovoltaics. *Advanced Functional Materials* **20**, 3918-3924, (2010).

107 Masson, J.-F., Murray-Methot, M.-P. & Live, L. S. Nanohole arrays in chemical analysis: manufacturing methods and applications. *Analyst* **135**, 1483-1489, (2010).

108 de Abajo, F. J. G. Colloquium: Light scattering by particle and hole arrays. *Reviews of Modern Physics* **79**, 1267-1290, (2007).

109 Luk'yanchuk, B. *et al.* The Fano resonance in plasmonic nanostructures and metamaterials. *Nature Materials* **9**, 707-715, (2010).

110 Palik, E. D. Handbook of Optical-constants. *Journal of the Optical Society of America a-Optics Image Science and Vision* **1**, 1297-1297 (1984).

111 Park, J. H., Nagpal, P., Oh, S.-H. & Norris, D. J. Improved dielectric functions in metallic films obtained via template stripping. *Applied Physics Letters* **100**,(2012).

112 van der Molen, K. L., Segerink, F. B., van Hulst, N. F. & Kuipers, L. Influence of hole size on the extraordinary transmission through subwavelength hole arrays. *Applied Physics Letters* **85**, 4316-4318, (2004).

113 McMahon, J. M., Henzie, J., Odom, T. W., Schatz, G. C. & Gray, S. K. Tailoring the sensing capabilities of nanohole arrays in gold films with Rayleigh anomaly-surface plasmon polaritons. *Optics Express* **15**, 18119-18129, (2007).

114 Yanik, A. A. *et al.* Seeing protein monolayers with naked eye through plasmonic Fano resonances. *Proceedings of the National Academy of Sciences of the United States of America* **108**, 11784-11789, (2011).

115 Braun, J., Gompf, B., Kobiela, G. & Dressel, M. How Holes Can Obscure the View: Suppressed Transmission through an Ultrathin Metal Film by a Subwavelength Hole Array. *Physical Review Letters* **103**,(2009).

116 Gao, H. W. *et al.* Using the Angle-Dependent Resonances of Molded Plasmonic Crystals To Improve the Sensitivities of Biosensors. *Nano Letters* **10**, 2549-2554, (2010).

117 Lesuffleur, A., Im, H., Lindquist, N. C., Lim, K. S. & Oh, S. H. Laser-illuminated nanohole arrays for multiplex plasmonic microarray sensing. *Optics Express* **16**, 219-224 (2008).

118 Yang, J.-C., Ji, J., Hogle, J. M. & Larson, D. N. Metallic nanohole arrays on fluoropolymer substrates as small label-free real-time bioprobes. *Nano Letters* **8**, 2718-2724, (2008).

119 Lindquist, N. C., Lesuffleur, A., Im, H. & Oh, S. H. Sub-micron resolution surface plasmon resonance imaging enabled by nanohole arrays with surrounding Bragg mirrors for enhanced sensitivity and isolation. *Lab on a Chip* **9**, 382-387, (2009).

120 Escobedo, C. *et al.* Integrated nanohole array surface plasmon resonance sensing device using a dual-wavelength source. *Journal of Micromechanics and Microengineering* **21**,(2011).

121 Chang, T.-Y. *et al.* Large-scale plasmonic microarrays for label-free high-throughput screening. *Lab on a Chip* **11**, 3596-3602, (2011).

122 Brolo, A. G., Gordon, R., Kavanagh, K. & Sinton, D. The development of surface-plasmon-based sensors using arrays of sub-wavelength holes. *Proc. SPIE-Int. Soc. Opt. Eng.* **6002**, (2005).

123 Lakowicz, J. R. Radiative decay engineering 5: metal-enhanced fluorescence and plasmon emission. *Analytical Biochemistry* **337**, 171-194, (2005).

124 Yanik, A. A., Huang, M., Artar, A., Chang, T.-Y. & Altug, H. Integrated nanoplasmonic-nanofluidic biosensors with targeted delivery of analytes. *Applied Physics Letters* **96**, (2010).

125 Hutchison, J. A., O'Carroll, D. M., Schwartz, T., Genet, C. & Ebbesen, T. W. Absorption-Induced Transparency. *Angewandte Chemie-International Edition* **50**, 2085-2089, (2011).

126 Ramachandran, N., Larson, D. N., Stark, P. R. H., Hainsworth, E. & LaBaer, J. Emerging tools for real-time label-free detection of interactions on functional protein microarrays. *Febs Journal* **272**, 5412-5425, (2005).

127 Wang, D. G. *et al.* Large-scale identification, mapping, and genotyping of single-nucleotide polymorphisms in the human genome. *Science* **280**, 1077-1082, (1998).

128 Brown, P. O. & Botstein, D. Exploring the new world of the genome with DNA microarrays. *Nature Genetics* **21**, 33-37, (1999).

129 MacBeath, G. & Schreiber, S. L. Printing proteins as microarrays for high-throughput function determination. *Science* **289**, 1760-1763 (2000).

130 Mitchell, P. A perspective on protein microarrays. *Nature Biotechnology* **20**, 225-229, (2002).

131 LaBaer, J. & Ramachandran, N. Protein microarrays as tools for functional proteomics. *Current Opinion in Chemical Biology* **9**, 14-19, (2005).

132 Pollard, H. B. *et al.* Protein microarray platforms for clinical proteomics. *Proteomics Clinical Applications* **1**, 934-952, (2007).

133 Chen, Z. *et al.* Protein microarrays with carbon nanotubes as multicolor Raman labels. *Nature Biotechnology* **26**, 1285-1292, (2008).

134 Srivastava, S. & LaBaer, J. Nanotubes light up protein arrays. *Nature Biotechnology* **26**, 1244-1246, (2008).

135 Barnes, W. L., Dereux, A. & Ebbesen, T. W. Surface plasmon subwavelength optics. *Nature* **424**, 824-830, (2003).

136 Liedberg, B., Nylander, C. & Lundstrom, I. Biosensing with surface-plasmon resonance - How it all started. *Biosensors & Bioelectronics* **10**, R1-R9, (1995).

137 Mrksich, M., Sigal, G. B. & Whitesides, G. M. Surface-plasmon resonance permits in-situ measurement of protein adsorption on self-assembled monolayers of alkanethiolates on gold. *Langmuir* **11**, 4383-4385, (1995).

138 Cooper, M. A. Optical biosensors in drug discovery. *Nature Reviews Drug Discovery* **1**, 515-528, (2002).

139 Homola, J. Surface plasmon resonance sensors for detection of chemical and biological species. *Chemical Reviews* **108**, 462-493, (2008).

140 Rothenhausler, B. & Knoll, W. Surface-plasmon microscopy. *Nature* **332**, 615-617, (1988).

141 Yeatman, E. & Ash, E. A. Surface-plasmon microscopy. *Electronics Letters* **23**, 1091-1092, (1987).

142 Brockman, J. M., Nelson, B. P. & Corn, R. M. Surface plasmon resonance imaging measurements of ultrathin organic films. *Annual Review of Physical Chemistry* **51**, 41-63, (2000).

143 Smith, E. A. & Corn, R. M. Surface plasmon resonance imaging as a tool to monitor biomolecular interactions in an array based format. *Applied Spectroscopy* **57**, 320A-332A (2003).

144 Shumaker-Parry, J. S., Aebersold, R. & Campbell, C. T. Parallel, quantitative measurement of protein binding to a 120-element double-stranded DNA array in real time using surface plasmon resonance microscopy. *Analytical Chemistry* **76**, 2071-2082, (2004).

145 Luo, Y., Yu, F. & Zare, R. N. Microfluidic device for immunoassays based on surface plasmon resonance imaging. *Lab on a Chip* **8**, 694-700, (2008).

146 Ouellet, E. *et al.* Parallel microfluidic surface plasmon resonance imaging arrays. *Lab on a Chip* **10**, 581-588, (2010).

147 Natarajan, S. *et al.* Continuous-flow microfluidic printing of proteins for array-based applications including surface plasmon resonance imaging. *Analytical Biochemistry* **373**, 141-146, (2008).

148 Rich, R. L. *et al.* Extracting kinetic rate constants from surface plasmon resonance array systems. *Analytical Biochemistry* **373**, 112-120, (2008).

149 Johnsson, B., Lofas, S. & Lindquist, G. Immobilization of proteins to a carboxymethyldextran-modified gold surface for biospecific interaction analysis in surface-plasmon resonance sensors. *Analytical Biochemistry* **198**, 268-277, (1991).

150 Im, H., Lesuffleur, A., Lindquist, N. C. & Oh, S.-H. Plasmonic Nanoholes in a Multichannel Microarray Format for Parallel Kinetic Assays and Differential Sensing. *Analytical Chemistry* **81**, 2854-2859, (2009).

151 Dahlin, A. B., Tegenfeldt, J. O. & Hook, F. Improving the instrumental resolution of sensors based on localized surface plasmon resonance. *Analytical Chemistry* **78**, 4416-4423 (2006).

152 Im, H., Sutherland, J. N., Maynard, J. A. & Oh, S.-H. Nanohole-Based Surface Plasmon Resonance Instruments with Improved Spectral Resolution Quantify a Broad Range of Antibody-Ligand Binding Kinetics. *Analytical Chemistry* **84**, (2012).

153 Chinowsky, T. M., Mactutis, T., Fu, E. & Yager, P. Optical and electronic design for a high-performance surface plasmon resonance imager in *Proceedings of SPIE* **5261**, 173-182 (2004).

154 Fukuta, S., Magnani, J. L., Twiddy, E. M., Holmes, R. K. & Ginsburg, V. Comparison of the carbohydrate-binding specificities of cholera-toxin and escherichia-coli heat-labile enterotoxins LTH-I, LT-IIA, and LT-IIB. *Infection and Immunity* **56**, 1748-1753 (1988).

155 Picking, W. L., Moon, H., Wu, H. & Picking, W. D. Fluorescence analysis of the interaction between ganglioside GM_1-containing phophlipids-vesicle and the B-subunit of cholera-toxin. *Biochimica Et Biophysica Acta-Protein Structure and Molecular Enzymology* **1247**, 65-73, (1995).

156 MacKenzie, C. R., Hirama, T., Lee, K. K., Altman, E. & Young, N. M. Quantitative analysis of bacterial toxin affinity and specificity for glycolipid receptors by surface plasmon resonance. *Journal of Biological Chemistry* **272**, 5533-5538 (1997).

157 Cai, X. E. & Yang, J. The binding potential between the cholera toxin B-oligomer and its receptor. *Biochemistry* **42**, 4028-4034, (2003).

158 Schon, A. & Freire, E. Thermodynamics of intersubunit interactions in cholera-toxin upon binding to the oligosaccharide portion of its cell-surface receptor, ganglioside-gm1. *Biochemistry* **28**, 5019-5024 (1989).

159 Merritt, E. A. *et al.* Crystal-structure of cholera-toxin B-pentamer bound to receptor GM_1 pentasaccharide. *Protein Science* **3**, 166-175 (1994).

160 Keller, C. A. & Kasemo, B. Surface specific kinetics of lipid vesicle adsorption measured with a quartz crystal microbalance. *Biophysical Journal* **75**, 1397-1402 (1998).

161 Krishnamoorthy, G., Beusink, J. B. & Schasfoort, R. B. M. High-throughput surface plasmon resonance imaging-based biomolecular kinetic screening analysis. *Analytical Methods* **2**, 1020-1025, (2010).

162 Kuziemko, G. M., Stroh, M. & Stevens, R. C. Cholera toxin binding affinity and specificity for gangliosides determined by surface plasmon resonance. *Biochemistry* **35**, 6375-6384, (1996).

163 Shi, J. *et al.* GM_1 clustering inhibits cholera toxin binding in supported phospholipid membranes. *Journal of the American Chemical Society* **129**, 5954-5961, (2007).

164 Zhang, X. Y., Young, M. A., Lyandres, O. & Van Duyne, R. P. Rapid detection of an anthrax biomarker by surface-enhanced Raman spectroscopy. *Journal of the American Chemical Society* **127**, 4484-4489, (2005).

165 Yea, K. *et al.* Ultra-sensitive trace analysis of cyanide water pollutant in a PDMS microfluidic channel using surface-enhanced Raman spectroscopy. *Analyst* **130**, 1009-1011, (2005).

166 Zielinski, O. *et al.* Detecting marine hazardous substances and organisms: sensors for pollutants, toxins, and pathogens. *Ocean Science* **5**, 329-349 (2009).

167 Bantz, K. C. & Haynes, C. L. Surface-enhanced Raman scattering detection and discrimination of polychlorinated biphenyls. *Vibrational Spectroscopy* **50**, 29-35, (2009).

168 Bao, L. L., Mahurin, S. M., Haire, R. G. & Dai, S. Silver-doped sol-gel film as a surface-enhanced Raman scattering substrate for detection of uranyl and neptunyl ions. *Analytical Chemistry* **75**, 6614-6620, (2003).

169 Kneipp, J., Kneipp, H., McLaughlin, M., Brown, D. & Kneipp, K. In vivo molecular probing of cellular compartments with gold nanoparticles and nanoaggregates. *Nano Letters* **6**, 2225-2231, (2006).

170 Kneipp, J., Kneipp, H., Wittig, B. & Kneipp, K. Following the Dynamics of pH in Endosomes of Live Cells with SERS Nanosensors. *Journal of Physical Chemistry C* **114**, 7421-7426, (2010).

171 Raman, C. V. & Krishnan, K. S. A new type of secondary radiation. *Nature* **121**, 501-502 (1928).

172 McCreery & L., R. *Raman Spectroscopy for Chemical Analysis*. (Wiley-Interscience, 2000).

173 Singh, R. C. V. Raman and the Discovery of the Raman Effect. *Physics in Perspective (PIP)* **4**, 399-420 (2002).

174 Moskovits, M. Surface-enhanced spectroscopy. *Reviews of Modern Physics* **57**, 783-826, (1985).

175 Fleischmann, M., Hendra, P. J. & McQuillan, A. J. Raman-spectra of pyridine adsorbed at a silver electrode. *Chem. Phys. Lett.* **26,** 163-166 (1974).

176 Brolo, A. G., Arctander, E., Gordon, R., Leathem, B. & Kavanagh, K. L. Nanohole-enhanced Raman scattering. *Nano Letters* **4**, 2015-2018, (2004).

177 Shanmukh, S. *et al.* Rapid and sensitive detection of respiratory virus molecular signatures using a silver nanorod array SERS substrate. *Nano Letters* **6**, 2630-2636, (2006).

178 Banholzer, M., Qin, L., Millstone, J., Osberg, K. & Mirkin, C. On-wire lithography: synthesis, encoding and biological applications. *Nature Protocols*, 838-848, (2009).

179 Im, H., Bantz, K., Lindquist, N., Haynes, C. & Oh, S. Vertically Oriented Sub-10-nm Plasmonic Nanogap Arrays. *Nano Letters*, 2231-2236, (2010).

180 Anema, J. R., Brolo, A. G., Marthandam, P. & Gordon, R. Enhanced Raman Scattering from Nanoholes in a Copper Film. *Journal of Physical Chemistry C* **112**, 17051-17055, (2008).

181 Yu, Q. M., Guan, P., Qin, D., Golden, G. & Wallace, P. M. Inverted size-dependence of surface-enhanced Raman scattering on gold nanohole and nanodisk arrays. *Nano Letters* **8**, 1923-1928, (2008).

182 Reilly, T. H., Chang, S. H., Corbman, J. D., Schatz, G. C. & Rowlen, K. L. Quantitative evaluation of plasmon enhanced Raman scattering from nanoaperture arrays. *Journal of Physical Chemistry C* **111**, 1689-1694, (2007).

183 Jackson, J. B. & Halas, N. J. Silver nanoshells: Variations in morphologies and optical properties. *Journal of Physical Chemistry B* **105**, 2743-2746, (2001).

184 Whelan, C. M., Smyth, M. R. & Barnes, C. J. HREELS, XPS, and electrochemical study of benzenethiol adsorption on Au(111). *Langmuir* **15**, 116-126, (1999).

185 Wan, L. J., Terashima, M., Noda, H. & Osawa, M. Molecular orientation and ordered structure of benzenethiol adsorbed on gold(111). *Journal of Physical Chemistry B* **104**, 3563-3569, (2000).

186 Dick, L. A., McFarland, A. D., Haynes, C. L. & Van Duyne, R. P. Metal film over nanosphere (MFON) electrodes for surface-enhanced Raman spectroscopy (SERS): Improvements in surface nanostructure stability and suppression of irreversible loss. *Journal of Physical Chemistry B* **106**, 853-860, (2002).

187 Jackson, J. B. & Halas, N. J. Surface-enhanced Raman scattering on tunable plasmonic nanoparticle substrates. *Proceedings of the National Academy of Sciences of the United States of America* **101**, 17930-17935, (2004).

188 Liu, X. F., Sun, C. H., Linn, N. C., Jiang, B. & Jiang, P. Wafer-Scale Surface-Enhanced Raman Scattering Substrates with Highly Reproducible Enhancement. *Journal of Physical Chemistry C* **113**, 14804-14811, (2009).

189 Tao, A. *et al.* Langmuir-Blodgett silver nanowire monolayers for molecular sensing using surface-enhanced Raman spectroscopy. *Nano Letters* **3**, 1229-1233, (2003).

190 Yao, J. L. *et al.* Surface enhanced Raman scattering from transition metal nano-wire array and the theoretical consideration. *Surface Science* **514**, 108-116 (2002).

191 Guieu, V., Talaga, D., Servant, L., Sojic, N. & Lagugne-Labarthet, F. Multitip-Localized Enhanced Raman Scattering from a Nanostructured Optical Fiber Array. *Journal of Physical Chemistry C* **113**, 874-881, (2009).

192 Stockle, R. M., Suh, Y. D., Deckert, V. & Zenobi, R. Nanoscale chemical analysis by tip-enhanced Raman spectroscopy. *Chemical Physics Letters* **318**, 131-136 (2000).

193 Gunnarsson, L. *et al.* Interparticle coupling effects in nanofabricated substrates for surface-enhanced Raman scattering. *Applied Physics Letters* **78**, 802-804 (2001).

194 Ward, D. R. *et al.* Electromigrated nanoscale gaps for surface-enhanced Raman spectroscopy. *Nano Letters* **7**, 1396-1400, (2007).

195 Gopinath, A. *et al.* Plasmonic Nanogalaxies: Multiscale Aperiodic Arrays for Surface-Enhanced Raman Sensing. *Nano Letters* **9**, 3922-3929, (2009).

196 Braeckmans, K., De Smedt, S. C., Leblans, M., Pauwels, R. & Demeester, J. Encoding microcarriers: Present and future technologies. *Nature Reviews Drug Discovery* **1**, 447-456, (2002).

197 Lee, H., Kim, J., Kim, H., Kim, J. & Kwon, S. Colour-barcoded magnetic microparticles for multiplexed bioassays. *Nature Materials* **9**, 745-749, (2010).

198 Dittmer, W. U. *et al.* Sensitive and rapid immunoassay for parathyroid hormone using magnetic particle labels and magnetic actuation. *Journal of Immunological Methods* **338**, 40-46, (2008).

199 Gaster, R. S., Hall, D. A. & Wang, S. X. Autoassembly Protein Arrays for Analyzing Antibody Cross-Reactivity. *Nano Letters* **11**, 2579-2583, (2011).

200 Li, Y. *et al.* Biomarkers identification and detection based on GMR sensor and sub 13 nm magnetic nanoparticles. *Conference proceedings: Annual International Conference of the IEEE Engineering in Medicine and Biology Society. IEEE Engineering in Medicine and Biology Society. Conference* **2009**, 5432-5435 (2009).

201 Pohl, H. A. Some effects of non-uniform fields on dielectrics. *Journal of Applied Physics*, **29**, 1182-1188, (1958).

202 Jones, T. B. Electromechanics of Particles. (Cambridge University Press, NY, 1995).

203 Gierhart, B. C., Howitt, D. G., Chen, S. J., Smith, R. L. & Collins, S. D. Frequency dependence of gold nanoparticle superassembly by dielectrophoresis. *Langmuir* **23**, (2007).

204 Jin, R. Nanoparticle Clusters Light Up in SERS. *Angewandte Chemie-International Edition* **49**, 2826-2829, (2010).

205 Lim, D.-K., Jeon, K.-S., Kim, H. M., Nam, J.-M. & Suh, Y. D. Nanogap-engineerable Raman-active nanodumbbells for single-molecule detection. *Nature Materials* **9**, 60-67, (2010).

206 Kretschmer, R. & Fritzsche, W. Pearl chain formation of nanoparticles in microelectrode gaps by dielectrophoresis. *Langmuir* **20**, 11797-11801, (2004).

207 Hermanson, K. D., Lumsdon, S. O., Williams, J. P., Kaler, E. W. & Velev, O. D. Dielectrophoretic assembly of electrically functional microwires from nanoparticle suspensions. *Science* **294**, 1082-1086, (2001).

208 Jain, P. K., Lee, K. S., El-Sayed, I. H. & El-Sayed, M. A. Calculated absorption and scattering properties of gold nanoparticles of different size, shape, and composition: Applications in biological imaging and biomedicine. *Journal of Physical Chemistry B* **110**, 7238-7248, (2006).

209 Kundu, J. *et al.* Adenine− and Adenosine Monophosphate (AMP)−Gold Binding Interactions Studied by Surface-Enhanced Raman and Infrared Spectroscopies. *The Journal of Physical Chemistry C* **113**, 14390-14397, (2009).

210 Barhoumi, A. & Halas, N. J. Detecting Chemically Modified DNA Bases Using Surface-Enhanced Raman Spectroscopy. *The Journal of Physical Chemistry Letters* **2**, 3118-3123, (2011).

211 Pagliai, M., Caporali, S., Muniz-Miranda, M., Pratesi, G. & Schettino, V. SERS, XPS, and DFT Study of Adenine Adsorption on Silver and Gold Surfaces. *Journal of Physical Chemistry Letters* **3**, 242-245, (2012).

212 Barhoumi, A. & Halas, N. J. Label-Free Detection of DNA Hybridization Using Surface Enhanced Raman Spectroscopy. *Journal of the American Chemical Society* **132**, 12792-12793, (2010).

213 Kneipp, K. *et al.* Detection and identification of a single DNA base molecule using surface-enhanced Raman scattering (SERS). *Physical Review E* **57**, R6281-R6284 (1998).

214 Cho, H., Lee, B., Liu, G. L., Agarwal, A. & Lee, L. P. Label-free and highly sensitive biomolecular detection using SERS and electrokinetic preconcentration. *Lab on a Chip* **9**, 3360-3363 (2009).

215 Derkacs, D., Lim, S. H., Matheu, P., Mar, W. & Yu, E. T. Improved performance of amorphous silicon solar cells via scattering from surface plasmon polaritons in nearby metallic nanoparticles. *Applied Physics Letters* **89**, (2006).

216 Lindquist, N. C., Luhman, W. A., Oh, S.-H. & Holmes, R. J. Plasmonic nanocavity arrays for enhanced efficiency in organic photovoltaic cells. *Applied Physics Letters* **93**, (2008).

217 Reilly, T. H., III, van de Lagemaat, J., Tenent, R. C., Morfa, A. J. & Rowlen, K. L. Surface-plasmon enhanced transparent electrodes in organic photovoltaics. *Applied Physics Letters* **92**,(2008).

218 Ferry, V. E. *et al.* Light trapping in ultrathin plasmonic solar cells. *Optics Express* **18**, A237-A245 (2010).

219 Pillai, S., Catchpole, K. R., Trupke, T. & Green, M. A. Surface plasmon enhanced silicon solar cells. *Journal of Applied Physics* **101**, (2007).

220 Catchpole, K. R. & Polman, A. Plasmonic solar cells. *Optics Express* **16**, 21793-21800 (2008).

221 Peumans, P., Yakimov, A. & Forrest, S. R. Small molecular weight organic thin-film photodetectors and solar cells. *Journal of Applied Physics* **93**, 3693-3723, (2003).

222 Hoppe, H. & Sariciftci, N. S. Organic solar cells: An overview. *Journal of Materials Research* **19**, 1924-1945, (2004).

223 Rand, B. P., Peumans, P. & Forrest, S. R. Long-range absorption enhancement in organic tandem thin-film solar cells containing silver nanoclusters. *Journal of Applied Physics* **96**, 7519-7526, (2004).

224 Rodrigo, S. G. *et al.* Extraordinary optical transmission through hole arrays in optically thin metal films. *Optics Letters* **34**, 4-6 (2009).

225 S. H. Lee *et al.* Linewidth-Optimized Extraordinary Optical Transmission in Water via Template-Stripped Metallic Nanohole Arrays with Tunable Hole Sizes. *Advanced Functional Materials, Accepted* (2012).

226 S. H. Lee *et al.* Real-time Full-spectral Imaging and Affinity Measurements from 50 Microfluidic Channels using Nanohole Surface Plasmon Resonance., Lab on a Chip *Accepted* (2012).

Appendix A

Derivation of the Dispersion Relations

This section describes the detailed derivation of the real and imaginary part of dispersion relations. The dispersion equation can be expressed as:

$$\beta = \frac{\omega}{\boldsymbol{c}}\sqrt{\frac{\varepsilon_m \varepsilon_d}{\varepsilon_m + \varepsilon_d}} = \frac{\omega}{\boldsymbol{c}}\sqrt{\frac{\left(\varepsilon_m' + \boldsymbol{i}\varepsilon_m''\right)\varepsilon_d}{\left(\varepsilon_m' + \boldsymbol{i}\varepsilon_m''\right) + \varepsilon_d}} = \frac{\omega}{\boldsymbol{c}}\sqrt{\frac{\varepsilon_d\left(\varepsilon_m' + \boldsymbol{i}\varepsilon_m''\right)\left(\varepsilon_m' + \varepsilon_d - \boldsymbol{i}\varepsilon_m''\right)}{\left(\varepsilon_m' + \varepsilon_d\right)^2 + \left(\varepsilon_m''\right)^2}}$$

$$\cong \frac{\omega}{\boldsymbol{c}}\frac{\sqrt{\varepsilon_d\left\{\left(\varepsilon_m' + \boldsymbol{i}\varepsilon_m''\right)\varepsilon_d + \varepsilon_m'^2\right\}}}{\varepsilon_m' + \varepsilon_d} = \sqrt{\frac{\varepsilon_m'\varepsilon_d}{\varepsilon_m' + \varepsilon_d}\left(\frac{\omega}{\boldsymbol{c}}\right)^2 + \boldsymbol{i}\frac{\varepsilon_m''\varepsilon_d^2}{\left(\varepsilon_m' + \varepsilon_d\right)^2}\left(\frac{\omega}{\boldsymbol{c}}\right)^2}$$

where, $\varepsilon_m = \varepsilon_m' + i\varepsilon_m''$

To separate real and imaginary terms of dielectric function, assume $\alpha + \boldsymbol{i}\chi = \sqrt{\boldsymbol{a} + \boldsymbol{ib}}$, then

$$\alpha + i\chi = \sqrt{a + ib}$$

$$\left(\alpha + i\chi\right)^2 = \left(\alpha^2 - \chi^2\right) + i2\alpha\chi = a + ib$$

$$\alpha^2 - \chi^2 = a$$

$$2\alpha\chi = b \;\rightarrow\; \chi = \frac{b}{2\alpha}$$

$$\alpha^2 - \left(\frac{b}{2\alpha}\right)^2 = a \;\rightarrow\; 4\alpha^4 - 4a\alpha^2 - b^2 = 0$$

$$\alpha^2 = \frac{2a \pm \sqrt{4a^2 + 4b^2}}{4} = \frac{a \pm \sqrt{a^2 + b^2}}{2}$$

$$\alpha = \sqrt{\frac{a + \sqrt{a^2 + b^2}}{2}}$$

$$\chi = \frac{b}{2\alpha} = \frac{b}{2}\sqrt{\frac{2}{a + \sqrt{a^2 + b^2}}}$$

From the dispersion relations,

$$\boldsymbol{a} = \frac{\varepsilon_m' \varepsilon_d}{\varepsilon_m' + \varepsilon_d}\left(\frac{\omega}{\boldsymbol{c}}\right)^2,\ \boldsymbol{b} = \frac{\varepsilon_m'' \varepsilon_d^2}{\left(\varepsilon_m' + \varepsilon_d\right)^2}\left(\frac{\omega}{\boldsymbol{c}}\right)^2$$

$$\sqrt{\boldsymbol{a}^2 + \boldsymbol{b}^2} = \left(\frac{\omega}{\boldsymbol{c}}\right)^2 \frac{1}{\left(\varepsilon_m + \varepsilon_d\right)^2}\sqrt{\varepsilon_m'^2 \varepsilon_d^2 \left(\varepsilon_m' + \varepsilon_d\right)^2 + \varepsilon_m''^2 \varepsilon_d^4} \cong \left(\frac{\omega}{\boldsymbol{c}}\right)^2 \frac{\varepsilon_m' \varepsilon_d \left(\varepsilon_m' + \varepsilon_d\right)}{\left(\varepsilon_m + \varepsilon_d\right)^2} = \left(\frac{\omega}{\boldsymbol{c}}\right)^2 \frac{\varepsilon_m' \varepsilon_d}{\varepsilon_m + \varepsilon_d}$$

Therefore, the real and imaginary value can be expressed as:

$$\mathrm{Re}[\beta] = \alpha = \sqrt{\frac{\left(\frac{\omega}{\boldsymbol{c}}\right)^2 \frac{\varepsilon_m' \varepsilon_d}{\varepsilon_m' + \varepsilon_d} + \left(\frac{\omega}{\boldsymbol{c}}\right)^2 \frac{\varepsilon_m' \varepsilon_d}{\varepsilon_m' + \varepsilon_d}}{2}} = \left(\frac{\omega}{\boldsymbol{c}}\right)\sqrt{\frac{\varepsilon_m' \varepsilon_d}{\varepsilon_m' + \varepsilon_d}}$$

$$\mathrm{Im}[\beta] = \frac{\boldsymbol{b}}{2\alpha} = \frac{\varepsilon_m'' \varepsilon_d^2}{\left(\varepsilon_m' + \varepsilon_d\right)^2}\left(\frac{\omega}{\boldsymbol{c}}\right)^2 \frac{1}{2}\left(\frac{\boldsymbol{c}}{\omega}\right)\sqrt{\frac{\varepsilon_m' + \varepsilon_d}{\varepsilon_m' \varepsilon_d}} = \frac{\omega}{2\boldsymbol{c}}\left(\frac{\varepsilon_d}{\varepsilon_m' + \varepsilon_d}\right)^{\frac{3}{2}} \frac{\varepsilon_m''}{\sqrt{\varepsilon_m'}} \quad \text{or} \quad \frac{\omega}{\boldsymbol{c}}\left(\frac{\varepsilon_m' \varepsilon_d}{\varepsilon_m' + \varepsilon_d}\right)^{\frac{3}{2}} \frac{\varepsilon_m''}{2\varepsilon_m'^2}$$

Appendix B

Fabrication Methods and Recipes

This appendix outlines detailed fabrication steps, procedures, and recipes.

B.1.1 Fabrication of nanohole arrays using template stripping

1) Prepare Si wafers with 100-nm-thick (or 200-nm thick) thermal oxide using wet oxidation at 1100 ^{o}C for 11 min.

2) Spin-coat the surface with a thermal nanoimprint resist (NXR-1025 from Nanonex Corp., NJ) at 3500 rpm for 1 min and bake the resist at 150 _C for 1 min.

3) Prepare a Si imprint stamp with a 2-dimensional array of circular posts with 210 nm in diameter, 350 nm in depth, and 500 nm in periodicity and coat the Si surface with (heptadecauoro-1,1,2,2-tetrahydrodecyl)trichlorosilane (obtained from Gelest Inc., PA) using a vacuum dessicator for 1 hr.

4) Imprint the Si stamp onto the resist with a pressure of 300 psi for 2 min at 130 ^{o}C

5) Etch the thermal oxide layer with the imprint resist as a mask for 4 min with 25 sccm of CF4 and 50 sccm of Ar gases at 150 W (PJSOXIDE recipe in STS etcher)

7) Remove the imprint resist by dipping in acetone for 30 min and subsequent oxygen plasma cleaning for 5 min with 100 sccm of O_2 at 100 W (O2CLEAN recipe in STS etcher)

8) Etch Si with the patterned oxide layer as a mask for 2 min using Si deep trench etcher (CNF-14mT recipe in DRIE)

9) Clean the patterned Si template with oxygen plasma for 15~30 min (O2CLEAN recipe in STS etcher)

10) Remove the oxide layer using a BOE solution until the surface turns into hydrophobic.

11) Clean the template using a piranha solution for 5 min.

12) Rinse the Si template with DI water at least 3 times. Dry the template first using a nitrogen gas and then a hotplate above 100 ^{o}C until the surface is perfectly dried.

13) Deposit metals using the Temescal e-beam evaporator without any adhesion layer. It is crucial to reduce the metal deposition on the sidewalls, especially in order to obtain optically thick (> 100 nm) films, requiring the alignment of the metal evaporation source normal to the sample surface. To obtain smooth metal surface after template stripping, the deposition rate should be very slow (< 0.1 A/sec) for first 10-20 nm of metal film.

14) Coat the metal with UV-curable optical epoxy (NOA 61, Norland products Inc., NJ) and cover it with a glass slide. It is crucial to use minimal amount of optical epoxy to obtain nanoholes with clean edges.

15) Cure the epoxy under UV light for 30 min and leave on a hotplate at 50 ^{o}C for several hours.

16) Peel off the metal of the Si template.

17) If necessary, the template-stripped metal can be covered by a thin silica layer using ALD at 100 ^{o}C. The deposition rate is around 16 A/cycle. (Use slow-test1 recipe in ALD)

18) Clean the Si template by removing remaining metals with wet etchants.

B.1.2 Fabrication of PDMS microfluidic flow cells

1) Remove a native oxide layer on a Si wafer by dipping the wafer in a BOE solution for a few seconds.
2) Make desired patterns using a SU-8 resist on the wafer. The type and spin-coating parameters should be adjusted based on the desired thickness of SU-8 mold. For instance, a SU-8 50 resist is used to make patterns with the height of around 50 μm ~ 100 μm.

For 50 μm-thick patterns,

(i) spin coat a SU-8 50 resist at 1300 rpm for 30 sec.

(ii) bake the resist at 65 ^{o}C for 10 min and then 95 ^{o}C for 40 min.

(iii) expose the resist under UV light through a photomask for 50 sec.

(iv) bake the resist at 65 ^{o}C for 1 min and then 95 ^{o}C for 5 min.

(v) develop the resist for 10 min using a SU-8 developer.

For 100 μm -thick patterns,

(i) spin coat a SU-8 50 resist at 2000 rpm for 30 sec.

(ii) bake the resist at 65 ^{o}C for 6 min and then 95 ^{o}C for 20 min.

(iii) expose the resist under UV light through a photomask for 30 sec.

(iv) bake the resist at 65 ^{o}C for 1 min and then 95 ^{o}C for 5 min.

(v) develop the resist for 6 min using a SU-8 developer.

3) Remove residual resist for 30 sec with 100 sccm of O_2 at 100 W (O2CLEAN recipe in STS etcher)

4) Coat the SU-8 mold wafer with (heptadecauoro-1,1,2,2-tetrahydrodecyl) trichlorosilane (obtained from Gelest Inc., PA) using a vacuum dessicator for 1 hr to prevent sticking of PDMS on the Si surface.

5) Mix 30 g of PDMS with 3 g of curing agent and remove bubbles using a vacuum dessicator.

6) Pour the degassed PDMS mixture onto the SU-8 mold placed in an alumina foil basket.

7) Cure the PDMS at 60 ^{o}C for overnight. Curing at higher temperature will reduce the curing time.

8) Cut PDMS using a razor blade, punch inlets and outlets, and clean the surface with acetone, methanol, IPA, and water.

Appendix C

Common Acronyms

Table C.1: A listing of the common acronyms used throughout the dissertation.

Acronym	Meaning
ALD	Atomic Layer Deposition
AgFon	Ag Film Over Nanosphere
AR	Aspect Ratio
BCP	2,9-dimethyl-4,7-diphenyl-1,10-phenanthroline
BZT	Benzenethiol
Biotin-PE	Biotinylated-Phosphatidylethanolamine
CTX-b	Cholera Toxin b Subunits
CuPc	Copper Phthalocyanine
DEP	Dielectrophoresis
DUV	Deep Ultraviolet
DPPE	1,2-Bis(diphenylphosphino)ethane
EBL	Electron Beam Lithography
Egg-PC	Egg Phosphatidylcholine
EFs	Enhancement Factors
EM	Electromagnetic
EOT	Extraordinary Optical Transmission
FDTD	Finite-Difference Time-Domain
FF	Fill Factor
FIB	Focused Ion Beam
FRAP	Fluorescence Recovery After Photobleaching
FWHM	Full Width at Half Maximum
GM1	Ganglioside Monosialic Acid
GMR	Giant Magnetoresistance
HOMO	Highest Occupied Molecular Orbit
ITO	Indium-Tin-Oxide
IPA	Isopropyl Alcohol
	Continued on next page

Table C.1: Continued from previous page

Acronym	Meaning
LOD	Limit of Detection
LOQ	Limit of Quantification
LSRP	Localized Surface Plasmon Resonance
LUMO	Lowest Unoccupied Molecular Orbit
MIM	Metal-Insulator-Metal
NPs	Nanoparticles
NSL	Nanosphere Lithography
NBD-PE	Nitrobenzoxadiazole-Conjugated Phosphatidylethanolamine
OPVs	Organic Photovoltaic Cells
PEEL	Phase-shift lithograhpy, Etching, Electron-beam deposition, and Lift-off
PDMS	Polydimethylsiloxane
RIE	Reactive Ion Etching
RIU	Refractive Index Units
Rho-PE	Rhodamine-labeled Phosphatidylethanolamine
RMS	Root-Mean-Square
SEM	Scanning Electron Micrograph
SAPE	Streptavidin-R-Phycoerythrin
SLBs	Supported Lipid Bilayers
SERS	Surface Enhanced Raman Spectroscopy
SPP	Surface Plasmon Polaritons
SPR	Surface Plasmon Resonance
SPs	Surface Plasmons